JACOBS
UNIVERSITY

# Wave packet simulations of nonlinear spectroscopy and excitation transfer in molecular systems

by

**Jörg Liebers**

A thesis submitted in partial fulfillment
of the requirments for a degree of
**Doctor of Philosopy in Physics**

**Thesis Committee:**

Professor Dr. Ulrich Kleinekathöfer    (Jacobs University Bremen, Germany)

Professor Dr. Arnulf Materny    (Jacobs University Bremen, Germany)

Dr. Thomas L. C. Jansen    (Zernike Institute for Advanced Materials,
 The Netherlands)

Date of Defense: November 4, 2011

School of Engineering and Science - Computational Physics and Biophysics Group

# Abstract

The theoretical framework of wave packet dynamics can be applied to describe many aspects in molecular physics and the interaction of matter and light. In this thesis wave packet dynamics occurring in various molecular systems have been investigated. This includes the simulations of nuclear wave packet dynamics in different electronic states of diatomic molecules initiated by femtosecond laser pulses. With these simulations the theoretical analyses of femtosecond time-resolved four-wave mixing experiments was possible. Furthermore a theoretical description of non-resonant multi-photon excitations has been given, which allows to study the wave packet dynamics initiated by such processes in the time domain. This is essential for the application of non-resonant femtosecond laser pulse excitations to control and investigate molecular dynamics. A further focus of this thesis is the investigation of excitation energy transfer in biological pigment complexes. A hybrid quantum classical approach is applied to describe excitonic wave packet dynamics in such complex molecular aggregates. This approach was verified within an artificial test system an then applied to the light harvesting system II of a purple bacteria. To perform simulations on this system, data from all-atom classical molecular dynamics simulations have been used to construct a model system for this complex. This allowed for the investigation of the excitation energy transfer dynamics which are an important aspect of the light harvesting process in photosynthesis. For these systems it was shown that the wave packet approach in combination with classical molecular dynamics simulations is a powerful tool to describe quantum dynamical processes in large molecular systems.

# Contents

# 1. Introduction

In the last decades there has been a strong trend in science towards the investigation of ever-smaller structures leading to the ubiquitous field of nano science aiming to understand the structure and functionality of nature on a molecular scale [1]. The structure of molecular systems can be exposed with high spatial resolution using tools like atomic force and scanning tunneling microscopes as well as X-ray diffraction. Alongside these experiments, the rapid progress made in the development of ultra short laser pulses opened the possibility to observe elementary dynamical processes in molecular systems in real time. With today's experimental techniques it is for example possible to monitor the fundamental nuclear motions in molecules during the absorption of light or within the progress of chemical reactions [2]. Also the atomic structures and quantum dynamical processes occurring in complex biological molecules optimized for functionality over millions of years of evolution can be resolved in detail [3, 4].

Although these experiments yield a multitude of detailed information about the nature of nanoscopic systems they are sometimes not sufficient to understand the complete course of processes in those systems leading to specific behaviors. Owing the development of modern computer systems [5, 6] with high processing capacity for complex calculation-intensive tasks over the last years it became feasible to model and simulate these kind of systems on an molecular level [7]. These simulations provide a new approach for the investigation of the fundamental processes in molecular systems. Still these simulations are limited and complete quantum mechanical calculations can only be performed for very small systems containing only a few atoms. But a complete description is often not necessary since a reduced model system can be sufficient to reproduce experimental results. The construction of such model systems is already the first step in understanding a system because the key properties of the system need to be determined.

The work presented here addresses the simulation of two different kinds of ultra-fast processes in molecular systems. In the first part the nuclear motions in small molecular systems induced by sequences of ultrashort femtosecond laser pulses are investigated and compared to experimental results. The second part applies to the simulation of energy transfer processes in large molecular systems. In both cases the wave packet formalism [8] is used to simulate the quantum dynamics which governs their time-dependent characteristics.

The experimental observation of nuclear wave packets in molecules was enabled by the availability of ultrashort laser pulses and opened a new field in chemical physics. The field of femtochemistry [2, 9, 10] which enfolds the investigation of elementary molecular processes using ultrashort laser pulses evolved in the late 90's initiated by the experiments performed by A. Zewail and co-workers [2, 9]. Today laser pulses can be generated in a spectral range spanning from ultraviolet to far infra-red. These laser pulses can be used to initiate and monitor the complex dynamics in molecular systems ranging from diatomic molecules [2] to complex biological systems [11, 12]. The basic concept of most of these time-resolved femtosecond spectroscopy experiments are pump probe schemes [13] where one laser pulse is employed to initiate dynamics in the system and a second laser pulse with a femtosecond time delay is used to probe the system. In contrast to other spectroscopic methods based on absorption, emission or scattering of light these time resolved experiments yield additional information about the chemical dynamics in the molecules. Femtosecond laser pulses are spectrally very broad so that an interaction with these pulses excites multiple states in the molecule coherently. This coherent superposition of eigenstates forms a wave packet whose time evolution can be monitored in the spectroscopic signal in form of quantum beats. Since the wave packet is the solution for the time-dependent Schrödinger equation [14, 15]

$$i\hbar\frac{\partial}{\partial t}|\Psi(t)\rangle = H(t)|\Psi(t)\rangle$$

of the system, these experiments offer the possibility to visualize a quantum system evolving in time. In addition to the simple two pulse pump-probe schemes other non-linear spectroscopic methods have been employed [16]. This work focuses on the simulation of time-resolved four wave mixing (FWM) experiments. The FWM

scheme involves the use of three non-linear electric fields interactions to create a fourth wave which obeys energy conservation and phase matching conditions. The time-dependent response of the molecule to these pulse sequence is given by the induced third-order non-linear polarization [16–18]. The FWM spectroscopy offers many degrees of freedom allowing for a separate analysis of different electronic states by varying timing, polarization and wavelength of the pulses. Another advantage is the generation of a strong background free signal due to the phase matching condition. The FWM scheme can also be combined with an initial pump pulse to access high-lying electronic states [19].

Already small molecular systems like diatomic molecules show very complex dynamics [20, 21]. For these systems the nuclear Schrödinger equation including the interaction with the laser fields can be solved numerically with an precision that allows for an exact comparison to experimental results [22]. The simulations presented in this thesis are motivated by experiments performed in the group of Prof. A. Materny [23–25]. They used a combination of FWM with an initial pump pulse to investigate the dynamics in high-lying electronic states including ion-pair states in molecular bromine and iodine. The measured signals for bromine showed some interesting features which could be identified using our simulations as contributions from hot ground states. In the past years there have been a lot of publications concerning femtosecond spectroscopy of iodine and bromine, experimentally [26–30] and theoretically [31–33]. But most of this work was objected to ground state dynamics. Here we extend the investigations to higher lying electronic states using the pump FWM scheme. Iodine and bromine are well characterized by frequency-resolved spectroscopy [34–41] so that the excitation energies for the vibronic states in many electronic states are well known. Using this data it is possible to construct very accurate potential energy surfaces for the electronic states of these molecules which are of essential importance for accurate simulations. This fact makes these molecules excellent model systems for testing new spectroscopic methods. The exact knowledge of the excitation processes in such simple systems also opens the way to prepare and probe specific states in the molecule which is an key element for the development of quantum computers [42] or the control of chemical reactions [43].

A common approximation in building model system for theoretical spectroscopy is to truncate the the used state space to only those bound electronic states which are

directly involved in the interaction with the laser pulses [8]. But there are of course an infinite number of unbound electronic states which may also contribute to the spectra [44]. These states become important for multi-photon processes where the energy of two or more photons induces transitions which do not involve intermediate states to support them [45–47]. This can be a two-photon excitation where the photon energy is half of the fundamental optical transition or non-resonant Raman processes, where the energy difference of two photons matches an transition energy in the molecule. Theoretically these non-resonant processes can be treated conveniently in the frequency domain [16] but that will not allow for the study of time-resolved experiments. For that reason we investigated methods to simulate these processes in time domain. The used theory is based on a projection operator formalism in the framework of a time-local approach and compared to time-non-local approaches [48, 49]. This formalism also considers a reduced states space of levels involved in the transitions but additionally contains an effective coupling to the manifold of off-resonant states. In this work reasonable approximations for the formulation of the effective coupling are discussed and verified for two and three photon transitions in a two level model system.

An other application of wave packet simulations which is utilized in the scope of this thesis is the simulation of excitation energy transfer (EET) in complex biological systems [50–53]. The usual size of these molecular complexes ranges in an order of magnitude of several hundred thousand atoms [54]. Therefore a full quantum simulation of these systems are at present computationally prohibitive. To simulate these systems multi scale modeling approaches are needed [7]. The first choice to describe energy changes in such large systems are usually classical molecular dynamics (MD) simulations [55–57] because they can be performed with relatively low computational costs. In the MD simulations all the interactions between the atoms in the system are encoded in force fields which are then employed to calculated the structural changes using Newton's classical equations [58]. The problem with these simulations is that they completely ignore quantum effects and do not allow for the calculation of optical properties. To circumvent this deficiency hybrid quantum/classical methods [7] are used because in most cases a full quantum description is only needed for some degrees of freedom of the system. One way is for example a the time-dependent combination of molecular dynamics (MD) simulations and quantum chemistry (QC) methods to calculate a time-dependent

Hamiltonian of the quantum subsystem which can subsequently be used for an ensemble-averaged wave packet simulation [59, 60]. An other way is to utilize density matrix calculations based on spectral densities which can also be calculated from the MD/QC results [48, 61]. Here we focus on wave packet calculations which employ the time dependent Hamiltonian from the MD simulations directly and therefore make use of their complete information with out truncating them into spectral densities. One disadvantage of the wave packet simulations is the fact that it includes an implicit high-temperature assumption and therefore does not equilibrate into the correct thermal state. Methods which can resolve this issue will be discussed and tested in the following on a two level system coupled to a bath.

This thesis is organized as follows:

The subsequent chapter contains an introduction to the basic aspects of the wave packet formalism for the calculation of spectroscopic signals. Therefore a short introduction to the general aspects of femtosecond time-resolved four wave mixing spectroscopy is given followed by an elucidation of the details for the numerical solution of the time-dependent Schrödinger equation for nuclear motions in diatomic molecules and the construction of potential energy surfaces from excitation energies. The last part of this chapter explains how non-linear spectroscopic signals can be calculated from the solutions of the time-dependent Schrödinger equation. Perturbative and non-perturbative methods are discussed. Furthermore the methodology for the incorporation of an initial pump pulse in the FWM scheme is detailed. In addition a short overview of the setup used in the FWM experiments which were used for comparison to the simulations is given here.

The application of these methods to the interrogation of vibrational dynamics occurring in high-lying electronic states is detailed in chapter 3 following our publication [62]. As a first test case for this methods simulations for pump degenerate four wave mixing (pump-DFWM) experiments on molecular iodine in gas phase are simulated and compared to experimental results measured in the group of Prof. A. Materny. Pump-DFWM is a FWM scheme, in which all pulses have the same wavelength. First an introduction to the spectroscopic properties of iodine is given followed by a description of a model system for the iodine molecule. The spectroscopic pathways which contribute to the FWM signal are detailed in a further paragraph. The calculated results are then compared to the experimental outcome

for a set of different wave lengths and time orderings of the FWM pulses.

In chapter 4 simulations for pump-DFWM experiments on molecular bromine in gas phase are presented. In the experiments the dynamics in the excited $B$ state were monitored via transitions to ion pair states and showed different vibrational energy spacings for different DFWM wavelengths. The simulations were able to show that these different spacings arise from contributions of hot vibrational states in the electronic ground state. The experimental signal was dispersed and then recorded using a CCD camera which allowed for a frequency and time-resolved detection. The theoretical results were also calculated frequency and time resolved resulting in 2D spectral maps which were compared to the experimental results. The explanations in this chapter include details of the used model system for bromine, a comparison of theory and experiment followed by a discussion of the latter [63].

The vibrational dynamics in ion-pair states of molecular bromine are investigated in chapter 5. Here a similar methodology as in chapter 3 is used and applied to bromine but were extended to also include frequency and time resolved signals. Here the simulations are used to identify the contributions of different electronic states to signal. The theoretical modeling for this case is explained in detail followed by a discussion of theoretical and experimental results as published in Ref [64].

Chapter 6 introduces a time-local formalism for the description of non-resonant multi photon transitions between the electronic states of a molecular system published in Ref. [65]. It is based on a projection operator formalism leading to time-dependent Schrödinger equations which include effective couplings to manifold of off-resonant electronic states. To enhance the computational efficiency, the slowly varying amplitude approximation is invoked and tested. The validity of this approximation is verified numerically for two and three-photon processes.

In chapter 7 the application of wave packet simulation for the investigation of excitation energy transfers in quantum systems coupled to an environment is discussed in the context of hybrid quantum/classical methods. Therefore an artificial two-level Hamiltonian is created using statistical algorithms. This Hamiltonian mimics a two-level system which is coupled to a bath with a specific spectral density. Using this Hamiltonian, ensemble averaged wave packet simulations are performed, discussed and compared to dissipative density matrix calculations. As stated before,

14

the wave packet calculations comprise an implicit high-temperature assumption so that the correct thermal equilibrium distribution is not reached in the long time limit. There exist some attempts to overcome this drawback. Here we investigate a method proposed by A. Bastida and co-workers [66–68] which modifies the system bath couplings an a way that the dynamics obey the correct temperature behavior. This methodology will be explained in detail and applied to the two-level model system. The results are compared to dissipative density matrix calculations which exhibit the correct temperature behavior. Finally these calculations are applied to Hamiltonians calculated from resent MD/QC calculations of the light harvesting complex II found in the photosynthetic apparatus of purple bacteria [59, 69, 70].

The last chapter summarizes the results of the work presented in this thesis.

# 2. Wave-packet simulation of non-linear femtosecond spectroscopy

In this chapter the basics of the theoretical description of nonlinear time-resolved spectroscopy are detailed. For a deeper insight we refer to several textbooks [8, 16–18] on this subject. Here are those details specified which are essential for the theoretical description of four wave mixing spectroscopy of diatomic molecules, which will be matter of the next chapters. An direct extraction of the excitation processes from the experimental results is in some cases not possible and the interpretation of experimental results becomes complicated. Thus, simulations are an important instrument to investigate the molecular dynamics. To explain the theoretical model system for these simulations an overview of the experimental methods is given first.

## 2.1. Femtosecond time-resolved four-wave mixing spectroscopy

Four-wave mixing (FWM) spectroscopy involves the interaction of three laser beams with a medium generating a fourth beam, the FWM signal. The advantages of FWM spectroscopy are a high signal to noise ratio and a coherent laser like signal beam, allowing for a sensitive detection of molecular dynamics. Also the various degrees of freedom offered by this method allow to explore a multitude of aspects of molecular dynamics by changing the time ordering, wave lengths, polarizations durations and shapes of the incident pulses. FWM can be realized in different
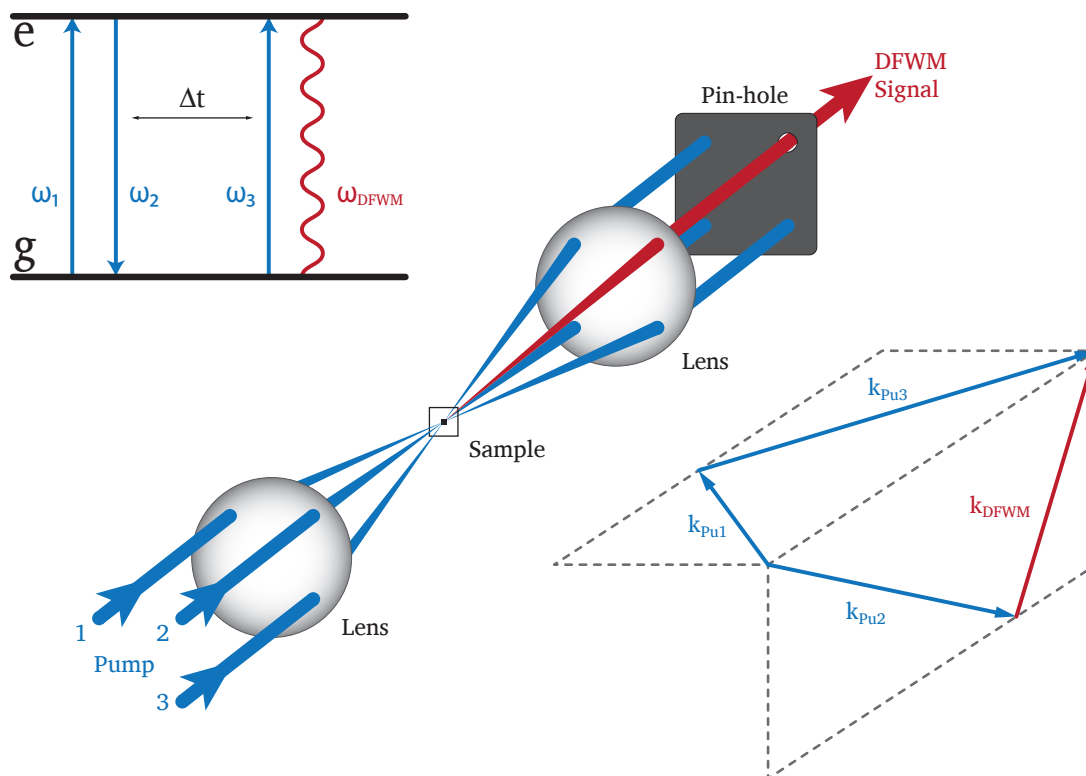
**Figure 2.1.: left:** Energy diagram showing the molecular transition of the DFWM process in a two level system. **middle:** BOXCARS beam geometry. The three pulses pass trough the corners of a box and are the focused by a lens on the sample. The signal emerges spatial separated from the incident pulses and can be separated with a pinhole due to the phase matching condition. **right:** Wave vector diagram for the DFWM experiment.

schemes, as for example coherent anti-Stokes Raman scattering (CARS), photon echo (PE) and degenerate four-wave mixing (DFWM) [71, 72].

In its time-resolved form FWM is a very powerful tool to prepare, manipulate, and observe molecular dynamics [16]. To achieve this, three laser pulses of different wave lengths (CARS) or equal wavelength (DFWM) are used to excite the medium in a specific time order. The generated fourth beam shows a time variation which depends on the temporal order of the pulse sequence. By analyzing the detected signal, informations about the dynamics in ground and excited state can be obtained. If these experiments are carried out with femtosecond laser pulses the time ordering can be controlled in fractions of femtoseconds which allows to monitor molecular vibrations, which happen on such time scale, directly. Since the spectrum of the pulse is related to the temporal shape by its Fourier transform, femtosecond pulses

are spectrally broad. A 100 fs pulse of wave length 800 nm has, for example a spectrally width of about 10 nm (20 meV). Since this is in most cases more than the energy spacing of vibrational states in molecules several modes are excited coherently. The dynamics of these modes are then reflected in the measured signal. As mentioned above, the FWM refers to a non-linear process of four interacting electromagnetic waves. The response of the medium to this electromagnetic radiation is described by the induced polarization. In the case of the non-linear FWM, the response is characterized by the third-order polarization, which is proportional to the third power of the field strength and given by

$$P^{(3)} = \chi^{(3)} \mathbf{E_1} \mathbf{E_2} \mathbf{E_3} \,, \tag{2.1}$$

where $\chi^{(3)}$ is the third-order non-linear optical susceptibility. The wave vector $\mathbf{k}_S$ of the signal fulfills the phase-matching condition

$$\mathbf{k}_S = \pm \mathbf{k}_1 \pm \mathbf{k}_2 \pm \mathbf{k}_3 \tag{2.2}$$

and also the frequency of the signal is a linear combination of the incident frequencies

$$\omega_S = \pm \omega_1 \pm \omega_2 \pm \omega_3 \,. \tag{2.3}$$

This spatial and energetic separation of the signal from the incident laser beams makes it easy to separate both from each other. The sign of the wave vectors and frequencies depends on the used beam geometry. The experiments which are object of the presented theoretical work are DFWM experiments [73, 74] with a folded BoxCars [75] geometry shown in Fig. 2.1. Therefore the phase matching condition reads

$$\mathbf{k}_S = \mathbf{k}_1 - \mathbf{k}_2 + \mathbf{k}_3 \,. \tag{2.4}$$

Since the wave lengths of the three incident pulses are of identical frequencies, the signal frequency is also the same

$$\omega_S = \omega_1 = \omega_2 = \omega_3 \,. \tag{2.5}$$
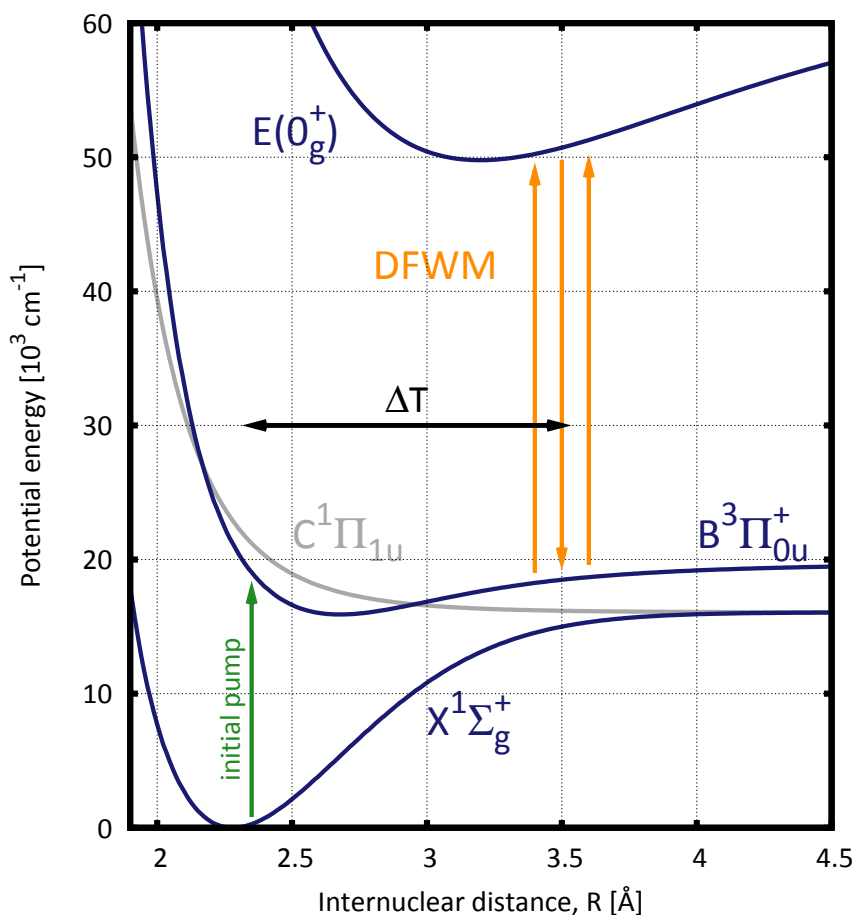
**Figure 2.2.:** Pump DFWM scheme used for the investigation of the dynamics in higher lying electronic. The initial pump pulse creates a wave packet in the first excited state, which is then probed by a DFWM process via higher electronic states. The potential energy surfaces shown here belong to molecular bromine.

An wave vector and energy diagram are depicted in Fig. 2.1 to illustrate the DFWM scheme.

### 2.1.1. Pump-DFWM

In order to access higher lying electronic states, the DFWM process can be combined with an additional pump pulse. These schemes are referred to as pump-DFWM [19]. Fig 2.2 shows the pump-DFWM applied to three electronic states in molecular bromine. In these experiments, a wave packet is excited from the ground state

to the first excited state in a first step called the initial pump. This initial pump pulse, which is in resonance with a transition from ground to first excited state is a spectrally broad femtosecond pulse, which creates a superposition of vibrational states, a wave packet, in the first excited state. After a time delay $\Delta T$, a conventional DFWM process is used to probe the excited state wave packet. In the experiments under investigation, one of the laser pulses was time delayed relatively to the other two time coincident laser pulses over a time range of several picoseconds, the time zero of the DFWM process, $\Delta t = 0$ ps, was defined by the temporal overlap of all three pulses. $\Delta T$ on the other hand was measured as time delay between the initial pump and the two time coincident DFWM pulses. Scanning $\Delta t$ yields a time-dependent signal, from which the dynamics of the first excited state and higher lying electronic states can be obtained. These experiments were performed by A. Scaria and are explained in detail in his PhD thesis [25]. However, for the purpose of completeness a short summary of the experimental setup is given below.

## 2.1.2. Experimental setup

A commercial femtosecond laser system (Clark-MXR Inc., CPA-2010) in combination with two optical parametric amplifiers (OPAs; TOPAS, Light Conversion) was used to provide the femtosecond pulses at different wavelengths required for the experiment. The output of one of the OPAs served as initial pump pulse. In order to obtain the three four wave-mixing (FWM) beams, the output of the second OPA was split into three equal parts. The pulses had a temporal width of 150 fs with an average energy of 1 mJ per pulse. A spatial and at the start of the experiment also a temporal overlap of the beams in the sample was required for the FWM process. The time delay between the pulses was realized with computer-controlled linear translation stages in Michelson interferometer arrangements. The temporal overlap of the beams was determined by using the optical Kerr effect [76] for the ultraviolet beams. The time zero point was defined as the positions of the delay stages were the beams coincided in time. A three-dimensional forward geometry (Folded BoxCARS) [75] arrangement was used, which fulfills the phase matching condition and provides a good spatial separation of the signal. Using a lens, the four beams were then focused into the cuvette containing iodine. After interaction

with the sample, the spatially separated DFWM signal was spatially filtered out by a pinhole. The collimated signal was then focused onto the entrance slit of a single monochromator and after dispersion detected using a Peltier-cooled CCD camera. Since the signal is of the same wavelength as the incoming FWM beams, extreme care was taken to minimize background due to scattering from the walls of the cuvette.

## 2.2. Theory and model

The signals measured in the previously mentioned experiments are primarily governed by the vibrational dynamics of the investigated molecular system. Traces of rotational motion are also present in the measured signals but they have in general a minor influence on the basic features of the experimental outcome in these systems. Since our aim was to achieve a very accurate simulation of the experimental results we chose a model system containing only the key properties but focused on calculating the parameters as accurate as possible. The next sections explain the methodology of building a model system for the simulation of these diatomic molecular systems.

### 2.2.1. Time-dependent Schrödinger equation for nuclear motion

The time evolution of the molecular system is governed by the time-dependent Schrödinger equation

$$i\hbar\frac{\partial}{\partial t}|\Psi(t)\rangle = H_{mol}(t)|\Psi(t)\rangle \tag{2.6}$$

where $|\Psi(t)\rangle$ represents the current state of the molecular quantum system including nuclei and electrons. The molecular Hamiltonian $H_{mol}(t)$ which generates the time evolution of $|\Psi(t)\rangle$ consists of the operators for kinetic energies and Coulomb interactions between nuclei and electrons

$$\begin{aligned}\hat{H}_{mol} &= \hat{T} + \hat{V} \\ &= \hat{T}_{el} + \hat{T}_{nuc} + \hat{V}_{el-el} + \hat{V}_{nuc-nuc} + \hat{V}_{el-nuc} \, .\end{aligned} \tag{2.7}$$

The stationary properties of this molecular system are determined by the solutions of the time-independent Schrödinger equation

$$\hat{H}_{mol}\,|\Psi\rangle = \epsilon\,|\Psi\rangle \ . \tag{2.8}$$

The solutions of this equation provides the energy spectrum $\epsilon_n$ with its corresponding eigenvectors $|\Psi_n\rangle$. The systems wave function can be obtained by projecting the state vector to Cartesian coordinates

$$\Psi(\mathbf{r}, \sigma, \mathbf{R}) = \langle \mathbf{r}, \sigma, \mathbf{R}|\Psi\rangle \ , \tag{2.9}$$

where $\mathbf{r}$ and $\mathbf{R}$ are the sets of position vectors of all electrons and nuclei and $\sigma$ the electrons spin. The probability distribution $|\Psi(\mathbf{r}, \sigma, \mathbf{R})|^2$ of the wave function comprehends the spatial arrangement of electrons and nuclei.

### 2.2.2. Born-Oppenheimer separation

For the solution of Eq. 2.6 it is advantageous to separate the system in an electronic and a nuclear part. This is reasonable due to the fact that the electrons move much faster than the nuclei because they are three orders of magnitude lighter. In general, this leads to an instantaneous response of the electrons to a change in the nuclear configuration, i.e., the electron-nuclei interaction depends adiabatically on the motion of the nuclei. Thus, the electron wave function can be considered as a stationary state and it is reasonable to define an electronic Hamiltonian which depends parametrically on the nuclear coordinates

$$H_{el}(R) = T_{el} + V_{el-nuc} + V_{el-el} \ . \tag{2.10}$$

The solutions of the time-independent electronic Schrödinger will give the stationary electronic wave functions $\phi_a(r,R)$ for a given nuclear configuration

$$H_{el}(R)\psi_a(r,R) = E_a(R)\phi_a(r,R) \ . \tag{2.11}$$

23

These solutions define a complete basis in the electronic Hilbert space in which the molecular wave wave function can be expanded as follows

$$\Psi(r,R) = \sum_a \chi_a(R)\phi_a(r,R) . \tag{2.12}$$

The expansion coefficients $\chi_a(R)$ depend only on the nuclear configuration and can be interpreted as nuclear wave function. Using this expansion within Eq. 2.8 yields an equation for the nuclear wave function which reads

$$T_{nuc}\chi_a(R) + \sum_b \Theta_{ab}\chi_b(R) = (\epsilon - E_a(R))\chi_a(R) . \tag{2.13}$$

Here $\Theta_{ab}$ are the so-called nonadiabaticity operators [48] which are responsible for transitions between individual adiabatic electronic states. Further, an effective Potential can be introduced to simplify Eq. 2.13. This effective potential consists of the electron energy for the given electronic state $a$ and the interaction energy between the nuclei

$$U_a(R) = E_a(R) + V_{nuc-nuc}(R) . \tag{2.14}$$

As long as these potential energy surfaces do not cross, the Born-Oppenheimer approximation can be applied, i.e., the nonadiabatic coupling terms $\Theta_{ab}$ in Eq. 2.13 can be neglected. With this approximation and the effective potential the time-dependent Schrödinger equation for the nuclear motion becomes practically solvable. The molecular state vector can be written as product of electronic and nuclear state.

$$|\Psi(t)\rangle = \sum_a |\chi_a(t)\rangle |\phi_a\rangle \tag{2.15}$$

The Hamiltonian for the nuclear motion in different electronic states can be defined using the effective potentials

$$\hat{H}_{mol} = \sum_a |\phi_a\rangle U_a \langle\phi_a| \tag{2.16}$$

and the respectively the time dependent Schrödinger equation for the nuclear motion in a specific electronic state

$$i\hbar \frac{\partial}{\partial t} \langle \phi_a | \Psi(t) \rangle = i\hbar \frac{\partial}{\partial t} |\chi_a(t)\rangle = \langle \phi_a | \hat{H}_{mol} | \phi_a \rangle |\chi_a(t)\rangle \tag{2.17}$$

The state vector $|\Psi(t)\rangle$ contains the probability of the molecular system being in a specific electronic state $|\phi_a\rangle$

$$P_a(t) = \left| \langle \phi_a | \Psi(t) \rangle \right|^2 . \tag{2.18}$$

Solving the static version of Eq. 2.17 yields the vibronic eigenstates and energies which can be used to further expand the nuclear wave vector.

$$\langle \phi_a | \Psi(t) \rangle = \chi_a(t) = \sum_\nu c_\nu^a(t) |\chi_\nu^a\rangle \tag{2.19}$$

### 2.2.3. Potential energy surfaces

To build up an accurate model system for the molecule it is essential to have very precise potential energy curves. Basically these PESs can be calculated ab initio by solving the static Schrödinger equation for the electron wave function. If high resolution spectroscopic data for the excitation energies of the molecule are available, it is possible to calculate PESs from this data which are order of magnitudes more precise then those obtained from ab initio calculations. Especially for diatomic molecules these surfaces can be calculated very accurately using the Rydberg-Rees-Klein (RKR) Method [77–80]. The basic idea behind this method is to take the measured excitation energies and fit them to a function giving the energy for a certain vibrational quantum number $\nu$. This can be done using the Dunham expansion where the $\nu$ dependence of the vibrational energies $G_\nu$ and the inertial rotational constants $B_\nu$ are represented by a power series

$$G_\nu = \sum_{l=0} Y_{l,0} \left( \nu + \frac{1}{2} \right)^l \tag{2.20}$$

$$B_v = \sum_{l=1} Y_{l,1} \left( v + \frac{1}{2} \right)^l \qquad (2.21)$$

using the Dunham coefficients $Y_{l,k}$. These functions are then used to calculate the Klein integrals which yield the inner and outer turning points of the potential. There exist two programs written by Robert J. Le Roy from the University of Waterloo. The first is called RKR1 [81] and computes RKR PESs from given Dunham coefficients and the second one LEVEL [82], a program to calculate eigenenergies from a given PES, which was used to cross check the results of the RKR calculation. With the effective PES for a certain electronic state $a$ given, the molecular Schrödinger equation now reads

$$H_a(R)\chi_a(R) = \left( T_{nuc} + U_a(R) \right) \chi_a(R) = \epsilon \chi_a(R) \qquad (2.22)$$

where $H_a$ is the nuclear Hamiltonian for the electronic state $|\phi_a\rangle$. So the complete time dependent Schrödinger equation can be written as

$$i\frac{\partial}{\partial t} |\Psi(t)\rangle = \sum_a |\psi_a\rangle \hat{H}_a \langle \psi_a|\Psi(t)\rangle \;. \qquad (2.23)$$

### 2.2.4. Interaction with electric fields

To include the interaction with a laser field in the nuclear Schrödinger equation an interaction Hamiltonian $\hat{H}_{field}(t)$ is added to Eq. 2.6

$$i\frac{\partial}{\partial t} |\Psi(t)\rangle = \hat{H}_{mol} |\Psi(t)\rangle + \hat{H}_{field}(t) |\Psi(t)\rangle \;. \qquad (2.24)$$

The interaction Hamiltonian contains the coupling between the electric field and the molecule, to arrive at an equation for this Hamiltonian the dipole approximation can be used, which gives

$$H_{field}(t) = -\hat{\mu}\mathbf{E}(t) \qquad (2.25)$$

for the interaction Hamiltonian. $\hat{\mu}$ is the operator of the electronic dipole moment which is responsible for the radiative coupling of the molecular states. It is the key molecular property which mediates its interaction with the light. The dipole operator consist of the transition dipole moments $\mu_{ab}$ between two electronic states $a$ and $b$

$$\hat{\mu} = \sum_{a,b} |\phi_a\rangle \, \hat{\mu}_{ab} \, \langle\phi_b| \, . \tag{2.26}$$

The transition dipole moment depends on the nuclear coordinates and can be calculated as follows

$$\mu_{ab}(R) = \int dr \, \phi_a(r,R) \left( \sum_i -er_i \right) \phi_b(r,R) \, . \tag{2.27}$$

In most cases it is sufficient to approximate the transition dipole moment as a constant. Therefore the nuclear Schrödinger equation for a specific electronic state $a$ takes the form

$$i\frac{\partial}{\partial t} |\chi_a(t)\rangle = \hat{H}_a |\chi_a(t)\rangle + \sum_b \hat{\mu}_{ab} \mathbf{E}(t)\chi_b(t) \, . \tag{2.28}$$

In this framework the light induced vibrational dynamics manifest themselves as motion of the nuclear wave packet $\chi_a(t)$. For the numerical solution of the time-dependent Schrödinger equation the wave function is, for example, represented on a spatial grid [83] or expanded in a basis defined by the eigenstates of the system

$$|\Psi(t)\rangle = \sum_n c_n(t) |n\rangle \, . \tag{2.29}$$

The latter approach yields a set of coupled differential equations for the expansion coefficients

$$\frac{\partial}{\partial t} c_n(t) = -\frac{i}{\hbar} \left( H_{nn}c_n(t) - \sum_m \langle n|\hat{\mu}|m\rangle \, E(t)c_m(t) \right) \, . \tag{2.30}$$

Since these equations are first-order differential equations, in principle all numerical tools solving these could be applied, such as adaptive Runge-Kutta [84] or

predictor-corrector schemes. Over the years however other efficient and meanwhile widely used methods (e.g. split operator, Chebyshev, Lanczos) have been developed, an overview is given in Ref [85]. Some of the advantages are that they allow accurate control over the propagation error, make a balanced overall treatment possible by using the Fourier representation and usually conserve the constants of motion. Using these wave packet methods the time evolution of the complete wave function is calculated. This approach makes it possible to monitor the dynamics in the molecular system in a very intuitive way. However, even for rather simple molecules like the diatomic iodine the number of differential equations which need to be solved can exceed a number of $10^4$ if the rotational and vibrational motions of the nuclei are considered. As mentioned above the usage of wave packets on electronic surfaces is restricted by the validity of the adiabatic approximation. For systems which exhibit phenomena like strong electronic and vibrational couplings, fast vibrational relaxation or dissipative effects alternative methods are needed [86]. Also for larger multidimensional systems a complete wave packet calculation would exceed our computational resources, therefore further approximative methods like multiconfiguration time-dependent Hartree (MCTDH) [87–89] have to be used.

### 2.2.5. Calculation of nonlinear optical response

The fundamental observable in spectroscopy is the molecular polarization which is induced by the electrical field of the incident laser pulses. This electric field can be described using the ansatz

$$\mathbf{E(t)} = \sum_n E_n f_n(t - T_n) \left( e^{-i\omega_n(t-T_n)+i\mathbf{k}_n x} + e^{i\omega_n(t-T_n)-i\mathbf{k}_n x} \right) \tag{2.31}$$

where $E_n$ is the amplitude, $f_n(t)$ the shape, $\omega_n$ the frequency, $\mathbf{k}_n$ the wave vector and $T_n$ the temporal center of laser pulse $n$. Using this expression in the time-dependent Schrödinger equation 2.28 allows to calculate the evolution of the molecular wave function during the excitation process with the FWM pulses. The molecular polarization is then given as the expectation value of the molecular dipole

moment[8, 16]

$$P(t) \equiv \langle \Psi(t)|\hat{\mu}|\Psi(t)\rangle \; . \tag{2.32}$$

This is the total polarization field of the molecule containing all powers of the electric field. As explained before, in FWM spectroscopy a special beam geometry is used to single out a specific dynamical pathway which makes it necessary to decompose the total polarization and single out those terms which contribute to the specific direction given by three different incident wave vectors. Since the electric field strength of the laser pulses is weak an perturbative expansion of the polarization in powers of the field strength is sufficient to describe the optical response of the system. This method will be described in the next paragraph. It is also possible to calculate the contributions of specific pathways in a non-perturbative manner directly from the exact solutions of the time dependent Schrödinger equation [22, 90–94]. This would circumvent the multiple time-integrals appearing in the perturbative treatment but therefore need many parallel propagations of the wave function. This method will also be detailed in the following.

**Perturbative approach**

The expansion of the polarization field in powers of the field strength reads

$$P(t) \equiv \langle \Psi(t)|\hat{\mu}|\Psi(t)\rangle = P^{(1)}(t) + P^{(2)}(t) + P^{(3)}(t) \; . \tag{2.33}$$

The signal of the FWM processes is generated by the third-order polarization $P^{(3)}(t)$. To calculate this, the wave function of the system is expanded in terms of the applied laser field strength

$$|\Psi(t)\rangle = |\Psi^{(0)}(t)\rangle + \sum_{n,m,l} \left( |\Psi^{(1)}_{\mathbf{k}_n}(t)\rangle + |\Psi^{(2)}_{\mathbf{k}_n,\mathbf{k}_m}(t)\rangle + |\Psi^{(3)}_{\mathbf{k}_n,\mathbf{k}_m,\mathbf{k}_l}(t)\rangle \right) \; . \tag{2.34}$$

Here the $\mathbf{k}_n$ denotes the different laser pulses. Since there are three different laser pulses, each successive interaction with the pulses has to be considered. The wave

functions at each order can be calculated iteratively

$$|\Psi_{\mathbf{k}_i,\mathbf{k}_j}^{(n)}(t)\rangle = -\frac{i}{\hbar}\int_0^t dt' e^{-i\hat{H}_{mol}(t-t')/\hbar}\mathbf{E}_j(t)\hat{\mu}|\Psi_{\mathbf{k}_i}^{(n-1)}(t)\rangle \ , \tag{2.35}$$

where $\mathbf{E}_j(t)$ is the electric field of one pulse with wave vector $\mathbf{k}_i$. Using this expansion together with Eq. 2.32 results in terms for the expansion of $P(t)$.

$$
\begin{aligned}
P^{(0)}(t) &\equiv \langle\Psi^{(0)}(t)|\hat{\mu}|\Psi^{(0)}(t)\rangle \\
P^{(1)}(t) &\equiv \langle\Psi^{(0)}(t)|\hat{\mu}|\Psi^{(1)}(t)\rangle + c.c. \\
P^{(2)}(t) &\equiv \langle\Psi^{(0)}(t)|\hat{\mu}|\Psi^{(2)}(t)\rangle + c.c. + \langle\Psi^{(1)}(t)|\hat{\mu}|\Psi^{(1)}(t)\rangle \\
P^{(3)}(t) &\equiv \langle\Psi^{(0)}(t)|\hat{\mu}|\Psi^{(3)}(t)\rangle + c.c. + \langle\Psi^{(1)}(t)|\hat{\mu}|\Psi^{(2)}(t)\rangle + c.c. \tag{2.36}
\end{aligned}
$$

The permanent dipole moment $P^{(0)}(t)$ and the second order term $P^{(2)}(t)$ give zero when averaged over an isotropic media. $P^{(1)}(t)$ is the linear response and $P^{(3)}(t)$ the third order polarization which is needed to calculate the FWM signals. The terms $P^{(3)}(t)$ represent overlaps of wave packets moving on different potential energy surfaces and creating non-vanishing transition dipole moments which interact with light. Using this expansion and eq. 2.34 the relevant spectroscopic pathways for the FWM process with the phase-matching condition $\mathbf{k}_S = \mathbf{k}_1 - \mathbf{k}_2 + \mathbf{k}_3$ can be determined.

$$
\begin{aligned}
P^{(3)}(t) &= \left(\langle\Psi^{(0)}(t)|\hat{\mu}|\Psi_{\mathbf{k}_1,\mathbf{k}_2,\mathbf{k}_3}^{(3)}(t)\rangle + \langle\Psi^{(0)}(t)|\hat{\mu}|\Psi_{\mathbf{k}_2,\mathbf{k}_1,\mathbf{k}_3}^{(3)}(t)\rangle\right) + c.c. \\
&+ \left(\langle\Psi_{\mathbf{k}_1}^{(1)}(t)|\hat{\mu}|\Psi_{\mathbf{k}_2,\mathbf{k}_3}^{(2)}(t)\rangle + \langle\Psi_{\mathbf{k}_3}^{(1)}(t)|\hat{\mu}|\Psi_{\mathbf{k}_2,\mathbf{k}_1}^{(2)}(t)\rangle\right) + c.c. \ . \tag{2.37}
\end{aligned}
$$

This expression includes all possible time orderings of the interacting pulses. For the numerical calculation of the third order polarization nine wave functions need to be propagated using the propagation methods described above. From the polarization the frequency resolved spectrum can be evaluated by a Fourier integral.

$$S(\omega) = \left|\int P_{\mathbf{k}_S}(t)e^{-i\omega t}dt\right|^2 \tag{2.38}$$

This calculation is then performed for different time delays of the laser pulses which in turn gives the time and frequency resolved FWM signal.

**Non-perturbative approach**

The polarization calculated from the exact propagated wave function is the total polarization (Eq. 2.32) of the system. To single out a specific pathways of wave vectors, which are responsible for a particular signal, further analysis is needed. This makes the calculation of the polarization from the exact propagated wave function more complicated but has the advantage of being not restricted to small laser field strengths. One method to resolve this problem is to compute the total polarization at different phase angles of the involved fields [22, 90]. This results in a system of linear equations and the solution yields the desired polarizations. In this method different sets of phases $\phi_k$ are added to the electric field

$$E(t) = \sum_n \epsilon_n f_n(t - T_n) \left( e^{-i\omega_n(t - T_n + \phi_k) + i\mathbf{k}_n x} + e^{i\omega_n(t - T_n + \phi_k) - i\mathbf{k}_n x} \right) \tag{2.39}$$

which allow for a Fourier decomposition of the polarization

$$P(t) = 2\Re \sum_{l,n,m}^M P_{l,n,m}(t) e^{-i(l\mathbf{k}_1 + m\mathbf{k}_2 + n\mathbf{k}_3)} \tag{2.40}$$

with $P_{l,n,m}(t)$ being the polarization filed emitted in the direction $\mathbf{k}_S = l\mathbf{k}_1 + n\mathbf{k}_2 + m\mathbf{k}_3$. For the DFWM scheme that would be $lmn = (1, -1, 1)$ The propagations are then performed for different phase and wave vector combinations

$$P(t, \phi_1, \phi_2, \phi_3) = 2\Re \sum_{l,n,m} P_{l,n,m}(t) e^{-i(l\phi_1 + m\phi_2 + n\phi_3)} \tag{2.41}$$

which yields a linear system of equations to calculate the polarization $P_{\mathbf{k}_S}$ in a specific direction. To resolve the polarization for the DFW process 12 different combinations of phases are needed and thus also 12 wave packet propagations [22].

# 3. Vibrational dynamics in higher electronic excited states of iodine

By using a combination of an initial pump pulse and a degenerate four-wave mixing (DFWM) process, we show that an interrogation of the vibrational dynamics occurring in high-lying electronic states of molecules is possible. As a test case, experiments applying this technique to iodine where analyzed and discussed using the results of wave packet simulations. In the experiment an initial pump pulse is used to populate the $B$ $(^3\Pi_u^+)$ state of molecular iodine in the gas phase. By introducing an internal time delay in the subsequent DFWM process, which is resonant with the transition between the B state and a higher lying ion-pair state, the vibrational dynamics of the $B$ state as well as of the ion-pair state could be observed. From the possible ion-pair states, the states of even symmetry are investigated, which are accessible by an one-photon transition from the $B$ state. By a proper choice of the wavelengths used for the pump and DFWM beams, the dynamics of ion-pair states belonging to two different tiers are monitored. Very good agreement between experimental and theoretical results are observed in most of the studied wavelength combinations.

## 3.1. Introduction

To access the excited state dynamics, the DFWM process can be combined with an initial pump pulse. In this scheme, a femtosecond pump pulse is used to initiate dynamics in the molecular system under investigation. The DFWM process is then used to probe the resulting dynamics. Motzkus *et al.* [95] used this pump DFWM technique to study unimolecular and bimolecular systems in gas phase. In these experiments, the DFWM process itself was not time-resolved, it was rather used to replace the probe pulse in a pump-probe scheme. Also excited state dynamics of complex polyatomic molecules in the condensed phase have been investigated using this technique [96, 97]. Recently, it was shown that with the application of a fully time-resolved combination of an initial pump and a DFWM process it is possible to access the dynamics in ion pair states of molecular iodine [23, 24]. Here, we use quantum dynamical calculations to analyze results of pump-DFWM experiments on the $I_2$. Simulations of pump-DFWM for different time orderings of the pulses and different combinations of pump and DFWM wavelengths are presented and compared to the experimental findings.

The iodine molecule is well characterized by different spectroscopical techniques and also a theoretical description of different FWM processes in this system has been given as mentioned above; additional information can be found, e.g., in Refs. [20, 33, 98, 99]. Therefore, the iodine molecule presents itself as ideal model system to investigate the efficiency of experimental techniques because these systems allow for a complete quantum dynamical description. The ion pair states in iodine form three clusters each consisting of three pairs of gerade (g) and ungerade (u) states. In the present study we concentrate on the first and second tier. The first tier consists of the states $D'(2_g)$, $\beta(1_g)$, $D\ (0_u^+)$, $E\ (0_g^+)$, $\gamma(1_u)$, and $\delta(2_u)$ dissociating into $I^-(^1S)$ and $I^+(^3P_2)$ ions. These states lie around 40,000 cm$^{-1}$ above the ground state. The second tier lies about 47,000 cm$^{-1}$ above the ground state. Its states dissociate into the ions $I^-(^1S)$ and $I^+(^3P_1)$. Since these states are characterized by large equilibrium inter-nuclear distances and similar molecular constants they are not easily accessible because a transitions from the ground state would correspond to a large Frank-Condon shift. Additionally, the selection rules for optical transitions have to be taken into account. Hence, transitions are only allowed between states of different symmetries

$$g \Longleftrightarrow u$$

and when the change of the projection of the total angular momentum $\Omega$ is

$$\Delta\Omega = 0, \pm 1$$
$$0^+ \Longleftrightarrow 0^+, 0^- \Longleftrightarrow 0^- \; .$$

Therefore, only states of odd symmetry can be accessed from the ground state via one photon processes. There are different techniques used in the frequency domain to analyze these ion-pair states and several of these ion-pair states are characterized experimentally [100]. In most of these studies the excited $B$ state is used as an intermediate state since it is readily accessible from the ground $X$ state. A multitude of detailed studies of the ion pair states using frequency domain experiments have been performed [36–41], but only a few time domain investigations are known [101, 102]. To access these higher lying states, multi photon processes [101] or vacuum ultra-violet pulses have to be used [102]. These techniques were successful in observing ion-pair states belonging to the first tier possessing odd symmetry.

In the following, we discuss experiments where the dynamics of the ion-pair states have been monitored using a combination of an initial pump laser pulse and subsequent time-resolved FWM spectroscopy. In this two-step process, firstly the $B$ state is populated by the pump pulse. Then, in a second step, the ion-pair states are accessed with a time-resolved DFWM process. For a more detailed analysis, different wavelengths are used for both initial pump and DFWM laser pulses. The experimental methodology of this pump-DFWM scheme is depicted in Fig. 3.1. In order to analyze and verify if the observed dynamics can be assigned to the ion pair states, quantum dynamical simulations of the pump-DFWM process have been performed. The model system for the simulations was reduced to contain only the relevant ion pair states. By comparing the results of these simulations it could be shown, that the pump-DFWM process is an efficient tool to monitor dynamics of specific higher lying electronic states.

This chapter is organized as follows: First, the theoretical model for the iodine molecule is introduced and in a next step, the specific pump-DFWM processes in this molecule are detailed. In the subsequent section the experimental and theoretical results are discussed and compared to each other. The chapter ends with conclusions.
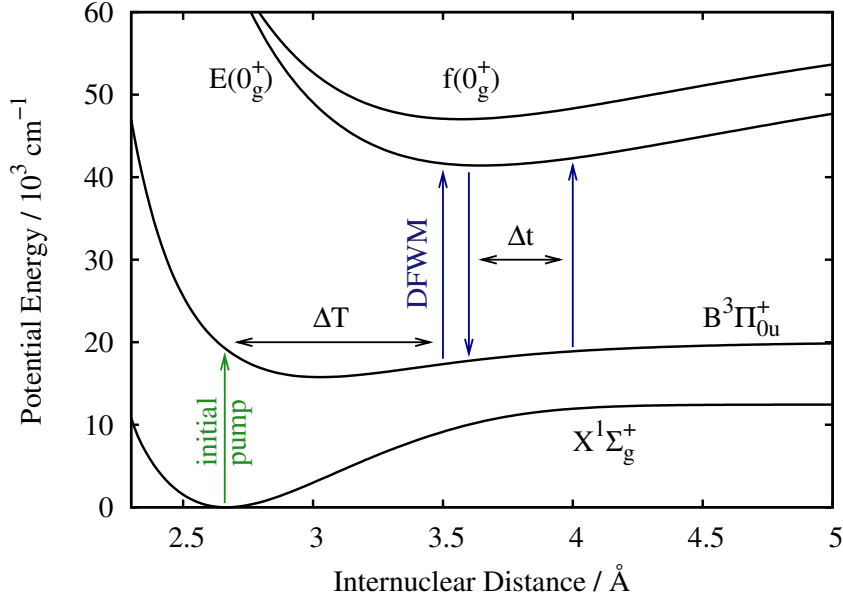
**Figure 3.1.:** Schematic diagram of the time-resolved pump-DFWM experiment performed on molecular iodine. A initial pump pulse is used to first populate the *B* state through a transition from the ground state. The dynamics in the *B* state and the ion pair states is then interrogated by a time-resolved DFWM process.

## 3.2. Model System

The model used for the I$_2$ molecule takes into account three electronic states, the ground state, the first excited state (here, the *B* state) and a further excited state, which corresponds to one of the ion pair states. These electronic states are coupled by the electric field of the laser pulses. The system Hamiltonian is given by

$$\hat{H}(t) = \hat{H}_{\text{mol}} + \hat{H}_{\text{int}}(t) \,. \tag{3.1}$$

Here, $H_{\text{mol}}$ denotes the Hamiltonian of the unperturbed system, which can be given in terms of the vibrational eigenstates of the electronic potential energy surfaces

$$\hat{H}_{\text{mol}} = \sum_{a,\nu} |a\nu\rangle \langle a\nu| \hbar\omega_{a\nu} \,. \tag{3.2}$$

Here the abbreviation $|a\nu\rangle$ is used for the electronic and vibrational eigenstates $|\phi_a\rangle |\chi_\nu^a\rangle$. In order to model the system accurately, we used Rydberg-Rees-Klein (RKR) potentials based on Dunham coefficients from Refs. [37, 40, 103] to calcu-

late the eigenstates. The coupling of the molecules to the electric field of the laser pulses $\mathbf{E}(t)$ through the dipole operator $\hat{\mu}$ was treated in dipole approximation, which can be written as

$$\hat{H}_{\text{int}} = -\hat{\mu}\mathbf{E}(t) \,. \tag{3.3}$$

The dipole matrix elements were calculated from the initial and final vibrational wave functions

$$\langle av | \hat{\mu} | a'v' \rangle = \mu_{a,a'} \langle \chi_v^a(r) | \chi_{v'}^{a'}(r) \rangle \tag{3.4}$$

with the electronic part of the dipole matrix element $\mu_{a,a'}$ and the Frank-Condon factor $\langle \chi_v^a(r) | \chi_{v'}^{a'}(r) \rangle$. Furthermore, the laser pulses were assumed to have the form

$$\mathbf{E}(t) = \sum_n \mathbf{E}_n(t) = \sum_n \epsilon(t - T_n) e^{-i\omega_n(t-T_i)+i\mathbf{k}_n\mathbf{x}} \tag{3.5}$$

with Gaussian shaped envelopes $\epsilon(t)$ centered at $T_n$, frequencies $\omega_n$ and wave vectors $\mathbf{k}_n$. To simulate the DFWM signal, the third-order polarization $P^{(3)}(t)$ was calculated using perturbation theory, which allows to select only those spectroscopic pathways, which contribute to the polarization in the direction of the DFWM signal

$$\mathbf{k}_s = \mathbf{k}_1 - \mathbf{k}_2 + \mathbf{k}_3 \,. \tag{3.6}$$

Within perturbation theory the third-order polarization induced in the system is given by

$$P^{(3)}(t) \equiv \langle \Psi^{(0)}(t) | \hat{\mu} | \Psi^{(3)}(t) \rangle + c.c. + \langle \Psi^{(1)}(t) | \hat{\mu} | \Psi^{(2)}(t) \rangle + c.c. \tag{3.7}$$

where $c.c.$ denotes the complex conjugate. The wave functions in the different orders can be calculated iteratively [104]

$$i\hbar \frac{\partial}{\partial t} |\Psi^{(n)}(t)\rangle = \hat{H}_{\text{mol}} |\Psi^{(n)}(t)\rangle + \hat{H}_{\text{int}}(t) |\Psi^{(n-1)}(t)\rangle \,. \tag{3.8}$$

These equations were solved in energy representation. In this representation it is possible to reduce the the system to those vibrational states, which were populated during the excitation processes. This helped to reduce the time for the numerical calculations drastically. Furthermore, the characteristics of the vibrational population in the different electronic states involved can be tracked easily during the excitation processes in the simulation. Using only those spectroscopic pathways, which contribute to the polarization in this direction results in [8]

$$
\begin{aligned}
P^{(3)}(t) &= \left( \langle \Psi^{(0)}(t)|\hat{\mu}|\Psi^{(3)}_{\mathbf{k}_1,\mathbf{k}_2,\mathbf{k}_3}(t)\rangle + \langle \Psi^{(0)}(t)|\hat{\mu}|\Psi^{(3)}_{\mathbf{k}_2,\mathbf{k}_1,\mathbf{k}_3}(t)\rangle \right) + c.c. \\
&+ \left( \langle \Psi^{(1)}_{\mathbf{k}_1}(t)|\hat{\mu}|\Psi^{(2)}_{\mathbf{k}_2,\mathbf{k}_3}(t)\rangle + \langle \Psi^{(1)}_{\mathbf{k}_3}(t)|\hat{\mu}|\Psi^{(2)}_{\mathbf{k}_2,\mathbf{k}_1}(t)\rangle \right) + c.c. \,.
\end{aligned}
\tag{3.9}
$$

In the simulations this polarization was calculated over a time range of 10 ps and then Fourier transformed to get the spectra $P(\omega, \Delta t)$, which correspond to the spectra measured in the experiment with the CCD camera. This results in transients at every detection wavelength. However, for the present molecular system the transients were found to be rather independent of this wavelength. Therefore, we have used the integrated signal $S(\Delta t)$, which was obtained by integrating over all detection wavelengths, to compare simulations and experiments

$$
S(\Delta t) = \int_{-\infty}^{\infty} d\omega |P(\omega, \Delta t)|^2 \,.
\tag{3.10}
$$

For this comparison, the Fourier transform of this quantity was calculated.

## 3.3. Detailed pump-DFWM scheme for the iodine experiment

In the experiment, a wave packet is excited from the ground state to the $B$ state. Following the selection rules, only states of even symmetry can be accessed from the $B$ state. This restricts the states, which can be involved in the pump-DFWM process to those listed in table 3.1. The ion pair states of iodine have been investigated earlier using frequency-domain spectroscopy [39, 105]. In our studies, we aim to explore the dynamic properties of the ion pair states as well as of the $B$

**Table 3.1.:** Molecular constants for the excited iodine $B$ state and the ion pair states relevant for the present study.

| State | $T_e$ / cm$^{-1}$ | $\tilde{\nu}_e$ / cm$^{-1}$ |
|---|---|---|
| $B({}^3\Pi_0 u^+)$ | 15,641 | 127 |
| $\beta(1_g)$ | 40,821 | 105 |
| $E(0_g^+)$ | 41,411 | 101 |
| $f(0_g^+)$ | 47,025 | 104 |
| $G(1_g)$ | 47,559 | 106 |

state. The experimental methodology of the pump-DFWM scheme employed in the experiments is depicted in Fig. 3.1. The initial pump pulse, which is in resonance with a transition from $X$ to $B$ , excites the molecule from the ground ($X$ ) state to the first excited state ($B$ ). Since a spectrally broad femtosecond pulse is used, this excitation process creates a superposition of vibrational states, a wave packet, in the $B$ state. After a time delay $\Delta T$, the DFWM process is then used to probe the $B$ state wave packet. The wavelength of DFWM beams was varied to be resonant with transitions from the $B$ state to the ion pair states of the first ($E$ ($0_g^+$)) and second tier (f($0_g^+$)). As was mentioned above, DFWM involves the interaction of three laser beams of the same wavelength with the sample, leading to the generation of a coherent fourth beam also of the same wavelength. In the experiments, one of the laser pulses was time delayed relatively to the other two time coincident laser pulses over a time range from $\Delta t = -40$ ps to $\Delta t = 40$ ps; the time zero of the DFWM process, $\Delta t = 0$ ps, was defined by the temporal overlap of all three pulses. $\Delta T$ on the other hand was measured as time delay between the initial pump and the two time coincident DFWM pulses. Scanning $\Delta t$ yields a time-dependent signal, from which the dynamics of the $B$ state and the ion pair states can be obtained. The time of the initial pump pulse was set to $\Delta T_0 = 42$ ps to ensure that the $B$ state is populated for all time delays $\Delta t$. For negative time delays, $\Delta t < 0$, there are two spectroscopic pathways, which mainly contribute to the signal [32]

$$
\begin{aligned}
P^{(3)} &= \left\langle \Psi_B^{(0)} \middle| \hat{\mu} \middle| \Psi_{\mathbf{k}_3-\mathbf{k}_2+\mathbf{k}_1}^{(3)} \right\rangle \\
&+ \left\langle \Psi_{\mathbf{k}_2-\mathbf{k}_1}^{(2)} \middle| \hat{\mu} \middle| \Psi_{\mathbf{k}_3}^{(1)} \right\rangle + c.c. \, .
\end{aligned}
\tag{3.11}
$$

Here, $|\Psi_B^0(t)\rangle$ denotes the initial state population of the DFWM process; this population being prepared by the initial pump laser via an excitation from the ground state to the $B$ state. Thus, $|\Psi_B^0(t)\rangle$ is describing a moving wave packet in the $B$ state and not a static population like in a ground state FWM experiment. In the simulation, the initial state was calculated by an exact propagation of the wave functions in the $X$ and $B$ states starting from the thermally (320 K) populated ground state $X$, which is coupled to the $B$ state by the electric field of the initial pump pulse. The first term in Eq. (3.11) corresponds to the process where a wave packet is created by the excitation with pulse $\mathbf{k}_3$ in the ion pair state, which then evolves freely in time until it is probed by a two photon process with the pulses $\mathbf{k}_2$ and $\mathbf{k}_1$. The second term emerges from the overlap between the wave packet prepared by $\mathbf{k}_3$ and the second-order wave packet created by absorptions by $\mathbf{k}_2$ and stimulated emission from $\mathbf{k}_1$. If the DFWM process starts with the preparation of an ion-pair state wave packet, which is then probed after a delay time $\Delta t$, one would expect to see in the transients the dynamics of the ion pair states only. However, in the case of the employed pump-DFWM scheme the initial state $|\Psi_B^0(t)\rangle$ is already a moving wave packet in the $B$ state. Thus, the DFWM signal also depends on the timing $\Delta T + \Delta t$ between the initial pump pulse and the DFWM probe pulse ($\mathbf{k}_3$) for negative time delays $\Delta t < 0$, where it acts as pump pulse of the DFWM process. Hence, the transients also show the dynamics of the $B$ state vibrational motion. For positive time delays a further pathway has to be considered, which leads to the expression [32]

$$
\begin{aligned}
P^{(3)} &= \left\langle \Psi_B^{(0)} \middle| \hat{\mu} \middle| \Psi_{\mathbf{k}_1 - \mathbf{k}_2 + \mathbf{k}_3}^{(3)} \right\rangle \\
&+ \left\langle \Psi_{\mathbf{k}_2 - \mathbf{k}_1}^{(2)} \middle| \hat{\mu} \middle| \Psi_{\mathbf{k}_3}^{(1)} \right\rangle + \left\langle \Psi_{\mathbf{k}_2 - \mathbf{k}_3}^{(2)} \middle| \hat{\mu} \middle| \Psi_{\mathbf{k}_1}^{(1)} \right\rangle + c.c.
\end{aligned}
\tag{3.12}
$$

for the third-order polarization. Here, the first two terms correspond to the dynamics on the $B$ state since in both cases a $B$ state wave packet is created by a two photon process involving the pulses $\mathbf{k}_1$ and $\mathbf{k}_2$, for which the time delay $\Delta T$ is fixed. This is then probed after a time delay $\Delta t$ with the $\mathbf{k}_3$ pulse. Since the third term also depends on the dynamics on the ion pair state, here, in any case ground and excited state dynamics contributions will determine the transient.
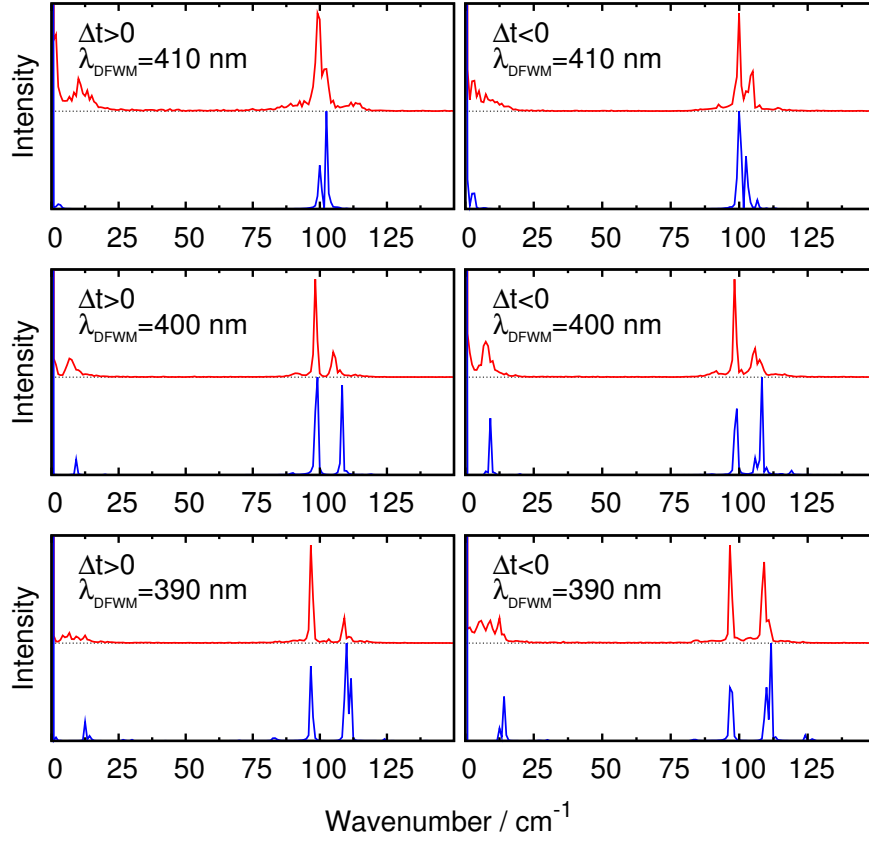
**Figure 3.2.:** Fourier transform spectra calculated from the DFWM transients obtained for $\lambda_{ip} = 620$ nm at different DFWM wavelengths as stated in the individual panels. In each panel the upper line shows the FT of the experimental transient and the lower line the simulated one. The results for positive time delays are shown in the left and for negative time delays in the right panels.

## 3.4. Results and Discussion

Different combinations of initial pump and DFWM wavelengths were used to explore the dynamics on different states. The ion pair states used for the simulation were chosen according to the total energy of the different combinations of initial pump and DFWM wavelengths. For energies accessing the first tier of ion pair states the state $E\,(0_g^+)$ was used while the $f(0_g^+)$ state was used for energies accessing the second tier. Although transitions to the $G(1_g)$ and the $\beta(1_g)$ states are possible these states were neglected in the simulations because $\Delta\Omega = 0$ transitions are more than an order of magnitude stronger than those with $\Delta\Omega = 1$ [106, 107]. The first

combination of wavelengths to explore the $E$ $(0_g^+)$ ion pair state consists of an initial pump wavelength of $\lambda_{ip}$=620 nm and a DFWM wavelength, which was varied between 390 and 410 nm. The transients were recorded for negative and positive time delays $\Delta t$. Here, we do not show the measured and calculated transients but only their Fourier transforms (FTs). The FTs expose all basic features of the transients and in this way the comparison between experiment and simulation becomes more evident. Fig. 3.2 shows the FT of the transients for $\lambda_{ip}$=620 nm and for three different DFWM wavelengths.

The wavenumbers of the 620 nm initial pump and the 390 nm DFWM pulses sum up to 41,770 cm$^{-1}$, which is far below the minimum of the potentials belonging to the second tier ion pair states. Therefore, only transitions to states of the first tier are possible and only transitions from the $B$ to the $E$ $(0_g^+)$ state need to be included in the simulation as stated above. As listed in table 3.1, for the $E$ $(0_g^+)$ state the vibrational wavenumber is $\omega_e = 101$ cm$^{-1}$ and hence the peaks corresponding to this have to appear below this value, since the potential is anharmonic with a decreasing level spacing for higher vibrational states. The FTs of the transients for the 620/390 nm excitation given in the lower panels of Fig. 3.2 show prominent peaks at 97 cm$^{-1}$ for negative as well as for positive time delays, which corresponds to the spacing of the vibrational states in the $E$ $(0_g^+)$ accessed by the 390 nm pulse. As discussed above, also the dynamics of the $B$ state is expected to show up in the transients recorded with both positive and negative time delays. The vibrational levels excited by the initial pump pulse in the $B$ state are in the proximity of $v = 9$, which corresponds to a spacings of 109.6 and 108.1 cm$^{-1}$. Since the initial pump wavelength is the same and only the DFWM wavelength is changed, peaks arising from the wave packet in the $B$ state are therefore expected to show up at these wavenumber positions. The FTs of the transients for 620/390 nm excitation show a sharp peak at around 109 cm$^{-1}$, which can be assigned to the $B$ state dynamics. Furthermore, a smaller peak can be seen at lower wavenumbers around 12 cm$^{-1}$. This value matches the wavenumber of a beating between the $E$ and $B$ state dynamics.

In a next step the DFWM wavelength was changed to 400 nm and then to 410 nm. The FTs of the so recorded transients are shown in the four upper panels of Fig. 3.2. For a DFWM wavelength of 400 nm a sharp peak at 98.3 cm$^{-1}$ can be seen in the FT for negative and positive time delays. This peak can clearly be assigned to the $E$ state dynamics. Compared to the 620/390 nm experiment it is shifted to a

higher value because now lower vibrational levels are excited, which have a larger spacing. This can also be seen in the FT of the 620/410 nm experiment where the $E$ state peak shifts further up to 100 cm$^{-1}$. Also peaks corresponding to the $B$ state dynamics can clearly be seen in all these FTs. The FTs of the experimental and calculated transients for our model system containing only the $X$, $B$ and $E$ $(0_g^+)$ states agree very well. This leads us to the conclusion that the pump-DFWM scheme gives access to properties of the $E$ $(0_g^+)$ state.

To further examine these findings, we have analyzed other initial pump-DFWM wavelength combinations. For the experiments discussed in the following, the initial pump wavelength was set to 600 nm and the DFWM wavelength was varied between 380 and 420 nm. The results are shown in Fig. 3.3. For the chosen initial pump wavelength vibrational states are accessed in the $B$ state around $v = 9$ where the spacing is 104.3 and 106.1 cm$^{-1}$. For a DFWM wavelength of 380 nm the FTs of the transients are displayed in the lower panels of Fig. 3.3. These spectra show a major peak at 92.5 cm$^{-1}$ for negative as well as for positive time delays. This peak corresponds to the dynamics on the $E$ state. The contribution of the $B$ state dynamics can be found as rather weak peak for positive time delays at approximately 107.5 cm$^{-1}$. For negative time delays the $B$ state dynamics is seen in the FT spectrum with much higher intensity. The reason for the stronger $B$ state contribution was already explained above. Since the initial state of the DFWM process is already a moving wave packet, the DFWM probe pulse for negative time delays $\Delta t < 0$ encounters the population prepared by the initial pump pulse resulting in a strong contribution of the $B$ state dynamics. On the other hand, for positive time delays, the DFWM probe pulse probes the wave packet created by the two time coincident DFWM pump pulses. Since the time delay $\Delta T$ between the initial pump pulse and these two DFWM pump pulses is fixed, the $B$ state contribution for positive time delays is only attributed to the $B$ state wave packet created by the DFWM process.

Also for this initial pump wavelength (600 nm), the DFWM wavelength was increased stepwise from 380 to 420 nm. The FTs of the measured and calculated transients are also presented in Fig. 3.3. In the panels for 380, 390, 400, and 410 nm the shift of the peak corresponding to the $E$ state dynamics is clearly recognizable. The contribution of the $B$ state is different for specific DFWM wavelengths although the initial pump wavelength was not changed. In the FTs for 380, 390
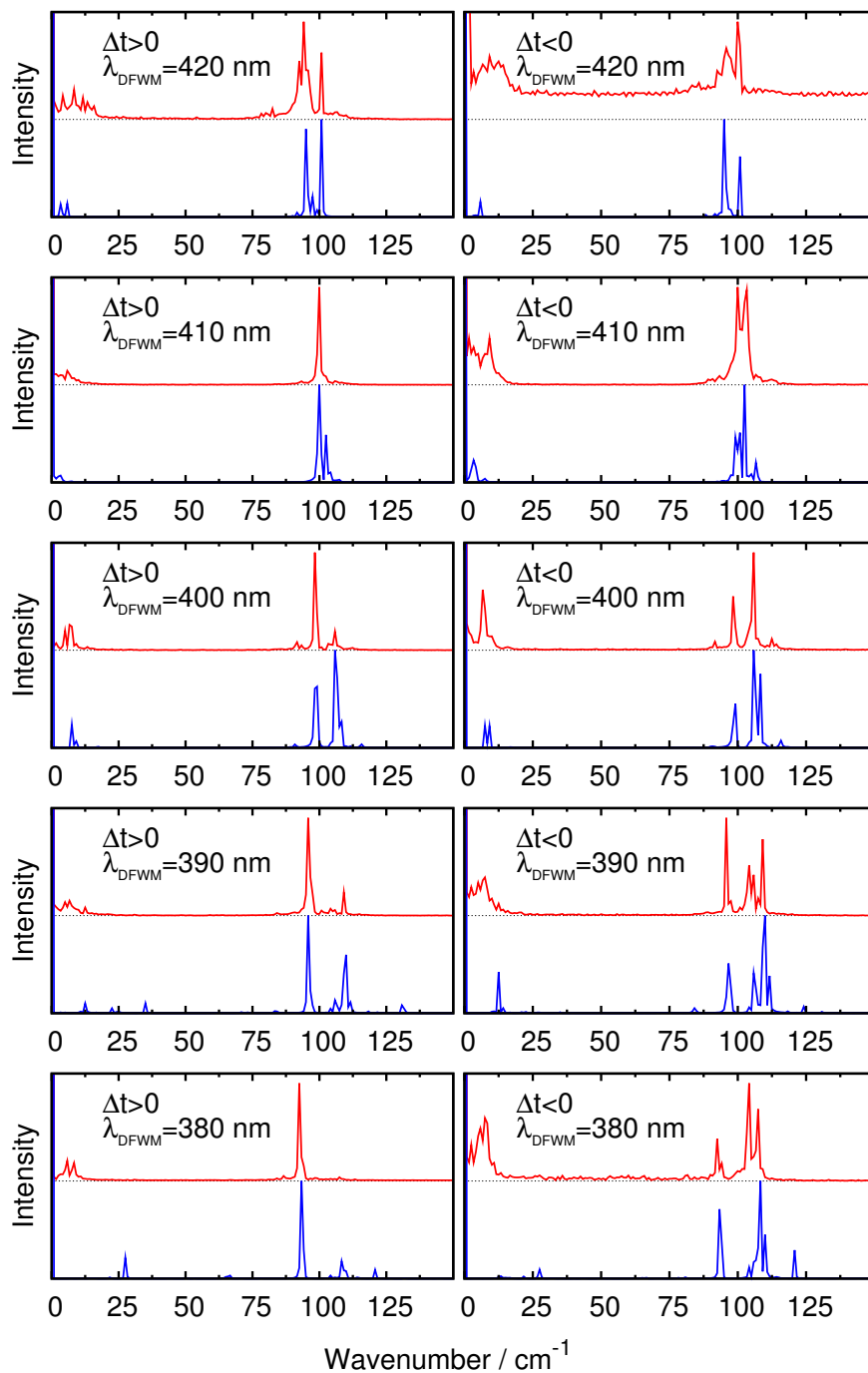
**Figure 3.3.:** Same as in Fig. 3.2 but for $\lambda_{ip} = 600$ nm.

and 400 nm the peaks of the $B$ state dynamics occur at the expected positions, which correspond to the value of the spacings in the range of the vibrational levels populated by the initial pump pulse. However, in the FT of the 410 nm DFWM experiment there are only some closely neighbored peaks around 100 cm$^{-1}$ and for 420 nm there is a peak at 95 cm$^{-1}$ and one at 100 cm$^{-1}$. The total wavenumber for the 600/410 nm combination (41,060 cm$^{-1}$) is close to the wavenumber difference between the vibrational ground state of the $X$ state and the minimum of the $E$ state potential. The total wavenumber for the 600/420 nm combination (40,480 cm$^{-1}$) is even below this value. Thus, only the peak at 100 cm$^{-1}$ can be assigned to the spacing between the lowest vibrational states of the $E$ state and the peak at 95 cm$^{-1}$ must be assigned to a $B$ state contribution. The strong shift of the $B$ state contribution can be explained by the contribution of the second-order wave packet created by the absorption by $\mathbf{k}_2$ and stimulated emission from $\mathbf{k}_1$ or $\mathbf{k}_3$. Since the excitation energy of the 420 nm pulse is slightly below the vibrational ground state of the $E$ state only the lowest vibrational states are excited. In the following stimulated emission the Franck-Condon overlaps to higher vibrational states in the $B$ state are much stronger so that a wave packet at around $v = 15$ is created, which corresponds to the observed spacing of 95 cm$^{-1}$. This could be verified by analyzing the population on the vibrational states in the simulation.

To access the ion pair states of the second tier, which lie around 47,000 cm$^{-1}$, the initial pump wavelength was finally reduced to 540 nm and the DFWM wavelength were set to 325 nm and 335 nm. The total wavenumbers of these combinations are 48,369 cm$^{-1}$ and 49,287 cm$^{-1}$, respectively, which is in both cases above the minimum of the $G(1_g)$ state (see Tab. 3.1). To analyze the transients recorded in these experiments, the FT was calculated and compared to the simulation. The results are shown in Fig. 3.4. For the simulation a model system consisting only of the $X$, $B$, and f$(0_g^+)$ states was used. The simulation of the initial pump process showed that with a 540 nm pulse the vibrational states around $v = 27$ are populated in the $B$ state. This corresponds to a spacing of 75.3 and 77.5 cm$^{-1}$. Peaks at these values and their second harmonic at around 150 cm$^{-1}$ can be seen in the FTs of the transients for 335 nm and 325 nm. From the simulation it became evident, that the transition from the $B$ state to the $f$ state with a 325 nm pulse is very weak compared to that of the 335 nm pulse. For this reason, the FT of the 325 nm transient is "nosier" than the 335 nm FT which can also be seen in the FT of the simulated
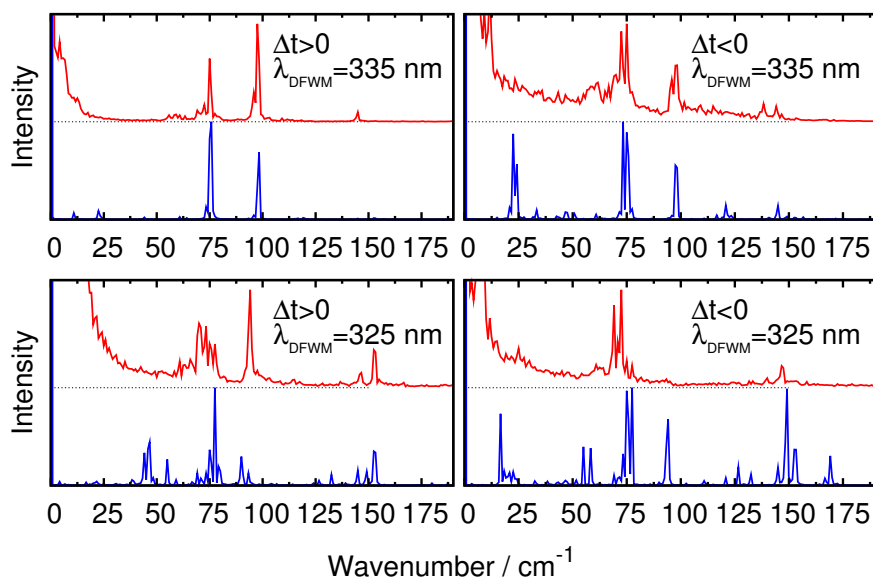
**Figure 3.4.:** Same as in Fig. 3.2 but for $\lambda_{ip} = 540$ nm.

transient, *i.e.,* there are many transitions with very low intensity. Nevertheless, a clear peak at 94.1 cm$^{-1}$ can be seen in the FT of the transient recorded for positive time delays, which can be assigned to the dynamics of the *f* state. For the 335 nm pulses the intensities of the main peaks in the FT are much larger again. Here, sharp peaks corresponding to the *B* and *f* state dynamics are present. The simulation shows in all cases additional peaks at around 25 cm$^{-1}$, which fit the difference between the *B* state and *f* state peaks. These peaks are not evident in the experimental FTs due to the strong background. Although the agreement between the peak intensities in the experimental and theoretical FTs is not very good, the peak positions do coincide quite well. However, this is not surprising taking into account the simplifications made within the theoretical model compared to the real experimental situation. Especially, the deviation of the spectral shapes of the pulses from Gaussian profiles and the slight chirp, which could not be completely avoided in the experiments have considerable influence on the intensities of the contributions seen in the FT spectra as was demonstrated earlier [108, 109].

## 3.5. Conclusions

In the present chapter we have demonstrated that the combination of time-resolved degenerate DFWM and an initial pump pulse is a suitable tool for the investigation of wave packet dynamics on different excited state potential energy surfaces. It could be shown that it is possible to access high-lying ion pair states in molecular iodine and gain information on the dynamics in these states. To verify that the observed dynamics belong to the expected ion pair states, the experimental results were compared to quantum dynamical calculations in model systems containing only the relevant states.This could be verified using quantum dynamical calculations which where needed to identify the contributions if the ion pair states in the experimental measured signal. The calculations were based on a model systems containing only the relevant states and did not incorporate rotational degrees of freedom. Comparing the experimental and theoretical results, good agreement could be found for the simple system under investigation. This leads to the conclusion that the basic features of the transients correspond primary to vibrational dynamics and that such adjusted model systems are a numerical effective way to analyze complex molecular dynamics.

# 4. Vibrational Dynamics in *B* state of molecular Bromine

In this chapter femtosecond pump-degenerate four-wave mixing experiments on molecular bromine are analysed using wave packet calculations. In these experiments the dynamics in the excited *B* state were investigated via transitions to ion pair states. By varying the DFWM wavelength different vibrational energy spacings of the excited *B* state were be observed. Using the results of quantum dynamical calculations for this system, we were able to show that these differences in the transients arise from a substantial contribution of a hot vibrational state of the electronic ground state. Furthermore we show that specific Franck-Condon overlaps between the *B* and an ion pair state can be used to probe different parts of the excited state dynamics individually and therefore indirectly the contributions from different vibrational states in the electronic ground state.

## 4.1. Introduction

The ultrafast dynamics of wave packets in excited states often shows complex behavior, even in diatomic molecules [21]. While the dynamics in iodine, for example, was investigated using time-resolved spectroscopy in detail [110] and has even been proposed as a substance for quantum logic gates [42], bromine is much less studied. In bromine fractional revivals of the *B* state wave packet were observed using pump-probe spectroscopy [29]. Averbukh *et al.* [30] measured the excited state dynamics of bromine by using pump-probe spectroscopy based on ion detection. Their aim was to introduce a general wave packet method for laser isotope separation rather than to monitor the time evolution of the wave packet inside

the bound *B* state. Schmitt *et al.* [28] employed electronically resonant coherent anti-Stokes Raman scattering (CARS) spectroscopy to monitor the excited state dynamics of bromine. No ground state dynamics was observed since the vibrational energy spacing of the ground state of bromine is relatively large ($\approx 325$ cm$^{-1}$). Due to the small bandwidth of the employed laser pulses, therefore, vibrational overtones could not be efficiently excited. Furthermore, also the wave packet dynamics of bromine in condensed phase hosts was investigated in different setups [111, 112].

Recently, pump-degenerate four-wave mixing (DFWM) experiments were performed on iodine to investigate the vibrational dynamics of higher excited states [23, 24]. Experiments performed with time-coincident DFWM pulses, while temporally varying the initial pump pulse, yielded exclusive *B* state dynamics. A scheme employing a time-resolved DFWM, gave access to dynamics of the *B* state as well as higher lying ion-pair states. By employing different wavelengths for the initial pump and DFWM pulses, dynamics of different excited states were accessed. The investigations are now extended to bromine, in which features appear that are qualitatively different from those in iodine. These findings are of significance for time-resolved experiments in general since they show that one can extract molecular details of excited states using pump-DFWM which are otherwise not easily accessible. The experimental methodology employed for the time-resolved measurements on bromine is depicted in Fig. 5.2 and detailed below. The experiments were performed with a constant initial pump wavelength while the DFWM wavelength is varied. Time-coincident DFWM pump pulses are employed to monitor the *B* state dynamics exclusively. Since the wave packet is created by the initial pump pulse, which is then probed by another pulse, a change of wavelength of the probe pulse is not expected to have a distinct influence on the observed transient. The contributions of vibrational overtones seen in the Fourier transform spectrum of the transients should not vary considerably for a low pressure gas, where collisions do not play a role on the time scale considered [113]. Contrary to what is expected from the experiments with iodine in the previous chapter, these experiments show different dynamics. The results of these experiments are described and analyzed below. The experimental setup is described in paragraph 2.1.2. The experiments were performed on isotopically pure $^{81}Br_2$. Hereafter, the term bromine will refer to this isotope of bromine, unless otherwise stated.
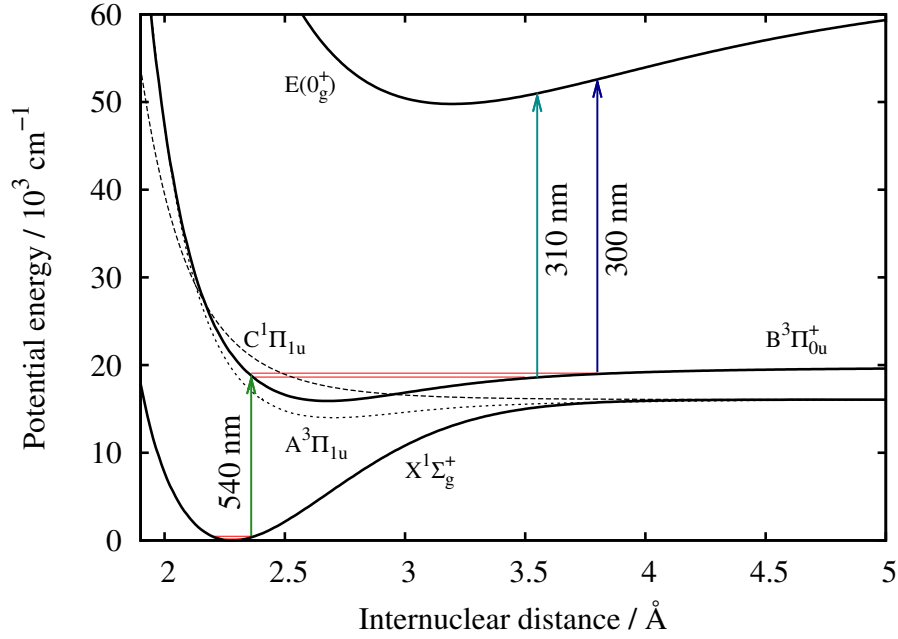
**Figure 4.1.:** Sketch of the time-resolved processes performed on molecular bromine. A pump pulse at 540 nm invokes a transition from the ground *X* state to the excited *B* state. The wave packet prepared by the initial pump pulse is interrogated by time-coincident DFWM pulses at 310 nm pulse or at 300 nm.

## 4.2. Theory and Model System

For the calculation of the signals the time-dependent Schrödinger equation for the nuclear dynamics was solved numerically. To this end a system of the three electronic states *X*, *B*, and *E* based on accurate Rydberg-Klein-Rees (RKR) potentials [114] coupled by femtosecond laser pulses was used. With the resulting state vector $|\Psi(t)\rangle$ the total polarization induced in the molecule is given by $P(t) = \langle\Psi(t)|\mu|\Psi(t)\rangle$ in which $\mu$ denotes the dipole moment of the molecule. From this total polarization the contribution in the direction of the DFWM signal was singled out in a non-perturbative manner as described in paragraph 2.2.5. This method was chosen because in these experiments the DFWM process is only used to probe the *B* state wave packet with out an internal time delay. Therefore all three DFWM pulses are coincident. In This case an perturbative description can lead to wrong results [104]. The calculated polarization field was then Fourier-transformed to calculate the frequency-resolved DFWM signal. In the present letter rotational effects are neglected since the investigation is focused on vibrational dynamics.
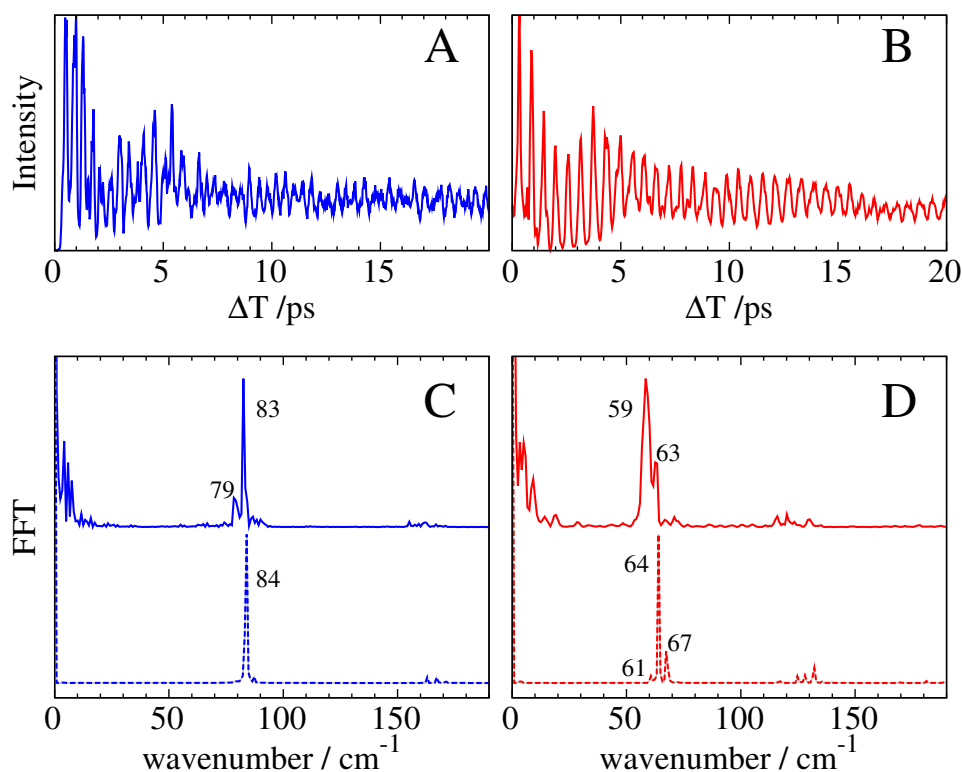
**Figure 4.2.:** Panel A shows the DFWM signal recorded as a function of the delay time, $\Delta T$ between the initial pump (540 nm) and the three time-coincident FWM (310 nm) beams for molecular bromine. Panel B shows the same for a DFWM wavelength of 300 nm. In panels C and D the FT spectrum obtained using DFWM beams with 310 nm and 300 nm, respectively, is displayed. The top solid lines show the experimental results while the lower dashed lines are the results of the simulations.

## 4.3. Results and Discussion

Bromine is a molecule lighter than iodine with a broad visible absorption spectrum. It is a highly volatile liquid at room temperature. The investigations here are performed on bromine in the gas phase. In the frequency domain, the ground *X* and excited *B* states of bromine are well characterized [34, 35]. Here, we attempt to investigate the vibrational dynamics in bromine using pump-DFWM spectroscopy. An initial pump pulse at 540 nm, which is resonant with the *X* to *B* state transition initiates the dynamics in the system. The spectrally broad femtosecond pulse creates a coherent superposition of several vibrational eigenstates in the *B* state, which is then probed by the time-coincident DFWM pulses at 300 or 310 nm. In the first case, the wavelength of the DFWM beams was chosen to be 310 nm, which is reso-

nant with the transition from the $B$ state to the $E$ state, belonging to the first tier of ion-pair states [115, 116]. Transients are recorded as a function of delay time, $\Delta T$, between the initial pump and the DFWM beams. The DFWM signal is detected using a CCD camera thereby enabling broadband detection and in this way a time and wavelength resolved spectrum is obtained. Here only the dynamics at the DFWM wavelength position (310 nm) are displayed in Fig. 4.2A. The transient consists of oscillations of the signal for positive delay times and a constant signal for negative delay times. For $\Delta T < 0$, the initial pump pulse is incident after the DFWM pulses. Since the DFWM wavelength is not resonant with any transition from the ground state, the signal observed in this case is the nonresonant signal from the ground state of bromine. For positive time delays the DFWM pulses arrive after the initial pump pulses. The oscillation of the signal reflects the motion of the wave packet in the excited state potential well. The Fourier-Transform (FT) of the transient for positive delay times is shown as solid line in Fig. 4.2C. The FT spectrum shows a sharp peak at 83 cm$^{-1}$ which agrees well with the $B$ state vibrational energy spacing around $v' = 21$ that is accessed by the initial pump at 540 nm [35]. In a next step, the DFWM probe wavelength is changed to 300 nm keeping the initial pump frequency the same. Transients are recorded as before by temporally varying the initial pump pulse relative to the DFWM beams. A change in the DFWM wavelength is not expected to drastically change the period of oscillations. However, contrary to expectations a different beat period is observed. Fig. 4.2B shows the transient at 300 nm. Beats are observed with an average separation of 510 fs. This can be compared to the average period in the transient in Fig. 4.2A, which is 395 fs, pointing to a change of wave packet oscillation frequency with a change of DFWM wavelength. The FT spectrum of the transient is displayed in Fig. 4.2D. A peak is observed at 59 cm$^{-1}$, which is quite different from the expected 83 cm$^{-1}$. This result reveals a different vibrational energy spacing, which does not match with the $B$ state vibrational frequency accessed by the 540 nm laser. In the rather similar iodine molecule no such peak shift is observed and so this result is rather surprising. Below, several possibilities are considered in order to explain the observed feature.

The pump-DFWM experiments were repeated for the other pure isotope $^{79}Br_2$ and also for the natural mixture ($^{79}Br^{81}Br$). In these samples the same behavior was seen as in the case for $^{81}Br_2$ ruling out any isotope effect. Since the pump energy is above the $A$ state dissociation limit [117], a $A \leftarrow X$ absorption would lead to disso-

ciation not to an oscillating wave packet in the *A* state, which can be probed after large delay times of several picoseconds. Therefore, the observed contributions cannot be attributed to the *A* state. Possibilities of multiphoton transitions were dismissed by checking the linearity of the signal with the pump intensity. Therefore, no contributions from higher excited states are expected. Also the possibility of a new adiabatic potential energy surface formed by the crossing of the dissociating *C* state and the *B* state (see Fig. 5.2) was investigated. However, an estimation of the resulting level spacings, which are rather invariant to different values of the unknown level coupling, led to the conclusion that such a state cannot explain the observed spacings.

Turning our attention to the quantum dynamical calculations, the distribution of populations in the different vibrational energy levels in the excited *B* state was simulated for a 540 nm initial pump pulse. From these calculations it became evident that a pump laser pulse at 540 nm deposits a substantial amount of population in the vibrational levels close to $v' = 26$ instead of an expected majority in the levels near $v' = 21$. The levels around $v' = 21$ in the excited *B* state are populated from the $v'' = 0$ level in the ground state. The vibrational levels in the region of $v' = 26$ are populated from the hot $v'' = 1$ state. The experiments on bromine were performed at room temperature. At this temperature the population in the $v'' = 1$ state is much lower than in the $v'' = 0$ state. However, the Franck–Condon factors for the $v'' = 1$ level are larger than for the $v'' = 0$ state for the transition to the *B* state by approximately a factor of 5, which results in substantial amounts of population in the higher vibrational levels of the *B* state. For the *B* state of an iodine molecule this alone would not lead to the results found in experiment. But for the *B* state of bromine, the level spacings around $v' = 26$ are rather different from those around $v' = 21$ due to the larger anharmonicity of the potential. These facts together explain the appearance of peaks around 60 cm$^{-1}$ in the FT of the transients.

Having basically two separate wave packets on the *B* state with contributions around $v' = 21$ and $v' = 26$, one would expect a double peak structure rather independent of the probe wavelength. But now, the question arises, why the 310 nm probes only the level spacings around 84 cm$^{-1}$ and 300 nm interrogates only the vibrational level spacings close to 64 cm$^{-1}$. This can be explained only by considering the Franck–Condon factors for the transitions between the states under consideration.

A more favorable overlap with the $E$ state for the vibrational levels close to $v' = 26$ for a 300 nm probe wavelength results in the observation of the 64 cm$^{-1}$ peak at this wavelength. For 310 nm the Franck–Condon factors favor transitions from the vibrational levels near $v' = 21$. Therefore, for a probe wavelength of 310 nm, an energy spacing of 84 cm$^{-1}$ is observed.

But using quantum dynamical calculations one cannot only calculate the Franck-Condon factors and populations but also the nonlinear spectra directly. A comparison of the results obtained from the experiments and from the calculations are shown in Figs. 4.2C and D. In Fig. 4.2C the FT spectrum for an initial pump wavelength of 540 nm and DFWM wavelength of 310 nm is displayed. A sharp peak is seen at 83 cm$^{-1}$. Fig. 4.2D depicts the FT spectrum for a DFWM wavelength of 300 nm with the same initial pump wavelength. The experimental spectrum shows a sharp peak at 59 and 63 cm$^{-1}$ while the calculated spectrum shows a major peak at 64 cm$^{-1}$. Comparing the experimental and theoretical spectra the general agreement with regard to the line positions is rather good. Here, it should be noted that rotational effects are not taken into account in these calculations. A better agreement with the experimental data is expected when rotations are included. Also the calculations were performed for transform-limited pulses, while in the experiments the pulse was not perfectly transform limited (approx. 120 fs pulse length instead of slightly less than 100 fs expected for a completely compressed pulse) since it was rather difficult to efficiently compress the UV pulses. This chirp may result in a change of relative intensities of the lines seen in the FT [99, 118]. Considering these aspects the agreement seen between experimental and calculated values is excellent. The calculations clearly show that a DFWM wavelength of 300 nm probes higher vibrational levels in the region of $v' = 26$.

In the above discussion, we have presented the FT plots at a particular wavelength position concerning the FT of the delay time. For a more general understanding it would be interesting to see the line positions observed at different wavelengths as displayed in Fig. 4.3. The experimental FT spectrum for a center wavelength of 310 nm is displayed in Fig. 4.3A. The $x$-axis displays the wavelengths, the $y$-axis the line positions, while the intensity is shown using a color code. Fig. 4.3D shows the theoretical spectrum for the same center wavelength. The agreement observed is remarkable. For a center wavelength of 300 nm, Figs. 4.3B and E show the experimental and theoretical spectra, respectively. Considering the neglect of
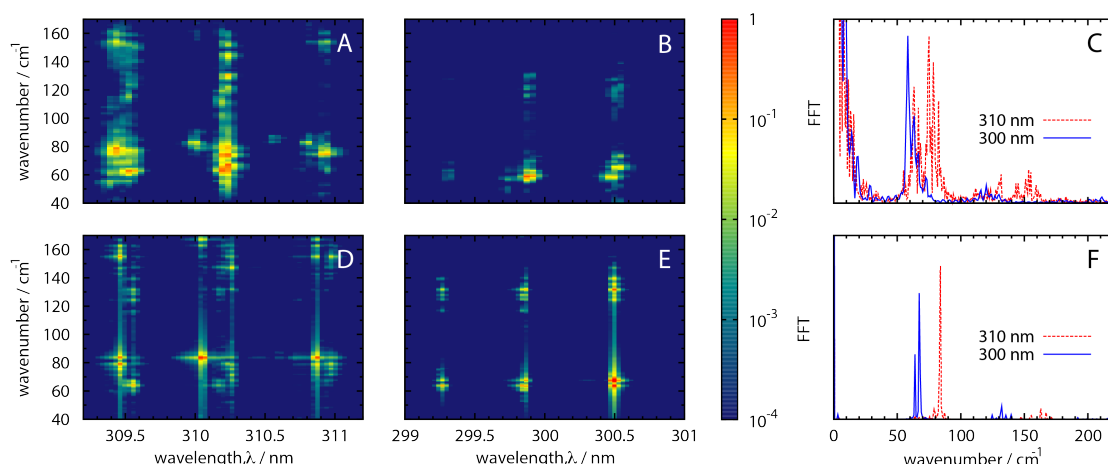
**Figure 4.3.:** Panels A and B show the experimentally obtained FT spectrum for a DFWM wavelength of 310 nm and 300 nm, respectively. Panels D and E display the respective FT spectrum obtained from calculations. The intensity of the lines are indicated by the logarithmic color code. Panels C and F show the integrated FT spectrum obtained experimentally and theoretically, respectively.

the rotations in the simulations and a possible chirp in the experiment as discussed above, the agreement observed is very good. The integrated spectra as a function of the Fourier-transformed delay time are shown in Figs. 4.3C and F for experiment and theory, respectively. This is the spectrum that is often obtained while using a photomultiplier tube as detector. Also here the experimental and theoretical values are in good agreement. Thus, the calculations support the experimental observation of different energy spacings for different DFWM (probe) wavelengths.

## 4.4. Conclusions

The vibrational dynamics of the excited *B* state in bromine were investigated using pump-DFWM spectroscopy. A different *B* state vibrational energy spacing was observed for different DFWM wavelengths of 310 nm and 300 nm with a fixed initial pump wavelength of 540 nm in both cases. For a DFWM wavelength of 310 nm, the vibrational energy spacing observed agreed well with the frequency domain data. However, for a DFWM wavelength of 300 nm, a smaller vibrational energy spacing was found. The theoretical analysis showed that the different spacings observed are attributed to the contribution of the first hot vibrational state in the electronic

ground state. The Franck–Condon factor for the transition to the *B* state is approximately five times bigger than that for the vibrational ground state, leading to a significant amount of population in the higher vibrational levels of *B* state. A favorable Franck–Condon overlap for these higher levels in the *B* state with the *E* state at a wavelength of 300 nm causes the observation of a smaller energy spacing for a DFWM (probe) wavelength of 300 nm. On the other hand 310 nm probes the lower vibrational levels and therefore gives the values "expected", which are in agreement with the frequency domain data and which also have been observed in iodine for similar experiments [110].

While in frequency-resolved spectroscopy the contribution of the hot vibrational state of Bromine was already observed, its importance for the time domain experiments, up to our knowledge, never has been taken into consideration. Furthermore it is very interesting that the contributions from the different vibrational states belonging to the electronic ground state can be probed separately varying the DFWM wavelength. This is a special feature of bromine caused by the anharmonicity of the *B* state and the Franck-Condon overlaps between the *B* and *E* states. Similar scenarios might apply to many other molecules as well. Before assigning the observed deviations from the expected dynamics to an additional excitation channel starting from a hot state, various models had been considered in detail. The results presented in this contribution demonstrate that extreme care has to be taken when interpreting data from time resolved pump-probe experiments. Even at relatively low temperatures hot vibrational modes may have a dominant contribution due to favorable Franck-Condon overlaps. Interpretations of femtosecond dynamics in practically all cases at room temperature is based on the assumption that the vibrational ground state in the electronic ground state is the starting point of every pump step. However, always when low energy vibrations like e.g. phonons in solids exist, efficient transitions also from hot states have to be taken into account. With the present method, the pump-DFWM scheme, these contributions can be resolved in the excited state dynamics individually for certain molecules, i.e. molecules with a rather anharmonic *B* state. Since an interpretation of the results using only spectroscopic properties is not easily possible, quantum dynamical calculations prove to be very powerful for a detailed understanding.

# 5. Vibrational dynamics in higher electronic excited states of Bromine

In this chapter the studies on molecular Bromine are extended to a time-resolved DFWM scheme. In the previous investigation the DFWM was only used as probe process, here a time delay in the DFWM process is introduces. This allows to gain also information about the dynamics in the ion pair states similar to the studies on iodine in chapter 3. Since the previous analysis of the bromine experiments showed that frequency and time-resolved spectra contains additional information we also analyzed these results here. Applying this technique the vibrational dynamics occurring in the $E$ ion-pair state of molecular bromine was investigated. The initial pump pulse is used to excite the $B$ state, from which the $E$ ion-pair state can be accessed in a subsequent DFWM process. By introducing an internal time delay in the DFWM process the vibrational dynamics of the $E$ and $B$ states can be probed. In most cases the signals of the $E$ and $B$ state dynamics are overlapping which makes it difficult to identify the contributions of the respective states. To this end it is shown that it is possible to extract the contributions of the $E$ state by a spectral decompostion of the DFWM signal.

## 5.1. Introduction

Here we analyze fully time- and frequency-resolved pump-degenerate four-wave mixing (pump-DFWM) experiments to monitor the ultra-fast dynamics of higher excited states in molecular bromine. Even though bromine is a diatomic molecule
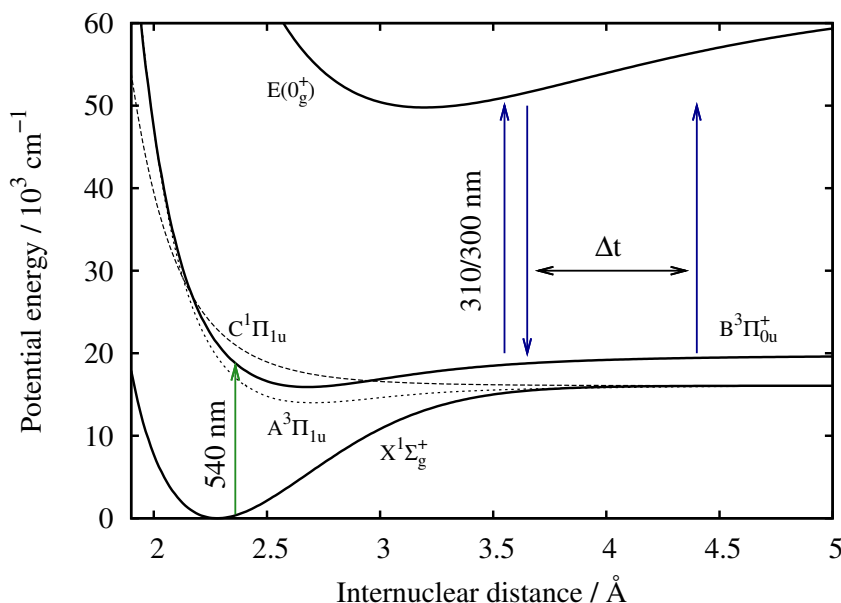
**Figure 5.1.:** Sketch of the time-resolved processes performed on molecular bromine. A pump pulse at 540 nm invokes a transition from the ground *X* state to the excited *B* state. The wave packet prepared by the initial pump pulse is then interrogated by a time-resolved DFWM process with wavelengths of 310 nm or 300 nm.

the vibrational dynamics shows complex behavior due to the strong anharmonicity of the excited state potentials which can be qualitatively different from that of iodine [63]. Extensive work has been performed to characterize the electronic states in the frequency domain [116, 119, 120]. These experiments provide very accurate data of the electronic structure of the bromine molecule, which can be used as a basis for quantum dynamical simulations of the pump-DFWM experiments. This makes the bromine molecule an ideal model system to study and test this experimental technique.

So far there are only a few experiments which investigated the vibrational dynamics in bromine. In the group of Stolow fractional revivals of a *B* state wave packet were observed [29]. The same group also measured an calculated the excited state dynamics using ion-detection based pump-probe spectroscopy [30]. Schmitt et al. employed electronically resonant CARS spectroscopy to investigate the excited state dynamics in bromine [28].

Here we investigate the vibrational dynamics occurring in the *E* ion-pair state of molecular bromine. Therefore an initial pump pulse is applied to excite the *B* state

of bromine, from which the *E* ion-pair can be accessed in a subsequent DFWM process which is resonant with the *E* to *B* transition. By introducing an internal time delay in the DFWM process the vibrational dynamics of the *E* and *B* state can be observed time- and frequency-resolved. This pump-DFWM scheme is depicted in Fig 5.1. Simulations of the pump-DFWM process are used to verify the assignment of the measured dynamics to the *E* ion-pair state.

## 5.2. Theory

The model system applied to simulate the DFWM signal for the bromine molecule is composed of the vibrational Hamiltonians belonging to three electronic states

$$\hat{H}_{\text{mol}} = |X\rangle H_X \langle X| + |B\rangle H_B \langle B| + |E\rangle H_E \langle E| \ . \tag{5.1}$$

Here, $H_X$,$H_B$ and $H_E$ denote the vibrational Hamiltonians of the ground *X* , the first excited *B* and the *E* ion pair-state. To model these Hamiltonians Born-Oppenheimer potential energy surfaces consisting Rydberg-Rees-Klein (RKR) potentials calculated from Dunham coefficients given in Refs. [116, 119, 120] are used. Furthermore the coupling of the molecule to the electric field of the laser pulses $\mathbf{E}(t)$ through the dipole operator $\hat{\mu}$ is treated in the dipole approximation

$$\hat{H}(t) = \hat{H}_{\text{mol}} - \hat{\mu}\mathbf{E}(t) \tag{5.2}$$

using the dipole operator

$$\hat{\mu} = \mu \left( |\Psi_X\rangle \langle \Psi_B| + |\Psi_B\rangle \langle \Psi_E| \right) + c.c. \tag{5.3}$$

with a constant dipole strength $\mu$. The electric fields of the laser pulses are assumed to have the form

$$\mathbf{E}(t) = \sum_n \mathbf{E}_n(t) = \sum_n \varepsilon(t - T_n)e^{-i\omega_n(t-T_i)+i\mathbf{k}_n\mathbf{x}} \tag{5.4}$$

with Gaussian shaped envelopes $\epsilon(t)$ centered at times $T_n$ with frequencies $\omega_n$ and wave vectors $\mathbf{k}_n$. The polarization field was calculated in the same way as described

for the iodine experiment in chapter 3. In the simulations the polarization was calculated over a time range of 10 ps and then Fourier transformed to get the spectra which correspond to the spectra measured in the experiment using a CCD camera. This results in transients at every detection wavelength. The different terms in Eq. 3.12 are corresponding to different spectroscopic pathways exhibiting dynamics of the $B$ and the $E$ state as detailed in section 3.3. The third term in Eq. 3.12 comprehends only the dynamics of the $E$ state, therefore this part of the polarization can be used to determine the contribution on the $E$ state dynamics included in the complete transient as measured in the experiments.

## 5.3. Results and Discussion

The ground $X$ and excited $B$ states of bromine have been well characterized in frequency domain experiments [119, 120]. Also the ion pair states have been investigated in detail [116]. Since these states are well characterized in these frequency domain experiments it is possible to connect the measured vibrational dynamics in the present experiments with the properties of the molecule. As mentioned above, an initial pump pulse at 540 nm, which is resonant with the $X$ to $B$ state transition, is used to initiate the dynamics in the system. This spectrally broad femtosecond pulse creates a coherent superposition of several vibrational eigenstates in the $B$ state, which is then probed by the time-resolved DFWM process.

Since the $B$ state potential energy surface is highly anharmonic, the pump process creates a wave packet on the $B$ state which strongly depends on the population of hot vibrational states in the ground $X$ state. This was investigated in the previous chapter in detail using a pump-DFWM scheme with time-coincident pulses [63]. Here we extend these experiments to a time-resolved DFWM scheme to investigate also the $E$ state dynamics. By using two different sets of DFWM wavelengths different vibrational modes of the $E$ state can be accessed. This should be reflected in different contributions of the $E$ state in the recorded transients.

Figure 5.2 shows the transient for a DFWM wavelength of 310 nm. The transient shows a complex superposition of oscillations of different frequencies which can be determined by performing a Fourier transformation of the transient signal. The
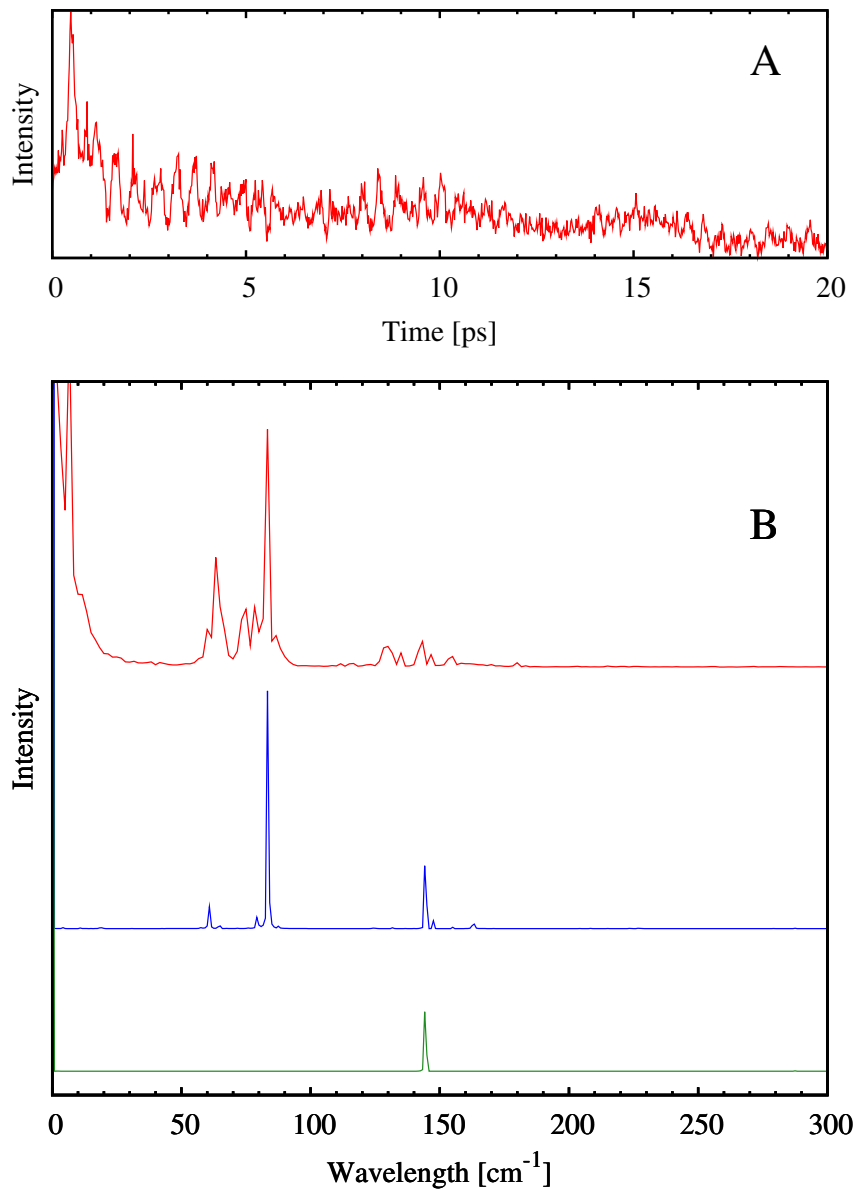
**Figure 5.2.:** Panel A shows the DFWM signal recorded as a function of the delay time, $\Delta t$, within the DFWM beams of 310 nm for molecular bromine. Panel B shows the FT of the experimental and calculated transients. The red line denotes the FT of the experimental signal while the blue line shows the FT of the calculated transient. The FT of the simulation including only the excited state dynamics is shown as green line.
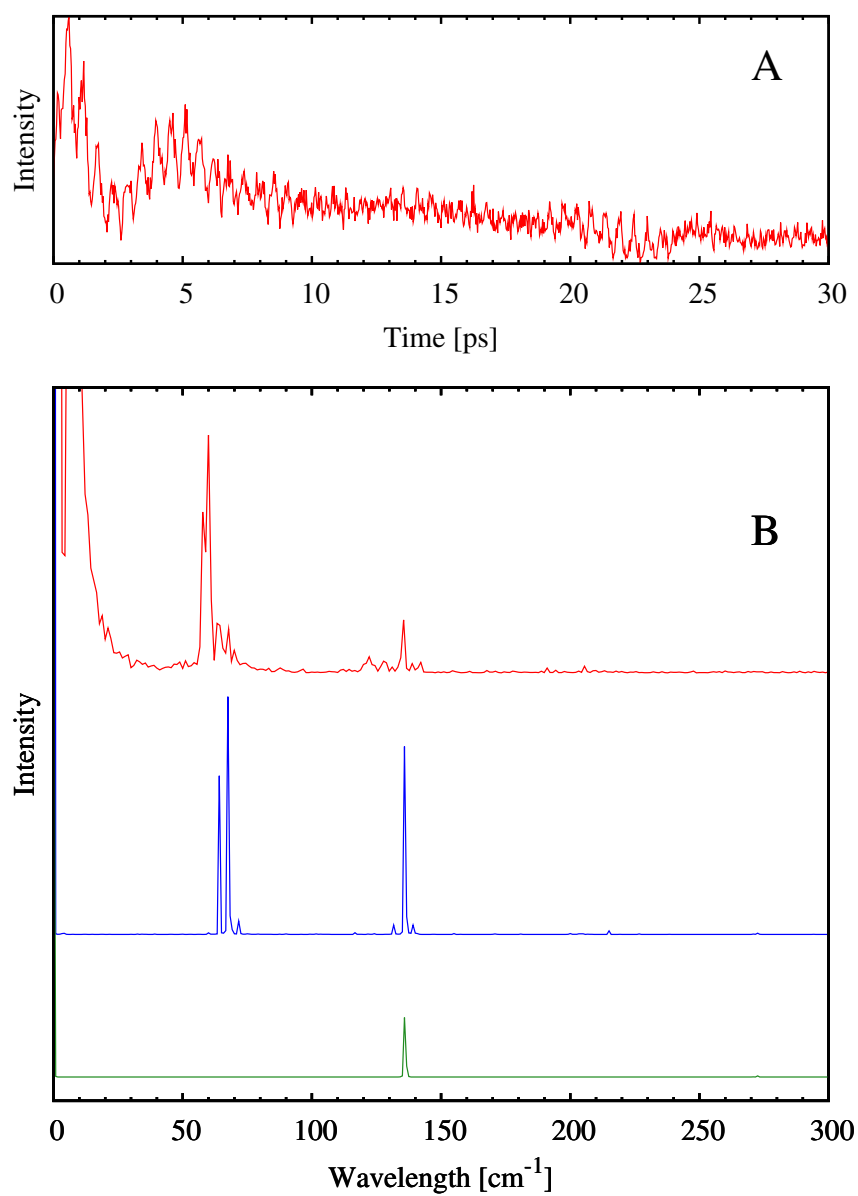
**Figure 5.3.:** Same as Fig. 5.2 but for a DFWM wavelength of 300 nm.

result is shown in panel B of Fig. 5.2. This FT shows a broad double peak structure between 50 cm⁻1 and 100 cm⁻1. The peak around 84 cm⁻1 corresponds to the level spacing of vibrational levels around $v' = 21$ of the $B$ state, which is the expected excitation region corresponding to the 540 nm pump pulse. The peak around 60 cm⁻1 arises from a wave packet created by a transition from the first vibrational state $v'' = 1$ of the ground state, which leads to an excitation to $v' = 26$ where the level spacing is around 60 cm⁻1. This can also be seen in the FT of the simulated transient. An additional peak structure is noticeable at wavenumbers above 120 cm⁻1. These peaks could be attributed to either the second harmonics of the $B$ state dynamics or to dynamics on the $E$ state. Since they overlap it is difficult to identify the contribution of the $E$ state from the experimental signal. But with the help of the simulations where it is possible to include only those pathways which contain the $E$ state dynamics it is possible to assign the peak at 143.3 cm⁻1 to the $E$ state dynamics. This separate contribution is also shown in Fig. 5.2

In a next step the DFWM wavelength was changed to 300 nm. The transient is shown in Fig. 5.3 along with its FT in panel B. For this case the strongest vibrational peaks are at 60 cm⁻1. Due to particular Franck-Condon overlaps between the $B$ and the $E$ states only that part of the $B$ state wave packet created from the hot vibration ground state is probed by the 300 nm DFWM process. Comparing simulations and experiment the $E$ state dynamics can be assigned to the peak at 135.7 cm⁻1. This is at a lower wavenumber than the peak for the 310 nm DFWM experiment. This can easily be rationalized because the 300 nm pulses excite higher vibrational levels in the $E$ state which have a lower level spacing.

The transients shown in Figs. 5.2 and 5.3 are the integrated transients over the complete detection wavelength range and are basically the same as for an experiment using a photomultiplier as detector. In order to examine the experimental DFWM signal in more detail it was recorded frequency-resolved using a CCD camera as detector. The FTs of the transients at different detection wavelengths are shown as color maps in Figs. 5.4 and 5.5. The experimental FT spectrum for a center wavelength of 310 nm is displayed in Fig. 5.4A. The $x$-axis displays the wavelengths, the $y$-axis the line positions while the intensity is shown using a color code. Fig. 5.4B shows the theoretical spectrum for the same center wavelength. For a center wavelength of 300 nm, Figs. 5.5A and B show the experimental and theoretical spectra, respectively. It is obvious that for the two DFWM wavelengths
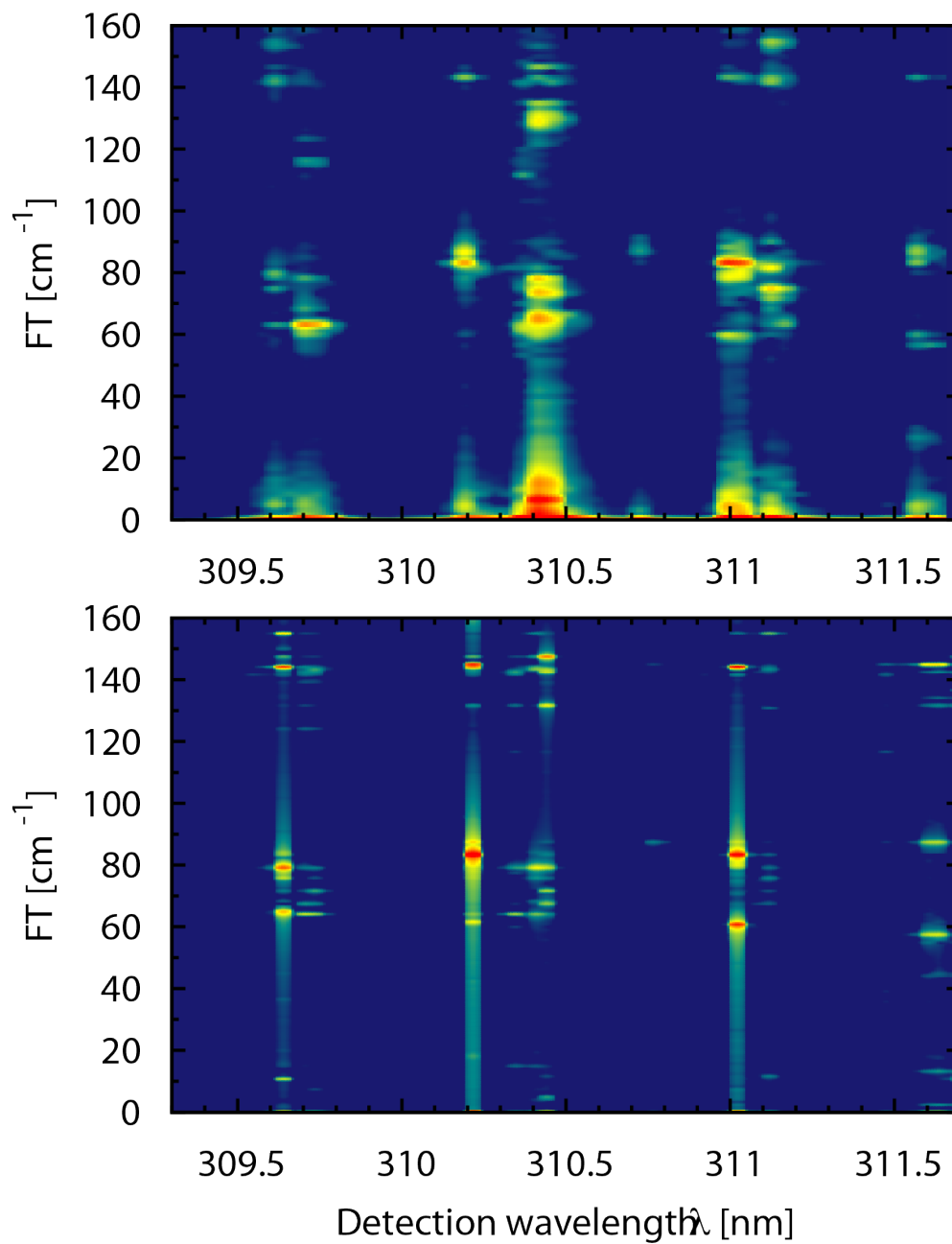
**Figure 5.4.:** Panel A shows the experimentally obtained FT spectrum for a DFWM wavelength of 310 nm. Panels B displays the respective FT spectrum obtained from calculations. The intensity of the lines are indicated by the logarithmic color code.
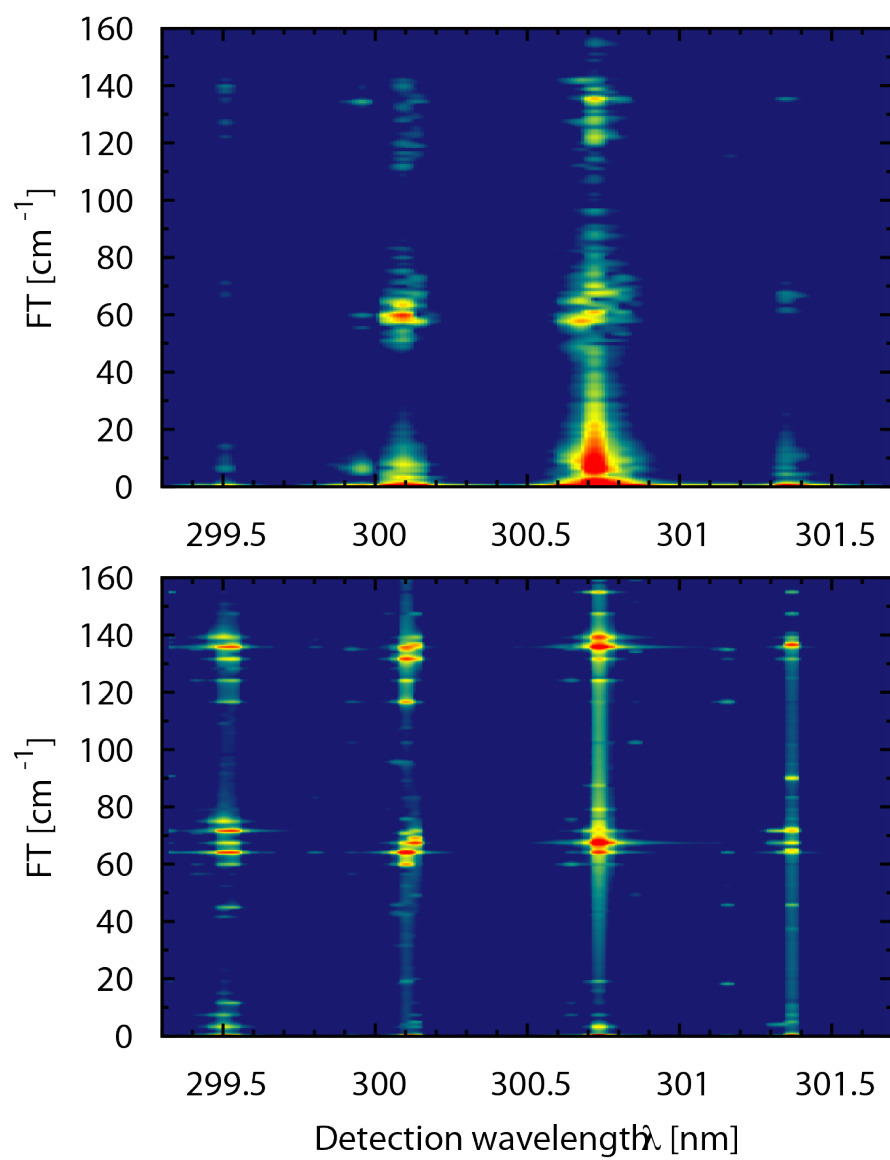
**Figure 5.5.:** Same as fig. 5.4 but for a DFWM wavelength of 300 nm.

the FTs at specific detection wavelength differ considerable. The intensity of the contributions from the *B* state and the *E* state vary strongly at different detection wavelengths. Therefore it is possible to find certain positions where the *E* state contribution is much more distinct than in the integrated DFWM transients (Figs. 5.2 and 5.3). This fact allows for a more detailed investigation of the *E* state dynamics since it can be extracted from the overall transient behaviour. The experimentally recorded data and the simulations show the same structure of vertical lines and different peak positions, although the employed model for the calculations is reduced to contain only the vibrational degrees of freedom neglecting the rotations. It can be reasoned that such a model system is adequate to simulate the basic features of these complex spectra.

In order to track the dynamics of the *E* ion-pair state exclusively the relevant data can be extracted from the frequency-resolved FT maps by choosing particular line positions. These line positions where chosen by comparing the experimental map plots (Figs. 5.4 and 5.5) with the simulations which were reduced to contain only the excited state dynamics. Figures 5.6 and 5.7 show the FTs taken at particular line positions, which shows a stronger *E* state contribution than the transient of the integrated transient. For the case of the 310 nm excitation the FT of a selected transient is shown in Fig. 5.6 together with the simulated FT at the same line position. The peak is not much stronger than in Fig. 5.2 but it only shows the 143.3 cm peak which corresponds to the *E* state dynamics, the second harmonics of the *B* state dynamics are absent. The FT for a DFWM of 300 nm is shown in Fig. 5.7. Here it was possible to find positions where the *E* state dynamics dominate the transient and thus shows the strongest peak in the FT.

For the 310 nm DFWM experiment the *E* state peak is located at 143.3 cm$^{-}$1. Comparing this value to the frequency-domain data indicates that it corresponds to the excitation of vibrational levels in vicinity of $v' = 7$. The minimum of the *E* state PES lies at an energy of 49778 cm$^{-}$1 and the $v' = 7$ level at 50896 cm$^{-}$1. This energy is comparable to the total energy of the 540 nm initial pump pulse and the 310 nm DFWM pulses which is 50777 cm$^{-}$1 . For a DFWM wavelength of 300 nm, the *E* state peak appears at 135.7 cm$^{-}$1 which correspond to the level spacing found at around $v' = 16$. The energy position of this level is at 52130 cm$^{-}$1 and the energy of the 540 nm and 300 nm pulse combination is 51852 cm$^{-}$1 . So the observed dynamics can clearly be assigned to the *E* ion pair state. For the case of bromine these

values were known from frequency-domain experiments but it shows the sensitivity of the method to obtain information about high-lying excited states of the probed molecule.
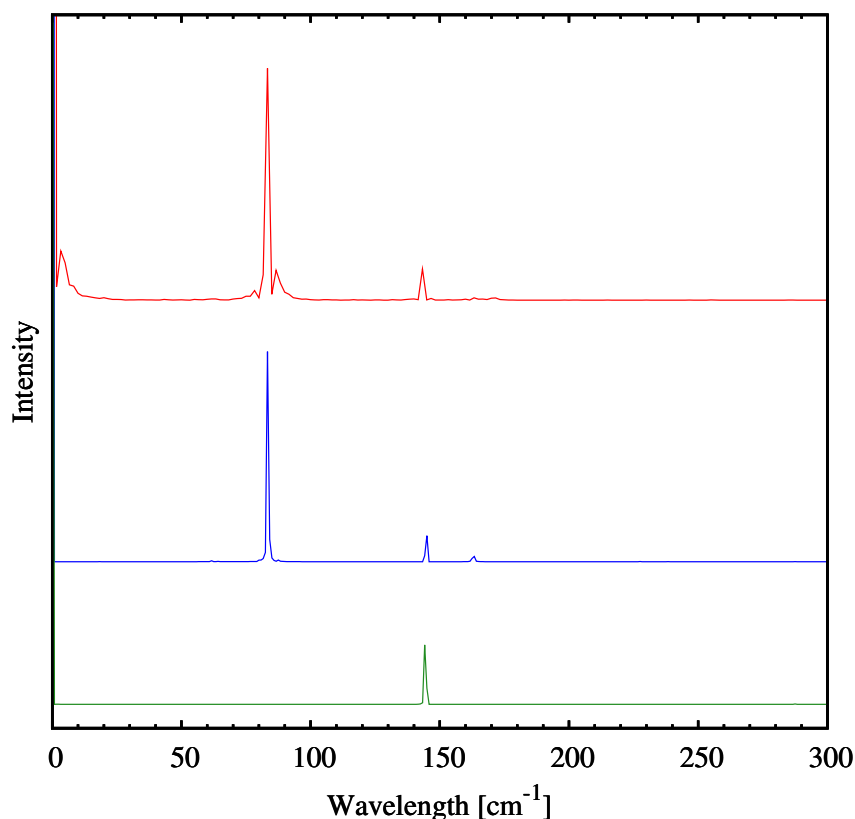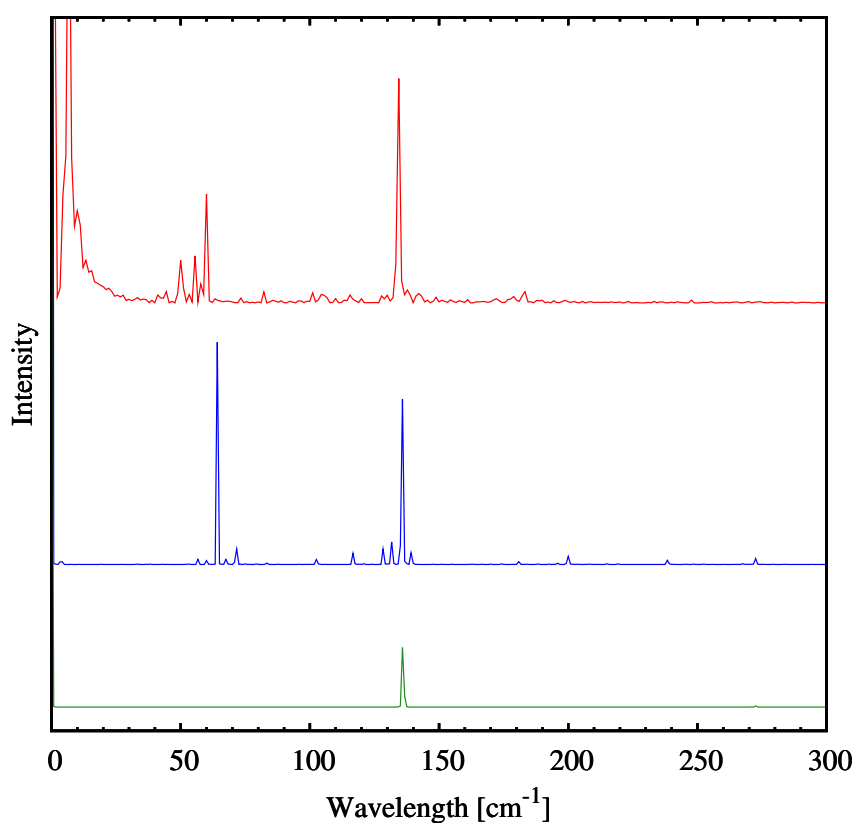


**Figure 5.6.:** Here a selected FT of the 310 nm DFWM experiment at a detection wave length of 310.148 nm is shown (experiment in red, simulation in blue). For comparison also the FT of the simulation including only excited state dynamics is shown as green line.

## 5.4. Conclusion

It could be shown that the pump DFWM technique is a well suited tool to gain information about the wave packet dynamics occurring in higher lying electronic states of molecules. Here we used molecular bromine as a test system. Although this is a simple two atomic molecule, it exhibits complex wave packet dynamics due to its highly anharmonic excited state potentials. Using a DFWM setup with a

frequency-resolved signal detection it was possible to examine the ion-pair state dynamics in detail by considering only transients at particular detection wavelengths. It was possible to verify the experimental findings by quantum dynamical simulation reproducing all the basic features of the measured transients. Two different wave packets could be measured by using two different DFWM wavelengths. Furthermore, the observed dynamics of these wave packets are in good agreement with simulations based on a model system using PES calculated from frequency domain experiment data. These simulations are important to understand the complex dynamics measured in the experiments, especially to asign specific features of the transients to properties of the molecular systems.



**Figure 5.7.:** Here a selected FT of the 300 nm DFWM experiment at a detection wave length of 299.914 nm is shown (experiment in red, simulation in blue). For comparison also the FT of the simulation including only excited state dynamics is shown as green line.

# 6. Non-resonant multi photon transition

Non-resonant multiphoton transitions between three electronic states of a molecular system are studied. Based on a projection operator formalism which is formulated in the framework of the so-called time-local as well as the time-nonlocal approach, time-dependent Schrödinger equations are obtained which include effective couplings to the laser field. For both procedures a slowly varying amplitude approximation can be invoked. The resulting time-local equations can be computed numerically in a much more efficient way than the original effective Schrödinger equations. The validity of these approximations is verified numerically for a 2-photon process. Furthermore, the effective Schrödinger equations are specified to sequences of 2-photon and 3-photon transitions. The derived equations are applied to a molecular system consisting of three electronic states with Morse-type potential energy curves. Using different laser pulse scenarios the conditions are discussed under which a sequence of 2-photon and 3-photon transitions can take place. The work presented here was developed in cooperation with Dr. habil. Volkhard May and published in Ref. [65].

## 6.1. Introduction

In many cases multiphoton transitions may proceed without resonant intermediate states. These so–called *non-resonant multiphoton transitions* (NMTs) represent processes in which transitions between, for example, electronic energy levels of a molecular system can only take place if the energy of two or more photons induces a transition that does not involve intermediate states which support it. Therefore,

whenever the external frequency is below half of the fundamental optical transition, NMTs can come into effect. Because the non-existence of intermediate states the couplings to higher lying off–resonant states play an important role for NMTs.

Theoretically NMT processes can be treated either in the frequency or in the time domain. The treatment in the frequency domain is well established [45, 121–124] while less studies have been performed in the time domain to explain, for example, femtosecond spectroscopical experiments [46, 47, 125, 126]. The purpose of this paper is to extend preliminary considerations by one of the authors [44, 127, 128] to sequences of ultrafast NMTs in a three–electronic level molecule.

NMT process in the time domain can be simulated directly by solving the time-dependent Schrödinger equation. In such studies a state expansion should of course be avoided since otherwise one would have to treat also the high lying off–resonant states which induce the electronic coupling. So, for example, grid-based calculations would be possible but have to be performed with a sufficiently high precision and then any type of light–induced transitions including NMTs can be accounted for. This approach to study NMTs has been shown to work in different cases either using the Born-Oppenheimer approximation [129, 130] or avoiding it [131, 132]. But the systems which could be treated in this manner were small systems as atoms, diatomic molecules or 1d model systems.

In order to be able to treat larger systems one has to invoke perturbation theory or approximations in one way or the other. The perturbation theory is normally applied in the laser-matter interaction term $-\hat{\mu}\mathbf{E}(t)$ with the molecular dipole operator $\hat{\mu}$ and the field–strength of the laser pulse $\mathbf{E}(t)$ [45, 121–124]. As a reminder and to show the importance of the non-resonant states we calculate in Appendix A the transition probability of a non–resonant two–photon process in using second–order perturbation theory. The used perturbational treatment of the coupling to the radiation field, however, restricts the whole description to the low–field regime. Furthermore, the perturbative treatment includes multiple time integrals which are computationally challenging.

An alternative approach is the development of an effective Schrödinger equation where NMT processes are accounted for by effective couplings [44, 45, 127, 128]. In this formalism the electronic states are split into two categories. Those states representing the initial and final states within the NMT process will then be named

*primary* states. The rest of the states with energy levels far above the initial and final states of the NMT process are described in a way independent of the solution of the time–dependent Schrödinger equation and called non–resonant *secondary* states. These *secondary* states are not treated explicitly, i.e. there will be no Schrödinger equations for these states, but they enter the theory only via effective NMT coupling matrix elements **D**. The general approach of deriving effective coupling expressions to the radiation field is known (see, for example, [44, 45, 47]) and is based on projection operator techniques as detailed below.

It is common to use effective coupling expressions to the radiation field [133, 134] and it is also known how to derive such couplings [44, 45, 47]. But, so far, such approaches have never been directly applied to femtosecond spectroscopy. Previously it has been shown [127, 128] how NMT processes can be incorporated into a theory which only accounts for a very selected set of states (previously introduced here as the primary states). This way one can derive an *effective* time-dependent Schrödinger equation with *effective* couplings to the radiation field including powers of the field-strength and effective transition dipole operators. Here we will extend this theory to include sequences of two and three-photon NMT processes.

It is the particular aim of this paper to apply two different variants of the projection operator formalism which are called the time-nonlocal (TNL) and the time-local (TL) approaches. These variants are well-known from the field of dissipative quantum dynamics (for references in this field, see for example [48, 49]). The TNL theory is based on the Nakajima-Zwanzig identity [135, 136] and is also called chronological time ordering prescription [137], time convolution approach [138] or Mori formalism [139]. Historically the TL approach goes back to work by Fuliński and Kramarczyk [140, 141] and Shibata et al. [142, 143] and is also known as partial time ordering prescription [137], time-convolutionless formalism[138], and Tokuyama-Mori approach [144]. Both, the TL and the TNL formalism use the exact contributions up to second order in the small parameter but do different partial resummations of higher-order terms. To have a clear comparison of both approaches we will remind on some formulas already given in [127, 128].

The paper is organized as follows: In the next section the model system is introduced before in Section III we derive the effective Schrödinger equations both in the TNL and in the TL fashion. The weak field assumption is used in Section IV while

in Section V the rotating wave (RWA) and the slowly varying amplitude (SVA) approximation are employed. Numerical results are given in Section VI and the paper ends with some conclusions in Section VII.

## 6.2. The Model and Some Basic Relations

The total Hamiltonian governing NMT processes in a molecular system can be split into the molecular part $H_{\text{mol}}$ and the laser field part $H_{\text{field}}(t)$

$$H(t) = H_{\text{mol}} + H_{\text{field}}(t) .\tag{6.1}$$

Using the adiabatic electronic states $|\varphi_\alpha\rangle$ the molecular part has the form

$$H_{\text{mol}} = \sum_\alpha H_\alpha(q) |\varphi_\alpha\rangle \langle\varphi_\alpha| .\tag{6.2}$$

Here the $H_\alpha(q)$ are vibrational Hamiltonians with $q$ representing the set of vibrational coordinates. To remain at a sufficient simple form of $H_{\text{mol}}$ nonadiabatic couplings between the states are neglected throughout the whole paper (see also the remark below).

The eigenfunctions of the vibrational Hamiltonian are denoted as $\phi_M^\alpha(q)$, and the electronic-vibrational states $|\Psi_{\alpha M}\rangle = |\phi_M^\alpha\rangle|\varphi_\alpha\rangle$ form a complete basis with energies $\varepsilon_{\alpha M} = \varepsilon_\alpha + \omega_{\alpha M}$. Here, the $\varepsilon_\alpha$ describe the electronic energies, i.e. the minimum of the PES plus vibrational zero–point energy, and the $\omega_{\alpha M}$ are the vibrational eigenenergies.

As mentioned in the introduction, the whole state space will be split into the part of primary states and off–resonant secondary states. Therefore the set of electronic quantum numbers $\alpha$ is separated into the set $x$ belonging to the state space of secondary states and a remaining set $a$ related to the primary state space (cf. Fig. 6.1). In the following the latter comprises the electronic ground–state with $a = g$, the first excited state with $a = e$ and one higher excited state with $a = f$. In general, of course further states as well as nonadiabatic couplings can be included if necessary (the latter introduce additional deactivation channels among the excited
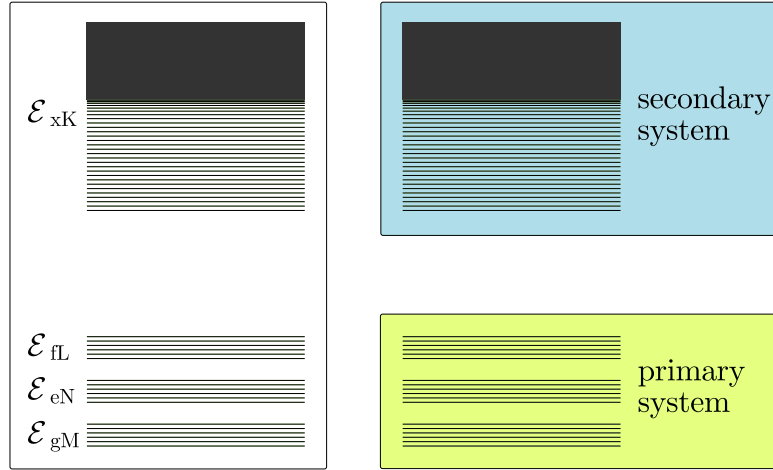
**Figure 6.1.:** Energy level scheme considered in the framework of NMT processes. Left panel: Vibrational levels $\varepsilon_{gM}$, $\varepsilon_{eN}$ and $\varepsilon_{fK}$ referring to the ground and two excited electronic states, all connected by NMTs. The set of energy levels $\varepsilon_{xK}$ form the manifold of off–resonant levels. Right panel: Separation of the complete level scheme into the primary and into the secondary system of levels being off–resonant with respect to the non–resonant multiphoton transitions.

states in the primary state space). To ease the description of the secondary states we introduce their density of states (DOS)

$$\varrho(\Omega) = \sum_{x,K}{}' \delta(\Omega - \varepsilon_{xK}), \tag{6.3}$$

which, if necessary, can be reduced to a pure electronic one. Nonadiabatic couplings may enter by replacing the $\varepsilon_{xK}$ by the true energy eigenvalues following from a diagonalization of the secondary states Hamiltonian. (The rough way the DOS finally enters the effective time–dependent Schrödinger equations including NMT processes let become the effect of nonadiabatic couplings of less importance here.)

The coupling $H_{\text{field}}(t)$ to the laser field in Eq. 6.1 is treated in dipole approximation and given by

$$H_{\text{field}}(t) = -\mathbf{E}(t)\hat{\boldsymbol{\mu}} \equiv -\mathbf{E}(t)\sum_{\alpha \neq \beta} \mathbf{d}_{\alpha\beta}\,|\varphi_{\alpha}\rangle\,\langle\varphi_{\beta}| + \text{h.c.}, \tag{6.4}$$

where $\hat{\boldsymbol{\mu}}$ is the molecular dipole operator and $\mathbf{E}(t)$ the electric field strength. It will

be written as

$$\mathbf{E}(t) = \mathbf{n}E(t)e^{-i\omega t} + \text{c.c.} \,, \tag{6.5}$$

with the unit vector $\mathbf{n}$ of (linear) polarization, the field envelope $E(t)$ and carrier frequency $\omega$.

The time-dependent Schrödinger equation defined be the complete Hamiltonian, Eq. 6.1 reads

$$i\hbar\frac{\partial}{\partial t}|\Psi(t)\rangle = H(t)|\Psi(t)\rangle \,. \tag{6.6}$$

For further use in the subsequent derivations we note its formal solution

$$|\Psi(t)\rangle = U_{\text{mol}}(t - t_0)S(t, t_0; \mathbf{E})|\Psi(t_0)\rangle \tag{6.7}$$

is written here in using the standard separation of the complete time-evolution operator $U(t, t_0; \mathbf{E})$ into the molecular part

$$U_{\text{mol}}(t - t_0) = \exp\left(-\frac{i}{\hbar}H_{\text{mol}}(t - t_0)\right), \tag{6.8}$$

and into the $S$-operator of the coupling to the radiation field:

$$S(t, t_0; \mathbf{E}) = \hat{T}\exp{-\frac{i}{\hbar}\int_{t_0}^{t} d\tau \, U_{\text{mol}}^{+}(\tau - t_0)H_{\text{field}}(\tau)U_{\text{mol}}(\tau - t_0)} \,. \tag{6.9}$$

## 6.3. Effective Schrödinger Equation for NMT Processes

In what follows we describe a systematic way to derive an effective NMT–Hamiltonian. It will define an effective Schrödinger equation exclusively defined in the space of the primary states. We start in presenting the derivation of the TNL–version (see also [127, 128]). Afterwards, it is confronted with TL–version of an effective NMT Schrödinger equation not given in literature so far.

The approaches use standard projection operator techniques and are based on the projector into the space of primary states

$$\hat{P} = \sum_a |\varphi_a\rangle \langle \varphi_a| , \tag{6.10}$$

Its orthogonal complement is denoted by

$$1 - \hat{P} \equiv \hat{Q} = \sum_x |\varphi_x\rangle \langle \varphi_x| . \tag{6.11}$$

According to the introduction of $\hat{P}$ and $\hat{Q}$ we obtain primary and secondary states as

$$|\Psi_1(t)\rangle = \hat{P} |\Psi(t)\rangle , \tag{6.12}$$

and as

$$|\Psi_2(t)\rangle = \hat{Q} |\Psi(t)\rangle , \tag{6.13}$$

respectively, where $\Psi(t)$ is an arbitrary state defined in the complete Hilbert space. In the same way we may introduce reduced Hamiltonians

$$H_1(t) = H_1^{(\text{mol})} + H_{\text{field}}^{(1)}(t) = \hat{P} H(t) \hat{P} , \tag{6.14}$$

and

$$H_2(t) = H_2^{(\text{mol})} + H_{\text{field}}^{(2)}(t) = \hat{Q} H(t) \hat{Q} , \tag{6.15}$$

with the first exclusively defined in the primary state space and the latter in the Hilbert space of secondary states.

Since it is the aim of the following derivation to get an effective time-dependent Schrödinger equation which is valid only in the primary state space we introduce a separation of the original time–dependent Schrödinger equation 6.6. The part projected onto primary states reads

$$i\hbar \frac{\partial}{\partial t} |\Psi_1(t)\rangle = H_1(t) |\Psi_1(t)\rangle + \hat{P} H_{\text{field}}(t) \hat{Q} |\Psi_2(t)\rangle , \tag{6.16}$$

and that projected onto off–resonant secondary states follows as

$$i\hbar \frac{\partial}{\partial t} |\Psi_2(t)\rangle = \hat{Q} H_{\text{field}}(t) \hat{P} |\Psi_1(t)\rangle + H_2(t) |\Psi_2(t)\rangle .$$
(6.17)

Here we took into account that $\hat{P} H_{\text{mol}} \hat{Q} = \hat{Q} H_{\text{mol}} \hat{P} = 0$.

### 6.3.1. Time-nonlocal version

The TNL–version of an effective NMT Schrödinger equation is obtained by a direct solution of Eq. 6.17 (note the initial condition $|\Psi_2(t_0)\rangle = 0$):

$$|\Psi_2(t)\rangle = -\frac{i}{\hbar} \int_{t_0}^{t} d\bar{t} \; U_2(t, \bar{t}; \mathbf{E}) \hat{Q} H_{\text{field}}(\bar{t}) \hat{P} |\Psi_1(\bar{t})\rangle .$$
(6.18)

The newly appearing time–evolution operator $U_2(t, \bar{t}; \mathbf{E})$ is that defined by $H_2(t)$. In the following it will be separated into $U_2^{(\text{mol})}(t - \bar{t})$ defined in analogy to Eq. 6.8 but with $H_2^{(\text{mol})}$ instead of $H_{\text{mol}}$ and into $S_2(t, \bar{t}; \mathbf{E})$. This $S$–operator is defined similar to Eq. 6.9 but with $U_{\text{mol}}$ and $H_{\text{field}}$ replaced by $U_2^{(\text{mol})}$ and $H_{\text{field}}^{(2)}(t)$, respectively.

If we insert the expression for $|\Psi_2(t)\rangle$, Eq. 6.17 into Eq. 6.16 for $|\Psi_1(t)\rangle$ we obtain a closed equation for the latter state

$$i\hbar \frac{\partial}{\partial t} |\Psi_1(t)\rangle = H_1(t) |\Psi_1(t)\rangle + \int_{t_0}^{t} d\bar{t} \; K_{\text{field}}(t, \bar{t}) |\Psi_1(\bar{t})\rangle .$$
(6.19)

The time–integral kernel takes the form

$$K_{\text{field}}(t, \bar{t}) = -\frac{i}{\hbar} \hat{P} H_{\text{field}}(t) \hat{Q} U_2^{(\text{mol})}(t - \bar{t}) S_2(t, \bar{t}; \mathbf{E}) \hat{Q} H_{\text{field}}(\bar{t}) \hat{P} .$$
(6.20)

It accounts for all NMT processes realized by the coupling to the manifold of off–resonant states. Since the latter have been projected out, of course, the resulting equation of motion is time non–local and shows a certain memory effect.

Let us expand Eq. 6.19 with respect to the primary electronic states. As a result a

set of coupled equations of motions for the vibrational wave functions $\chi_a(q, t) = \langle \varphi_a | \Psi_1(t) \rangle$ follow:

$$i\hbar \frac{\partial}{\partial t} \chi_a(t) = H_a(t) \chi_a(t) - \mathbf{E}(t) \sum_b \mathbf{d}_{ab} \chi_b(t) + \sum_b \int_{t_0}^{t} d\bar{t} \, K_{ab}(t, \bar{t}) \chi_b(\bar{t}) \,. \quad (6.21)$$

Note the introduction of

$$K_{ab}(t, \bar{t}) = \langle \varphi_a | K_{\text{field}}(t, \bar{t}) | \varphi_b \rangle \,. \quad (6.22)$$

## 6.3.2. Time-local version

In analogy to the time-convolutionless projection operator formalism proposed by Shibata and coworkers [143, 145] we derive the TL–version of an effective NMT Schrödinger equation. For this one replaces $|\Psi_1(\bar{t})\rangle$ in Eq. (6.18) by

$$|\Psi_1(\bar{t})\rangle \equiv \hat{P} |\Psi(\bar{t})\rangle = \hat{P} U(\bar{t}, t)(\hat{P} + \hat{Q}) |\Psi(t)\rangle \,. \quad (6.23)$$

Introducing the operator

$$\hat{\Sigma}(t) = -\frac{i}{\hbar} \int_{t_0}^{t} d\bar{t} \, U_2(t, \bar{t}; \mathbf{E}) \hat{Q} H_{\text{field}}(\bar{t}) \hat{P} U(\bar{t}, t; \mathbf{E}) \,, \quad (6.24)$$

Eq. (6.18) is written as

$$|\Psi_2(t)\rangle = \hat{\Sigma}(t) \hat{P} |\Psi_1(t)\rangle + \hat{\Sigma}(t) \hat{Q} |\Psi_2(t)\rangle \,. \quad (6.25)$$

From this relation one can deduce that

$$|\Psi_2(t)\rangle = (1 - \hat{\Sigma}(t))^{-1} \hat{\Sigma}(t) \hat{P} |\Psi_1(t)\rangle \,, \quad (6.26)$$

and Eq. (6.16) takes the form

$$i\hbar \frac{\partial}{\partial t} |\Psi_1(t)\rangle = H_1(t) |\Psi_1(t)\rangle + \hat{P} H_{\text{field}}(t) \hat{Q} (1 - \hat{\Sigma}(t))^{-1} \hat{\Sigma}(t) \hat{P} |\Psi_1(t)\rangle \,. \quad (6.27)$$

In contrast to Eq. 6.19 this equation is local in time. As for the TNL version it can also be expanded by the primary electronic states.

## 6.4. Weak Field NMT Processes

Since Eqs. 6.19 and 6.27 have been derived without any approximation its exact solutions $\Psi_1(t)$ should be identical with $\Psi(t)$ of Eq. 6.7 projected into the space of primary states. If a particular approximation for $K_{\text{field}}$ or the operator $[1 - \hat{\Sigma}(t)]^{-1}$ is taken, however, the quality of the result can be hardly judged. Such a problem arises since, for example, the kernel $K_{\text{field}}$, Eq. 6.20, already includes a complete summation with respect to **E**. It is covered via $S_2$ which has to be approximated when carrying out concrete computations. Once such an approximation $K_{\text{field}}^{(\text{approx})}$ has been introduced it remains rather undefined if the determination of $\Psi_1$ by a direct solution of Eq. 6.19 describes the main features of the dynamics. At least this has to be checked separately.

### 6.4.1. Time-nonlocal version

Nevertheless, we will proceed in this manner in the following and set

$$K_{\text{field}}(t, \bar{t}) = K_{\text{field}}^{(2)}(t, \bar{t}) + K_{\text{field}}^{(3)}(t, \bar{t}) + \dots , \tag{6.28}$$

where, $K_{\text{field}}^{(2)}$ and $K_{\text{field}}^{(3)}$ are of second and third power in the field–strength, respectively. By setting $S_2(t, \bar{t}; \mathbf{E}) \approx 1$ in Eq. 6.20 we obtain

$$K_{\text{field}}^{(2)}(t, \bar{t}) = -\frac{i}{\hbar} \hat{P} H_{\text{field}}(t) \hat{Q} U_2^{(\text{mol})}(t - \bar{t}) \hat{Q} H_{\text{field}}(\bar{t}) \hat{P} . \tag{6.29}$$

One may expect that it describes two–photon transitions. However, there is not any distinct criteria telling us up to which field–strengths **E** the time–evolution of the state vector $\Psi_1(t)$ computed in using $K_{\text{field}}^{(2)}$ is correct. We can only conclude that a reduction to such a field–strength region may lead to acceptable results where the excited state population $P_e$ depends on the fourth–order of **E**, i. e. $P_e \sim \mathbf{E}^4$. Since this dependence corresponds to a second–order perturbation theory with respect to the molecule radiation field coupling (see also Appendix A.1) it indicates the correctness of the solution of the time–dependent Schrödinger equation.

The third–order contribution with respect to the field–strength follows if the linear

expansion term of $S_2(t, \bar{t}; \mathbf{E})$ is take. We obtain

$$
\begin{aligned}
K_{\text{field}}^{(3)}(t, \bar{t}) \;=\; & -\frac{1}{\hbar^2} \int_{\bar{t}}^{t} dt_1 \, \hat{P} H_{\text{field}}(t)\hat{Q} \\
& \times U_2^{(\text{mol})}(t - t_1)\hat{Q} H_{\text{field}}(t_1)\hat{Q} U_2^{(\text{mol})}(t_1 - \bar{t})\hat{Q} H_{\text{field}}(\bar{t})\hat{P} \,. \quad (6.30)
\end{aligned}
$$

Respective primary system electronic matrix elements read

$$
\begin{aligned}
K_{ab}^{(2)}(t, \bar{t}) \;=\; & -\frac{i}{\hbar} \langle \varphi_a | \hat{\boldsymbol{\mu}} \hat{Q} U_2^{(\text{mol})}(t - \bar{t})\hat{Q}\hat{\boldsymbol{\mu}} | \varphi_b \rangle \, \mathbf{E}(t)\mathbf{E}(\bar{t}) \\
\equiv\; & -\mathbf{D}_{ab}^{(2)}(t - \bar{t})\mathbf{E}(t)\mathbf{E}(\bar{t}) \,, \quad (6.31)
\end{aligned}
$$

and

$$
\begin{aligned}
K_{ab}^{(3)}(t, \bar{t}) \;=\; & -\frac{1}{\hbar^2} \int_{\bar{t}}^{t} dt_1 \, \langle \varphi_a | \hat{\boldsymbol{\mu}} \hat{Q} U_2^{(\text{mol})}(t - t_1)\hat{Q}\hat{\boldsymbol{\mu}}\hat{Q} U_2^{(\text{mol})}(t_1 - \bar{t})\hat{Q}\hat{\boldsymbol{\mu}} | \varphi_b \rangle \\
& \times \mathbf{E}(t)\mathbf{E}(t_1)\mathbf{E}(\bar{t}) \\
\equiv\; & -\int_{\bar{t}}^{t} dt_1 \mathbf{D}_{ab}^{(3)}(t - t_1, t_1 - \bar{t})\mathbf{E}(t)\mathbf{E}(t_1)\mathbf{E}(\bar{t}) \,. \quad (6.32)
\end{aligned}
$$

The coupled equations of motion for the vibrational wave functions may be written as

$$
\begin{aligned}
i\hbar \frac{\partial}{\partial t} \chi_a(t) \;=\; & H_a(t)\chi_a(t) - \mathbf{E}(t)\sum_b \mathbf{d}_{ab}\chi_b(t) \\
& - \sum_b \int_{t_0}^{t} d\bar{t} \, \mathbf{D}_{ab}^{(2)}(t - \bar{t})\mathbf{E}(t)\mathbf{E}(\bar{t})\chi_b(\bar{t}) \\
& - \sum_b \int_{t_0}^{t} d\bar{t} \int_{\bar{t}}^{t} dt_1 \, \mathbf{D}_{ab}^{(3)}(t - t_1, t_1 - \bar{t})\mathbf{E}(t)\mathbf{E}(t_1)\mathbf{E}(\bar{t})\chi_b(\bar{t}) \,.
\end{aligned}
$$

$$(6.33)$$

For further use we give somewhat more explicit expressions for the NMT–coupling functions. Introducing an expansion with respect to secondary electronic states it follows

$$\mathbf{D}_{ab}^{(2)}(\tau) = \frac{i}{\hbar} \sum_x \mathbf{d}_{ax} e^{-iH_x \tau/\hbar} \mathbf{d}_{xb} \,, \tag{6.34}$$

and

$$\mathbf{D}_{ab}^{(3)}(\tau, \bar{\tau}) = \frac{1}{\hbar^2} \sum_{x,y} \mathbf{d}_{ax} e^{-iH_x \tau/\hbar} \mathbf{d}_{xy} e^{-iH_y \bar{\tau}/\hbar} \mathbf{d}_{yb} \,. \tag{6.35}$$

We neglect vibrational contributions and introduce the DOS of the secondary states

$$\mathbf{D}_{ab}^{(2)}(\tau) = \frac{i}{\hbar} \int d\Omega \, \varrho(\Omega) \mathbf{d}(a, \Omega) e^{-i\Omega\tau} \mathbf{d}(\Omega, b) \,, \tag{6.36}$$

and

$$\begin{aligned}
\mathbf{D}_{ab}^{(3)}(\tau, \bar{\tau}) &= \frac{1}{\hbar^2} \int d\Omega d\bar{\Omega} \, \varrho(\Omega) \varrho(\bar{\Omega}) \\
&\times \mathbf{d}(a, \Omega) e^{-i\Omega\tau} \mathbf{d}(\Omega, \bar{\Omega}) e^{-i\bar{\Omega}\bar{\tau}} \mathbf{d}(\bar{\Omega}, b) \,.
\end{aligned} \tag{6.37}$$

To estimate the time–dependence of both NMT coupling functions we assume a structureless DOS and a weak $\Omega$ and $\bar{\Omega}$ dependence of the transition dipole matrix elements. Then, the time–dependence of $\mathbf{D}_{ab}^{(2)}(\tau)$ is mainly determined by $-i/(\tau - i\varepsilon)$ ($\varepsilon \to +0$), i.e. it is localized at $\tau = 0$. For $\mathbf{D}_{ab}^{(3)}(\tau, \bar{\tau})$ one finds a similar behavior with a localization at $\tau = 0$ and $\bar{\tau} = 0$. The $\delta$–function like time localization (of the real part) of $\mathbf{D}_{ab}^{(2)}$ and $\mathbf{D}_{ab}^{(3)}$ is weakened if the concrete frequency dependence of the DOS and the transition dipole moments is taken into account. Since the energy spectrum of polyatomic molecules is dense we get strongly localized coupling functions $\mathbf{D}_{ab}^{(2)}$ and $\mathbf{D}_{ab}^{(3)}$ at least in a time interval of some fs (given by the inverse frequency interval which mainly contributes to the integrations).

## 6.4.2. Time-local version

Eq. (6.27) is an exact TL equation for the primary system. Unfortunately the computation of the inverse operator $[1 - \hat{\Sigma}(t)]$ is impossible for all non-trivial cases of interest. The standard way to find a convenient approximation is the perturbative expansion of the time-dependent generator. We start with

$$\hat{G}(t) = \hat{P} H_{\text{field}}(t) \hat{Q} (1 - \hat{\Sigma}(t))^{-1} \hat{\Sigma}(t) \hat{P} \equiv \hat{P} H_{\text{field}}(t) \hat{Q} \sum_{m=1}^{\infty} \hat{\Sigma}^m(t) \hat{P} \,, \qquad (6.38)$$

which is not the desired perturbative expansion since $\hat{\Sigma}$ depends on all orders of the laser–matter coupling. Therefore, a respective expansion of $\hat{\Sigma}$ becomes necessary first. We note the separation of $U_2(t, \bar{t}; \mathbf{E})$ into $U_2^{(\text{mol})}(t - \bar{t})$ and $S_2(t, \bar{t}; \mathbf{E})$ (cf. Section 6.3.1) as well as the similar separation of the complete time evolution operator $U(\bar{t}, t; \mathbf{E})$. Now, an expansion with respect to the laser–matter coupling becomes possible by expanding the respective $S$–operators, i.e. $S_2 \approx 1 + S_2^{(1)}$ and $S \approx 1 + S^{(1)}$ resulting in

$$\hat{\Sigma}^{(1)}(t) = -\frac{i}{\hbar} \int_{t_0}^{t} d\bar{t} \, U_2^{(\text{mol})}(t - \bar{t}) \hat{Q} H_{\text{field}}(\bar{t}) \hat{P} U^{(\text{mol})}(\bar{t} - t) \,, \qquad (6.39)$$

and in

$$\begin{aligned}
\hat{\Sigma}^{(2)}(t) = \quad & -\frac{1}{\hbar^2} \int_{t_0}^{t} d\bar{t} \int_{\bar{t}}^{t} dt_1 \, U_2^{(\text{mol})}(t - t_1) \hat{Q} H_{\text{field}}(t_1) \hat{Q} U_2^{(\text{mol})}(t_1 - \bar{t}) \quad (6.40) \\
& \times \hat{Q} H_{\text{field}}(\bar{t}) \hat{P} U^{(\text{mol})}(\bar{t} - t) + U_2^{(\text{mol})}(t - \bar{t}) \hat{Q} H_{\text{field}}(\bar{t}) \hat{P} \\
& \times U_1^{(\text{mol})}(\bar{t} - t_1) \hat{P} H_{\text{field}}(t_1) \hat{P} U^{(\text{mol})}(t_1 - t) \,.
\end{aligned}$$

The expansion of the generator up to the third order reads

$$\hat{G}(t) \approx \hat{G}^{(2)}(t) + \hat{G}^{(3)}(t) \,, \qquad (6.41)$$

with

$$\hat{G}^{(2)}(t) = \hat{P} H_{\text{field}}(t) \hat{Q} \hat{\Sigma}^{(1)}(t) \qquad (6.42)$$

and with

$$\hat{G}^{(3)}(t) = \hat{P}H_{\text{field}}(t)\hat{Q}\left[\hat{\Sigma}^{(2)}(t) + \hat{\Sigma}^{(1)}(t)\hat{\Sigma}^{(1)}(t)\right] = \hat{P}H_{\text{field}}(t)\hat{Q}\hat{\Sigma}^{(2)}(t). \quad (6.43)$$

For $G^{(2)}(t)$ which is responsible for two-photon transitions we explicitly obtain

$$\hat{G}^{(2)}(t) = -\frac{i}{\hbar}\int_{t_0}^{t}d\bar{t}\,\hat{P}H_{\text{field}}(t)\hat{Q}U_2^{(mol)}(t-\bar{t})\hat{Q}H_{\text{field}}(\bar{t})\hat{P}U^{(mol)}(\bar{t}-t). \quad (6.44)$$

The three-photon term is given by

$$
\begin{aligned}
\hat{G}^{(3)}(t) = \quad & -\frac{1}{\hbar^2}\int_{t_0}^{t}d\bar{t}\int_{\bar{t}}^{t}dt_1\left(\hat{P}H_{\text{field}}(t)\hat{Q}U_2^{(mol)}(t-t_1)\hat{Q}H_{\text{field}}(t_1)\hat{Q}\right. \quad (6.45)\\
& \times U_2^{(mol)}(t_1-\bar{t})\hat{Q}H_{\text{field}}(\bar{t})\hat{P}U^{(mol)}(\bar{t}-t) + U_2^{(mol)}(t-\bar{t})\\
& \left.\times\hat{Q}H_{\text{field}}(\bar{t})\hat{P}U_1^{(mol)}(\bar{t}-t_1)\hat{P}H_{\text{field}}(t_1)\hat{P}U^{(mol)}(t_1-t)\right).
\end{aligned}
$$

We can extract the two and three photon coupling operators by expanding the corresponding terms in the primary electronic states. Noting the definition of $\mathbf{D}_{ab}^{(2)}$, Eq.(6.36), and $\mathbf{D}_{ab}^{(3)}$, Eq.(6.37), we may write

$$\tilde{\mathbf{D}}_{ab}^{(2)}(t-\bar{t}) = \mathbf{D}_{ab}^{(2)}(t-\bar{t})e^{-iH_b(\bar{t}-t)/\hbar}, \quad (6.46)$$

$$\tilde{\mathbf{D}}_{ab}^{(3)}(t,\bar{t},t_1) = \mathbf{D}_{ab}^{(3)}(t-t_1,t_1-\bar{t})e^{-iH_b(\bar{t}-t)/\hbar}. \quad (6.47)$$

With these coupling operators the effective vibrational Schrödinger equation in the
TL approach is given by

$$
\begin{aligned}
i\hbar \frac{\partial}{\partial t}\chi_a(t) \;=\;& H_a(t)\chi_a(t) - \mathbf{E}(t)\sum_b \mathbf{d}_{ab}\chi_b(t) \\
& - \sum_b \int_{t_0}^{t} dt_1\, \tilde{\mathbf{D}}^{(2)}_{ab}(t-\bar{t})\mathbf{E}(t)\mathbf{E}(\bar{t})\chi_b(t) \\
& - \sum_b \int_{t_0}^{t} d\bar{t} \int_{\bar{t}}^{t} dt_1\, \tilde{\mathbf{D}}^{(3)}_{ab}(t,\bar{t},t_1)\mathbf{E}(t)\mathbf{E}(\bar{t})\mathbf{E}(t_1)\chi_b(t)\,.
\end{aligned}
$$

$$(6.48)$$

In contrast to Eq. 6.33 the vibrational functions $\chi_b(t)$ do not depend on the inte-
gration variables which is an advantage of the TL approach.

## 6.5. Some Specifications

The two versions of effective NMT Schrödinger equations are specified next. First,
in using the RWA we introduce an approximation scheme that leads to TL Schrödinger
equations also when starting with the TNL projection operator formalism. Then, the
NMT Schrödinger equation obtained by the TL projection operator formalism is ex-
panded with respect to vibrational eigenstates to arrive at the equations used in the
numerics.

### 6.5.1. Time-nonlocal version

In order to arrive at the RWA we expand the molecular wave function with respect
to powers of the basic oscillation $\sim \exp(-i\omega t)$ of the applied pulse. Accordingly,
the vibrational part of the complete molecular state vector reads

$$
\chi_a(t) = \sum_n e^{-in\omega t}\chi_a(n;t)\,,
$$

$$(6.49)$$

with $n$ running over all integers (and finally with $a = g, e, f$). This expansion is used to transform the coupled time–dependent Schrödinger equations for the $\chi_a(t)$ into those for the expansion coefficients $\chi_a(n;t)$. It follows an equation of type $\sum_n e^{-in\omega t} f(n;t) = 0$ where the $f(n;t)$ are determined by the original time–dependent Schrödinger equations. Then, respective time–dependent Schrödinger equations for the $\chi_a(n;t)$ may be derived by setting $f(n;t) = 0$. Since the field envelope and the expansion coefficients $\chi_a(n;t)$ depend on time, however, this procedure is only of an approximate character (it assumes that the different expansion terms in Eq. 6.49 are linearly independent from each other). We obtain

$$
\begin{aligned}
i\hbar \frac{\partial}{\partial t}\chi_a(n;t) &= (H_a - n\hbar\omega)\chi_a(n;t) \\
&- \sum_b d_{ab}\big(E(t)\chi_b(n-1;t) + E^*(t)\chi_b(n+1;t)\big) + \Gamma_a^{(2)}(n;t) + \Gamma_a^{(3)}(n;t)\,.
\end{aligned}
$$
(6.50)

Here, $\Gamma_a^{(2)}$ denotes the term, Eq. A.9 responsible for two–photon transitions and $\Gamma_a^{(3)}$ describes three–photon transitions according to Eq. A.12 (for details see Appendix A.2). Both contributions are non–local in time and include the wave function expansion coefficients as well as the field envelopes at earlier times than $t$. Since these quantities change only weakly on the time–interval $D_{ab}^{(2)}(\tau)$ and $D_{ab}^{(3)}(\tau - \bar\tau, \bar\tau)$ approach zero, we may take them at the actual time. This application of the SVA is justified by the time localization of $D_{ab}^{(2)}$ and $D_{ab}^{(3)}$ in a region of about 1 fs (cf. the discussion at the end of Section 6.4.1), whereas the laser pulse envelope changes on a 100 fs interval what is also valid for vibrational wave functions (see the wave packet dynamics given below).

The remaining time integrals with respect to $D^{(2)}$ and $D^{(3)}$ have been estimated in Ref. [128]. Here, we only present the results. For the two–photon coupling follows

$$
d_{ab}^{(2)} = \int_0^\infty d\tau\, e^{i\nu\omega\tau} D_{ab}^{(2)}(\tau) \approx \frac{\bar\varrho}{\hbar} d_{\mathrm{eff}}^2 = d^{(2)}\,,
$$
(6.51)

where $\bar\varrho$ denotes a representative mean value of the DOS, Eq. 6.3 and $d_{\mathrm{eff}}$ is an

mean transition matrix element form a primary state into the manifold of secondary states. In the same manner we obtain:

$$d_{ab}^{(3)} = \int_0^\infty d\tau \int_0^\tau d\bar{\tau}\, D_{ab}^{(3)}(\tau - \bar{\tau}, \bar{\tau}) e^{i\mu\omega\tau + i\nu\omega\bar{\tau}} \approx \frac{\bar{\varrho}^2}{\hbar^2} d_{\text{eff}}^3 = d^{(3)} \,. \tag{6.52}$$

Of course, a more detailed computation would result in a primary state dependence of $\bar{\varrho}$ and $d_{\text{eff}}$. However, this is outside the scope of the present studies.

We first specify Eq. 6.50 from the TNL case for the case that two photons of the applied field pulse are resonant to the transition from the ground to the first excited state, and three photons for the transition from this first excited state to the higher excited state (the reverse sequence is detailed in Appendix C). To neglect any contribution oscillating with multiples of $\exp(i\omega t)$ we concentrate on $\chi_g(0; t)$, $\chi_e(2; t)$, and $\chi_f(5; t)$. This corresponds to the RWA of Eq. 6.50. It is obtained if all those expansion coefficients are eliminated which include in their Schrödinger equations expressions $H_a - n\hbar\omega$ positioned in an energy range of multiples of $\hbar\omega$. Such a neglect guarantees the absence of any oscillation with multiples of $\omega$ in the remaining expansion coefficients. Moreover any single photon transition is neglected. To simplify the notation below we write $\chi_g(0; t) = \chi_g(t)$, $\chi_e(2; t) = \chi_e(t)$, and $\chi_f(5; t) = \chi_f(t)$.

We obtain for the ground–state vibrational wave function (note $n = 0$)

$$i\hbar \frac{\partial}{\partial t} \chi_g(t) = \left( H_g - 2d^{(2)}|E(t)|^2 \right) \chi_g(t) - d^{(2)} E^{*2}(t) \chi_e(t) \tag{6.53}$$

The equation of motion for the excited state wave function reads

$$\begin{aligned} i\hbar \frac{\partial}{\partial t} \chi_e(t) \;=\;& \left( H_e - 2\hbar\omega - 2d^{(2)}|E(t)|^2 \right) \chi_e(t) \\ & - d^{(2)} E^2(t) \chi_g(t) - d^{(3)} E^{*3}(t) \chi_f(t) \,. \end{aligned} \tag{6.54}$$

Finally, the wave function belonging to the further excited state obeys

$$i\hbar \frac{\partial}{\partial t}\chi_f(t) = \left(H_f - 5\hbar\omega\right)\chi_f(t) - d^{(3)}E^3(t)\chi_e(t)\,. \tag{6.55}$$

As already indicated in Ref. [127] the two–photon transition from the ground to the first excited state also includes a renormalization of the ground as well as excited state Hamiltonian (ac Stark–effect). A similar contribution is absent when discussing three–photon transitions.

## 6.5.2. Time-local version

Here, we present an expansion of the time–dependent vibrational wave functions with respect to the eigenstates belonging to the Morse–like PESs which will be specified in Section 6.6:

$$\chi_a(t) = \sum_n c_n^a(t)\phi_n^a\,. \tag{6.56}$$

The matrix elements of the photon coupling operator $\mathbf{D}$ are then given by

$$\tilde{D}_{nm}^{ab}(t,\bar{t}) = \frac{i}{\hbar}d_{nm}^{ab}\int d\Omega\rho(\Omega)\,d(a,\Omega)d(\Omega,b)e^{-i\Omega(t-\bar{t})}e^{i\varepsilon_m^b(t-\bar{t})} \tag{6.57}$$

with the matrix elements of the dipole operator

$$d_{nm}^{ab} = \langle\phi_n^a|\mu|\phi_m^b\rangle\,. \tag{6.58}$$

With these definitions the equation for the expansion coefficients reads

$$i\frac{\partial}{\partial t}c_n^a(t) = \varepsilon_n^a c_n^a(t) - \sum_{m,b}\Gamma_{ab,nm}^{(2)}(t)c_m^b(t) - \sum_{m,b}\Gamma_{ab,nm}^{(3)}(t)c_m^b(t) \tag{6.59}$$

where $\Gamma^{(2)}_{ab,nm}$ and $\Gamma^{(3)}_{ab,nm}$ denoting the two-photon and the three-photon coupling terms, respectively. The two-photon term is given by

$$
\begin{aligned}
\Gamma^{(2)}_{ab,nm}(t) &= \int_0^{t-t_0} d\tau\; \mathbf{E}(t)\tilde{D}^{ab}_{nm}(\tau)\mathbf{E}(t-\tau)\\[2mm]
&= E(t)\int_0^{t-t_0} d\tau\; E^*(t-\tau)e^{i\omega\tau}\tilde{D}^{ab}_{nm}(\tau)\\[2mm]
&\quad +E^*(t)\int_0^{t-t_0} d\tau\; E(t-\tau)e^{-i\omega\tau}\tilde{D}^{ab}_{nm}(\tau)\\[2mm]
&\quad +E(t)e^{-i2\omega t}\int_0^{t-t_0} d\tau\; E(t-\tau)e^{-i\omega\tau}\tilde{D}^{ab}_{nm}(\tau)\\[2mm]
&\quad +E^*(t)e^{i2\omega t}\int_0^{t-t_0} d\tau\; E^*(t-\tau)e^{i\omega\tau}\tilde{D}^{ab}_{nm}(\tau)
\end{aligned}
\tag{6.60}
$$

where the definition of the electric field 6.5 was used. Because the field envelope is slowly varying in time we replace $E(t-\tau)$ by $E(t)$. Setting $t_0$ to $-\infty$ the remaining integral can approximated as

$$
\int_0^\infty d\tau\; e^{\pm i\omega\tau}\tilde{D}^{ab}_{nm}(\tau) = -\frac{1}{\hbar}d^{ab}_{nm}\int d\Omega\; \frac{\rho(\Omega)d(a,\Omega)d(\Omega,b)}{E^b_m \pm \omega - \Omega - i\epsilon}\;.
\tag{6.61}
$$

Because the energy range $\Omega$ of the secondary states is much higher than the energies of the vibronic states $E^b_m$ and the electric field $\omega$ we can write

$$
-\frac{1}{\hbar}d^{ab}_{nm}\int d\Omega\; \frac{\rho(\Omega)d(a,\Omega)d(\Omega,b)}{E^b_m \pm \omega - \Omega - i\epsilon} = \frac{1}{\hbar}d^{ab}_{nm}\int d\Omega\; \frac{d^2_{\mathrm{eff}}\rho(\Omega)}{\Omega} = d^{ab}_{nm}d^2_{\mathrm{eff}}\frac{\bar{\rho}}{\hbar}
\tag{6.62}
$$

Here we assumed that the effective constant $d_{\mathrm{eff}}$ is the same as in the TNL case although the averaging procedure differs slightly. With this, Eq. (6.60) can be simplified to yield

$$
\Gamma^{(2)}_{ab,nm}(t) = \mathbf{E}^2(t)d^{ab}_{nm}d^2_{\mathrm{eff}}\frac{\bar{\rho}}{\hbar} = \mathbf{E}^2(t)d^{ab}_{nm}d^{(2)}.
\tag{6.63}
$$

Similar approximations can be performed for the three-photon term

$$
\Gamma^{(3)}_{ab,nm}(t) = \mathbf{E}^3(t)d^{ab}_{nm}d^3_{\mathrm{eff}}\frac{\bar{\rho}^2}{\hbar^2} = \mathbf{E}^3(t)d^{ab}_{nm}d^{(3)}.
\tag{6.64}
$$

The complete equation for the time evolution of the expansion coefficients reads

$$i\hbar\frac{\partial}{\partial t}c_n^a(t) = \varepsilon_n^a c_n^a(t) - \mathbf{E}^2(t)d^{(2)}\sum_{m,b} d_{nm}^{ab}\, c_m^b(t) - \mathbf{E}^3(t)d^{(3)}\sum_{m,b} d_{nm}^{ab}\, c_m^b(t)\,. \quad (6.65)$$

At this point one can go back to a representation independent formulation

$$i\hbar\frac{\partial}{\partial t}\chi_a(t) = H_a\chi_a(t) - \mathbf{E}^2(t)d^{(2)}\sum_{b}\chi_b(t) - \mathbf{E}^3(t)d^{(3)}\sum_{b}\chi_b(t)\,. \quad (6.66)$$

This equation can be applied in a straightforward manner leading to differential equations for $\chi_g(t)$, $\chi_e(t)$, and $\chi_f(t)$. Different from the equations for the TNL case 6.53 to 6.55 all processes are still included and one does not have to distinguish beforehand if one wants to treat a sequence of 2-photon and 3-photon processes or vice versa. Nevertheless one can derive Eqs. 6.53 to 6.55 which are based on the TNL projection operator formalism by performing the RWA, i.e. replacing $H_a$ by the respective $H_a - n\hbar\omega$ and replacing the field $\mathbf{E}(t)$ by its envelope $E(t)$. Furthermore all terms far outside the energy range of the 2-photon and 3-photon processes have to be neglected. The numerical results in the next Section have been achieved using Eq. 6.66 but using Eqs. 6.53 to 6.55 including the RWA does not lead to any visible deviations since the requirements for the RWA are fulfilled in those examples.

## 6.6. Numerical Results

As already indicated, our numerical computations will focus on an electronic three–level system defined versus a single vibrational coordinate. To stay sufficient simple we chose Morse type PES:

$$V(R) = E_D(1 - e^{-\beta(R-R_0)^2}) + E_0\,. \quad (6.67)$$

All three PES are shown in Fig. 6.2 (the parameters are given below). They resemble those PES typical for alkali dimers like $NaK$ (see [146] and references therein) as well as the one–dimensional PES used to describe NMT processes in a metal organic compound in Refs. [127, 128]. The concrete mutual energetic position has been taken to allow for a sequence of two–photon and three–photon transitions
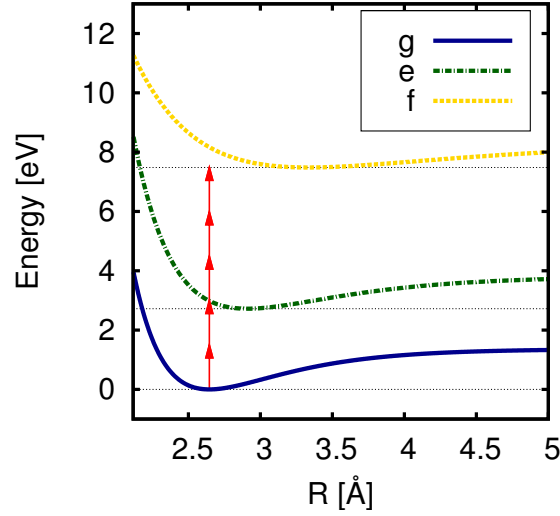
**Figure 6.2.:** Potential energy surfaces in an electronic three-level system. The energy of the laser pulse can lead to a 2-photon transition between the ground and first excited state and a 3-photon transition between the first and second excited state.

(this would be also possible in the metal organic compound used in [127, 128]). Moreover, the shape of the PES was chosen such that wave packet dynamics proceed roughly in the 100 fs region. (If the curvature of the PES would be more flat the wave packet dynamics would enter the 1 ps region being of less interest for the demonstration of ultrafast NMT processes.) First, we focus on a two–level version of our system, to study afterwards different laser pulse excitation schemes in the full three–level system.

## 6.6.1. Comparison of different approaches

Aim of this subsection is to compare the different approaches for a model system in which a 2-photon transition takes place. The test system consists of two electronic surfaces of Morse type (similar to two of the three PES shown in Fig. 6.2)

The parameter $E_D$ is 1.36 eV for both PES while the upper surface is shifted by $E_0 = 2.72$ eV in energy. The minimum of the PES $R_0$ is at 2.56 Å for both PES and $\beta$ is 1 $a_0^{-1}$ for the ground state and 0.8 $a_0^{-1}$ for the excited state PES. The system parameters $d_{eff}$ and $\bar{\rho}$ are chosen to be 1 D and 36.75 $eV^{-1}$, respectively. As density of states $\rho(\Omega)$ a step function was assumed so that $\rho(\Omega) = 0$ for $\Omega <$
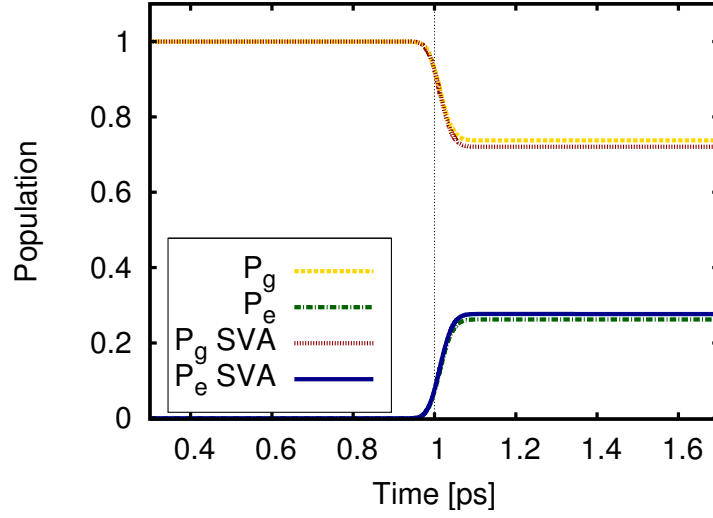
**Figure 6.3.:** Comparison of the population dynamics during a 2-photon process transition using the TL approach without and with SVA.

$\Omega_{min}$ and $\Omega > \Omega_{max}$ and 36.75 eV$^{-1}$ elsewhere. With this, the value of $\bar{\rho}$ equals 36.75 eV $\times \log(\Omega_{max}/\Omega_{min})$. For the present example, $\Omega_{min}$ was set to 27.2 eV and $\Omega_{max}$ to 81.6 eV. The envelope of the applied laser pulse (see Eq. 6.5) has Gaussian shape $E(t) = A \exp\left(-(t - T)^2/(2\sigma^2)\right)$ with $T = 1000$ fs, $\sigma = 42.5$ fs (FWHM = 100 fs). The prefactor $A$ is determined by the fluence $F = \int_0^\infty |E(t)|^2 dt$ which is chosen to $10^4$ [GV/m]$^2$fs. To induce a 2-photon process the carrier frequency $\omega$ has the value 1.36 eV, i.e. half of the energetic difference between the two PES. The lowest vibrational state of the electronic ground state is chosen as the initial wave function.

One formalism to be compared is the TL theory without further approximations as given in Eq. 6.48. The second and third approaches are the TNL formalism including RWA and SVA and the TL approach with SVA. Fig. 6.3 compares these different approximation in showing the temporal evolution of the electronic level populations

$$P_a(t) = \sum_n |c_n^a(t)|^2 \,. \tag{6.68}$$

As discussed above the TNL approach with RWA and SVA and the TL formalism with SVA lead to very similar equations. Therefore it is no surprise that they result

in the same values for the population dynamics and are shown only as one result in Fig. 6.3. So the question is how accurate do agree the results obtained without using the SVA (computed in the TL formalism) with the approximated values. As can be seen in Fig. 6.3 for the population dynamics of the ground and excited state the agreement is very good. Since the computational effort to determine the values without the SVA are much larger due to the calculation of the time integrals at every time step, this result is very important for further calculations of NMT processes. Since already for 2-photon processes the numerical effort without SVA is large, it is even much higher when going to 3-photon processes for which a double-time integral has to be calculated at every moment in time (see Eq. 6.48). Below all results are obtained in the TL formalism including the SVA allowing for an efficient calculation of NMT processes.

## 6.6.2. Sequence of a 2-photon and a 3-photon processes

In this subsection three different pulses are applied to a system of three electronic levels as depicted in Fig. 6.2. The minima $R_0$ of the PES are located at 2.65 Å, 2.91 Å, and 3.33 Å for the ground ($g$), first excited ($e$), and second excited ($f$) PES, respectively. The parameters $E_D$ have the values 1.36 eV, 1.09 eV, and 0.82 eV and the parameters β the values 1 $a_0^{-1}$, 0.8 $a_0^{-1}$, and 0.5 $a_0^{-1}$, respectively for the $g$, $e$ and $f$ PES. In addition there is an energetic shift between ground and first excites state of 2.72 eV and of 7.5 eV between the ground and second excited states. The system parameters $d_{eff}$ and $\bar{\rho}$ are chosen to be 1 D and 36.75 eV$^{-1}$, respectively.

The three different pulses schemes are shown in Fig. 6.4. The fluence in all three schemes is restricted to 5.4×10$^4$ [GV/m]$^2$fs. In the first single–pulse scenarios the pulses are centered around 1000 fs and have a FWHM of 100 fs an 250 fs, respectively. The third pulse scenario consists of two sub–pulses with FWHM of 100 fs centered at 700 fs and 1360 fs. To induce a 2-photon process between the ground and first excited state the carrier frequency ω was chosen to be 1.5 eV. This is not exactly twice the energetic difference between these two PES since they are also shifted in coordinate space. Again the lowest vibrational state of the electronic ground state is chosen as initial wave packet. Therefore the 2-photon process does not take place between the lowest vibrational states of the ground and
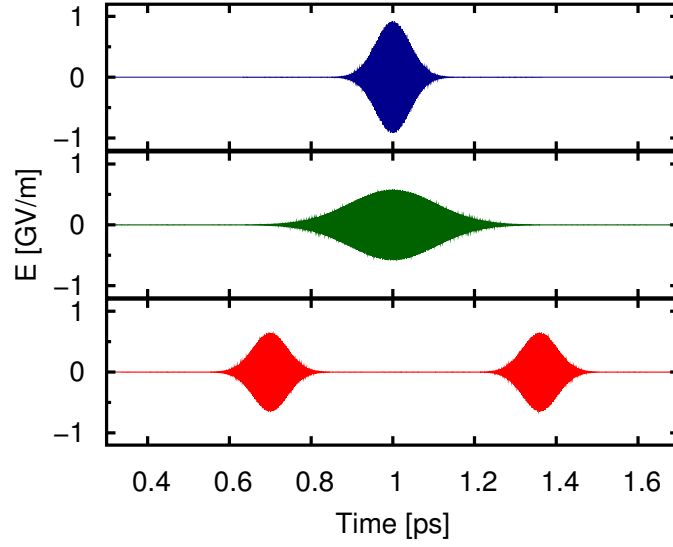
**Figure 6.4.:** Three different pulse scenarios to create a sequence of 2- and 3-photon transitions in a three-level system.

first excited PES but between the lowest vibrational states of the ground PES and higher vibrational states of the first excited PES. Due to the limited length of the pulse it has a non-negligible width in frequency space and can excite more than one vibrational state.

The electronic population dynamics for the 100 fs long single pulse is shown in Fig. 6.5. Initially all population is in the ground state. During the action of the laser pulse, population is transfered from the ground to the first excited state, here between the vibrational ground state of the lower PES to the 16th vibrational state of the upper one.

Wave packet dynamics on the first excited state is shown in Fig. 6.6 by drawing the vibrational coordinate probability distribution in a particular electronic state

$$P_a(R,t) = |\chi_a(R,t)|^2 \equiv |\sum_n c_n^a(t)\phi_n^a(R)|^2 \tag{6.69}$$

versus time. One can clearly see that the wave packet shows an oscillatory movement. During the pulse action the energetics is unfavorable for a transfer between the first and the second excited state. This can be already be envisioned from the sketch in Fig. 6.2. The difference between the minima of the first and second excited state would allow for a 3-photon processes but since the PES are shifted with
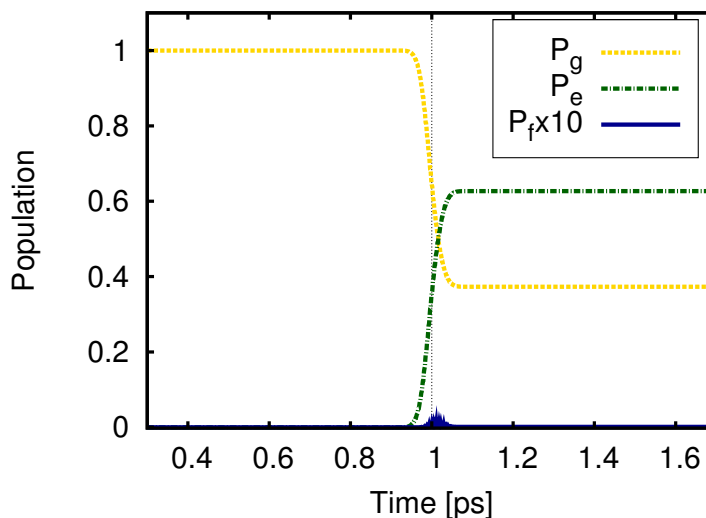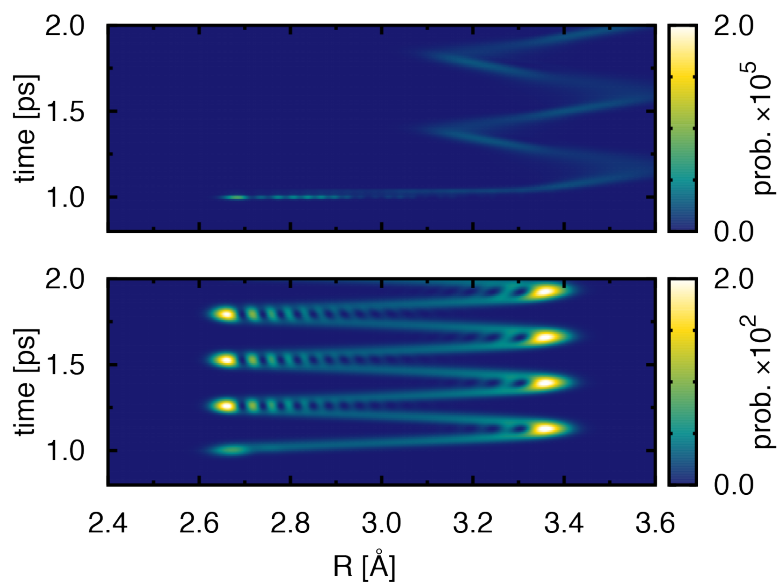
**Figure 6.5.:** Population dynamics in the three-level system under the influence of a 100 fs pulse.

respect to each the Franck-Condon overlap for the energetically accessible states is vanishing.

This changes when a longer pulse, for example, a 250 fs pulse is applied. The corresponding population and wave packet dynamics are shown in Figs. 6.7 and 6.8, respectively. First, population is transfered from the ground to the first excited state. However, the laser pulse is still acting when the wave packet in the first excited state enters the Franck-Condon window of the transition into the higher excited state. Therefore, a considerable amount of population is transfered via a 3-photon processes to the second excited state. The absolute value of this population transfer, of course, is small since in total the transfer from the ground to the second excited state corresponds to a process which is of 5th-order in the laser-field strength. This is mainly originated by the need to work in a field–strength region which can be also reached by multiphoton transition perturbation theory (cf. the discussion in Section 6.4). Comparing the present field–strength region of 1 GV/m with the 10 to 30 GV/m region of Ref. [128] (the used molecular parameters are similar) the limit of the validity of perturbation theory is not exceeded (in [128] a dependence of the excited state population $\sim \mathbf{E}^4$ and $\sim \mathbf{E}^6$ has been confirmed).

A third pulse scenario was shown in Fig. 6.4, a sequence of two 100 fs pulses

**Figure 6.6.:** Wave packet dynamics in the three-level system under the influence of a 100 fs pulse. The lower panel shows $P_e R, t$, Eq. 6.69 (probability distribution in the first excited state) while the upper panel displays $P_f R, t$ (probability distribution in the second excited state, note the different scales of the color coding).
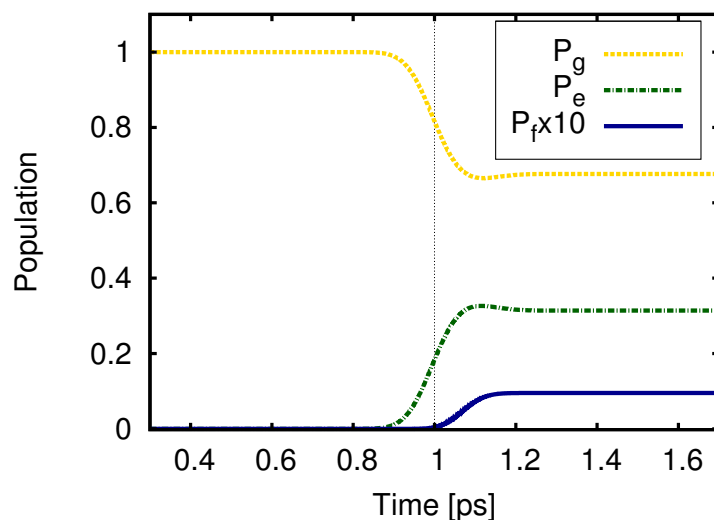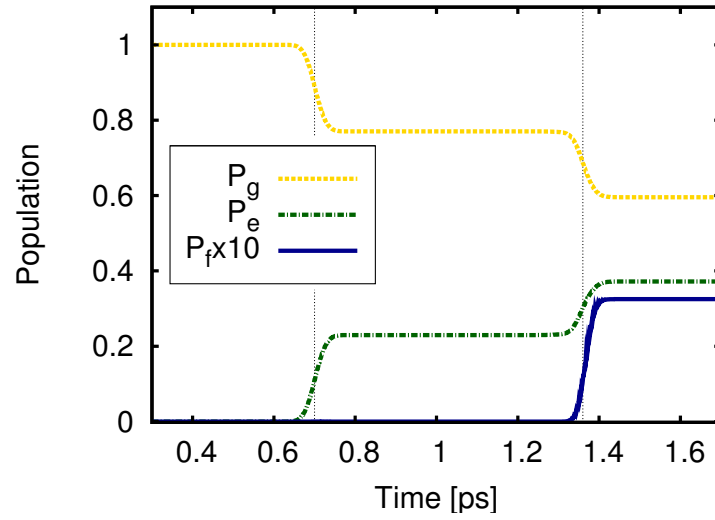


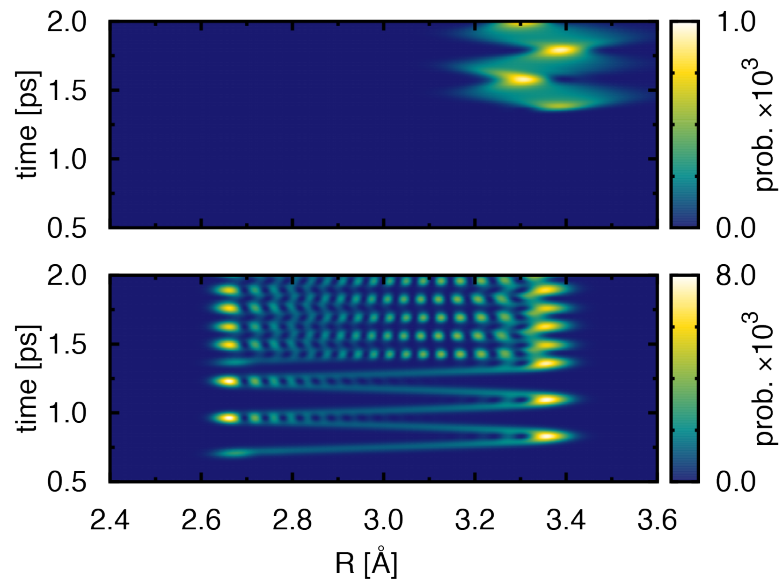**Figure 6.7.:** Same as in Fig. 6.5 but using a 250 fs pulse.
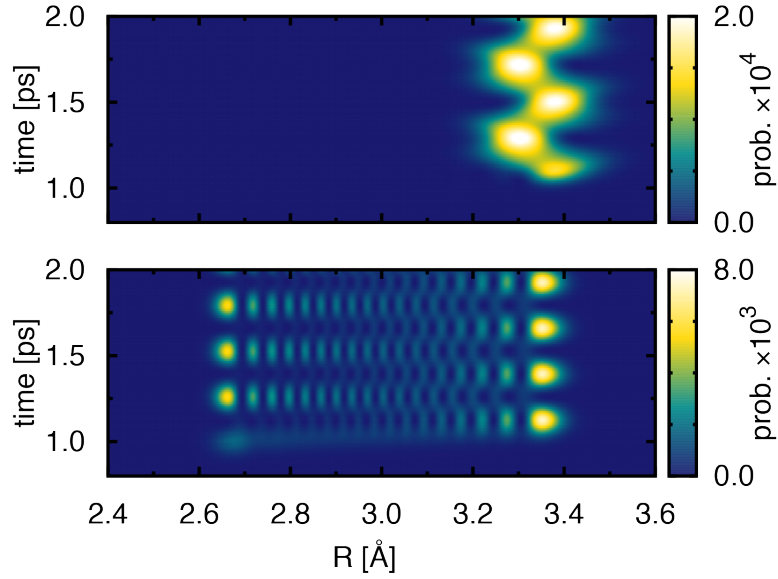
**Figure 6.8.:** Same as in Fig. 6.6 but using a 250 fs pulse. Note the change in the scale of the color coding.

separate by 660 fs. The corresponding population and wave packet dynamics are shown in Figs. 6.9 and 6.10, respectively. The first pulse stimulates a 2-photon process from the ground to the first excited state. No transfer to the second excited state can take place because the wave packet is outside the Franck-Condon overlap region for the energetically accessible states. This changes with the second 100 fs pulse. The effect of this pulse is twofold. On one side it further transfers population from the ground to the first excited state. But on the other side due to the selected temporal separation between the two pulses, the wave packet on the first excited state created by the first pulse moved into the Franck-Condon overlap region and a 3-photon transfer from the first to the second excited state can take place.

Above we have concentrated ourself on a model system in which a 2-photon and then a 3-photon transition can take place. In Section 5 the formulas were also given for schemes in which first a 3-photon and then a 2-photon transition is possible. For such a system setup equivalent results can be achieved.

**Figure 6.9.:** Same as in Fig. 6.5 but using the scenario with two separate 100 fs pulses.



**Figure 6.10.:** Same as in Fig. 6.6 but using the scenario with two separate 100 fs pulses. Note the change in the scale of the color coding.

## 6.7. Conclusions

Projection operator theories have been applied to study NMT processes in molecular systems. Effective time-dependent Schrödinger equations were derived starting from a time-local as well as a time-nonlocal formalism. These effective Schrödinger equations were further simplified by invoking either the SVA alone or the RWA and SVA, respectively. The validity of these approximations was numerically verified which was only possible due to the equations derived from the TL approach. In addition a perturbative description of non-resonant 2-photon transitions has been given in the appendix to further clarify the summation over the non-resonant states (the secondary states in the projection operator approaches).

Other than in previous publications [44, 127, 128] in which the effective Schrödinger equations were only derived from the time-nonlocal formalism and in which the additional approximation could not be tested, here we applied the approach to a sequence of 2-photon and 3-photon transitions. It was shown that for such a sequence of events certain prerequisites of the pulse have to be fulfilled.

Also for sequences of ultrafast NMTs one can imagine to apply optimal control theory as has been done for single NMTs [127, 128]. The numerical effort for using the TL formalism without further approximations would be rather high but using either the TL form with the SVA or the TNL theory with RWA and SVA would make these control calculations numerically tractable. As was shown above these extra approximations work very accurately and do not lead to large deviations from the TL formalism without further approximations.

# 7. Excitation energy transfer in biological pigment complexes

## 7.1. Introduction

In the preceding chapters 3,4 and 5 it was shown that quantum dynamical simulations are a powerful tool to investigate molecular dynamics and help to analyze and understand experimental findings. This was demonstrated for simple isolated molecules. The subsequent part of the thesis aims at the extension of this methodology to complex biological systems. In nature there exist a vast multitude of molecular complexes which where structurally optimized to accomplish special functions in biological systems. Two prominent examples are the DNA which stores the genetic instructions in all known living organisms and the photosynthetic apparatus which produces organic compounds using the energy from sunlight[147].

The theoretical description of energy transfer processes in such systems is an important element in understanding the relation between their structure and function. To gain a complete theoretical picture a full quantum dynamical description would be necessary. Since the development of realistic theoretical models in such complex systems is not feasible, numerical simulations emerged as an excellent tool to study these processes. However, time-dependent ab initio calculations for systems with hundreds of thousand atoms are computational too expensive. On the contrary, classical MD simulations are capable to simulate the structural changes in such large systems, but they ignore quantum effects which are important for energy and charge transfer processes and optical properties [48]. One way to overcome this problem is to use MD for the nuclear degrees of freedom and perform simultaneous electronic structure calculations. One prominent example of these *ab initio*
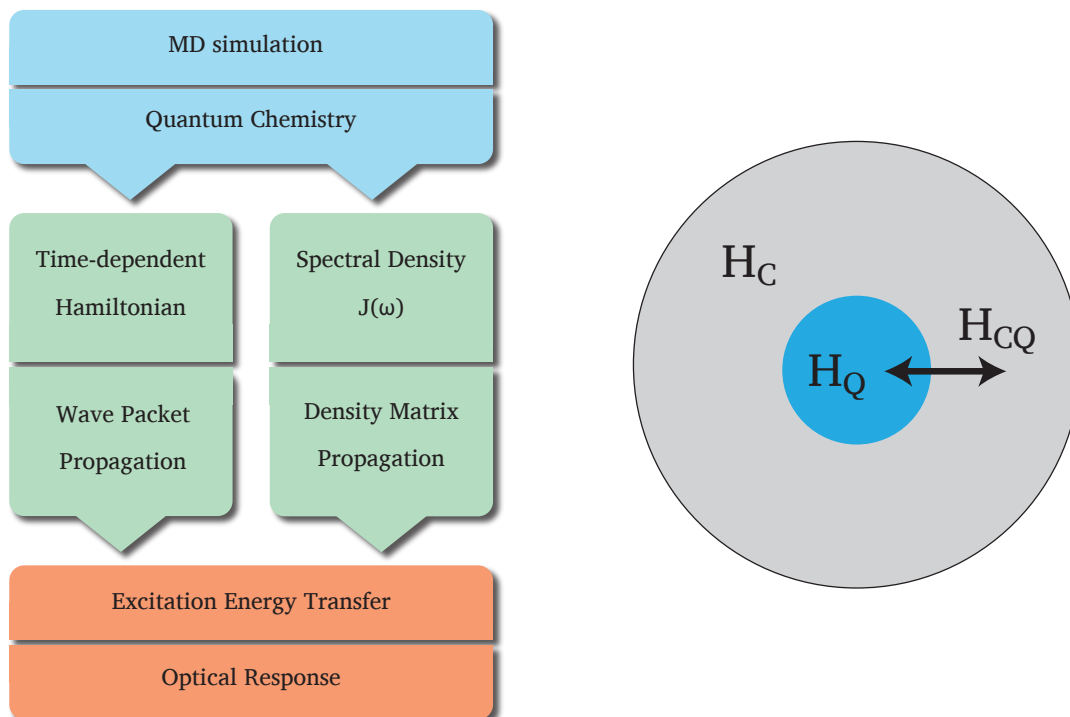
**Figure 7.1.: left:** Simulation scheme of the mixed quantum-classical approach. **right:** Model system for the mixed quantum-classical approach

MD is the Car-Parinello method [148] which can be used to describe systems of a few hundred atoms. For larger system other approximative methods have to be applied. In many cases it is not necessary to describe all degrees of freedom quantum mechanically but it is sufficient to use classical MD for the main part of the system and treat only those degrees of freedom quantum mechanically which are relevant for the process under investigation. The complete system is divided in a classical and a quantum part which influence each other trough couplings. Fig. 7.1 depicts this schematically. There exist several approaches to accomplish this, e.g. the Ehrenfest method [149] and surface hopping [150–152]. In the Ehrenfest method the quantum subsystem is described by wave packet propagation which allow to include electronic transition. The forces acting on the classical subsystem in turn are calculated by averaging over the time-dependent wave function of the quantum subsystem.

In the following part, the application of wave packet simulations for the description

of excitation energy transfer in large biological systems is investigated. Applications would be for example the excitation energy transfer in light-harvesting (LH) systems which are an essential part of the photosynthetic apparatus found in plants and some bacteria. They absorb light and transfer the excitation energy to the photosynthetic reaction center. These systems are very large and a reasonable model system would contain up to $10^5$ atoms. They consist of pigment molecules embedded in a protein structure. The pigments are the optical active components of the LH complexes and are responsible for the absorption and transfer of the excitation energy. The protein environment has also a strong influence on the tranfer dynamics and need to be included in the description. Due to the size of these systems approaches which include the influence of the quantum system on the classical system are still computationally too expensive. A further approximation is to neglect this influence. This assumption can be justified by the fact that the pigments are small compared to the protein environment and that an excitation in one of these pigments would not change the structure of the whole complex considerably. Therefore the classical system can be described by a parametrized force field which enables for MD simulation of systems with more then $10^5$ atoms. The pigments are then described as a quantum subsystem. A possible methodology of such a simulation is depicted in Fig. 7.1. Based on the trajectory from the MD simulation the Hamiltonian for the pigments is determined by performing electronic structure calculations for certain time steps of the MD trajectory. These calculations result in time-dependent excitation energies for the individual pigments and coupling factors between them. These can then be used to build a model Hamiltonian for ensemble averaged wave packet calculations, i.e., the numerical integration of the Schrödinger equation [50, 51]. This approach has the advantage of utilizing directly the full time dependence of couplings, transition dipole moments and other quantities obtained from the MD/QC approach. Disadvantageous is that the wave-packet based approach includes an implicit high-temperature assumption and therefore does not yield the correct thermal state in the long time limit. Another possibility is to calculate a spectral density out of the excitation energy fluctuations for a density and use density matrix theories to determine population dynamics and spectra. The disadvantage of this technique is that it involves several averaging procedures to obtain a time-independent Hamiltonian coupled to an environment which causes loss of information during the averaging processes.

In the following a method proposed by A. Bastida and co-workers [66–68] is discussed which modifies the wave packet approach in such a way that it conserves the correct temperature behaviour. This methodology will be explained in detail and applied to the two-level model system. The results are compared to dissipative density matrix calculations which exhibit the correct temperature behaviour. Finally these calculations are applied to Hamiltonians calculated from resent MD/QC calculations of the light harvesting complex II found in the photosynthetic apparatus of purple bacteria [59, 69, 70].

## 7.2. Theory

As stated above and depicted in Fig. 7.1 the system Hamiltonian is split in a quantum part, $H_Q$, and a classical part, $H_C$. $H_Q$ is the relevant part for the quantum calculation representing the optical active pigment molecules. $H_C$ describes the nuclear dynamics in the complex. Thus the complete system Hamiltonian reads

$$H(\mathbf{r},\mathbf{R}) = H_Q(\mathbf{r}) + H_C(\mathbf{R}) + H_{QC}(\mathbf{r},\mathbf{R}) \,. \tag{7.1}$$

Here $\mathbf{R}$ represents the set of nuclear coordinates, i.e. the degrees of freedom which are treated in a classical approximation and $\mathbf{r}$ the electronic degrees of freedom treated quantum dynamically. Both subsystems are coupled via the coupling operator $H_{QC}(\mathbf{r},\mathbf{R})$. For the modeling of the excitation energy transfer only the electronic excitation of the pigments is treated quantum mechanically. Thus $H_Q$ corresponds to the excitation Hamiltonian of the pigment system. The derivation of this excitation Hamiltonian from the electronic Hamiltonian of the complex will be shown in the following. The electronic Hamiltonian of the complex $H^{el}(R(t))$ depends parametrically on the nuclear coordinates. The nuclear coordinates are determined classically using Newton's equations

$$M_\nu \ddot{\mathbf{R}}_\nu = - \bigtriangledown_\nu \langle \Psi(\mathbf{r},\mathbf{R})|H(\mathbf{r},\mathbf{R})|\Psi(\mathbf{r},\mathbf{R})\rangle \tag{7.2}$$

for the position $\mathbf{R}_\nu$ of the $\nu$th nuclei and its related mass $M_\nu$. The force depends on the wave function $\Psi(\mathbf{r},\mathbf{R})$ of the system and is therefore coupled to the quantum system. The electronic wave functions evolves according to the time-dependent

Schrödinger equation

$$i\hbar\frac{\partial}{\partial t}\Psi(\mathbf{r},R(t)) = H^{el}(R(t))\Psi(\mathbf{r},R(t)) \,. \tag{7.3}$$

As discussed above the influence of the quantum system on the classical system can be neglected here. Therefore the potential $\langle\Psi|H|\Psi\rangle$ appearing in Eq. 7.2 can be replaced by a ground state potential which defines the force field used in the MD simulations.

### 7.2.1. Exciton Hamiltonian

The electronic Hamiltonian of the pigment system can be constructed from the electronic Hamiltonians of the individual pigments labeled by $m$ and the intermolecular Coulomb interactions $V_{mn}(\mathbf{r})$ between them. Therewith the electronic Hamiltonian reads

$$H^{el}(\mathbf{R}) = \sum_m H^{el}_m(\mathbf{R}) + \sum_{mn} V_{mn}(\mathbf{r}) \,. \tag{7.4}$$

To classify the transfer process the electronic part is expanded in terms of the adiabatic electronic states of the single molecules $|\psi_{ma}\rangle$. The label $a$ counts the electronic state of molecule $m$. These states are defined by the stationary Schrödinger equation for a single molecule

$$H^{el}_m(\mathbf{R})\phi_{am}(\mathbf{r},\mathbf{R}) = \varepsilon_{am}(\mathbf{R})\phi_{ma}(\mathbf{r},\mathbf{R}) \,. \tag{7.5}$$

$H^{el}_m(\mathbf{R})$ is basically identical to the electronic Hamiltonian in Eq. 2.10 defined in paragraph 2.2.2. The only difference is that here $\mathbf{R}$ represents all nuclear coordinates of the complete system and not only these of the single pigment molecule. In a next step we assume that there is no overlap between the electronic wave functions

$$\langle\phi_{ma}|\phi_{nb}\rangle = \delta_{ma,nb} \tag{7.6}$$

which is reasonable since the wave functions decrease exponentially with intermolecular distance. Usually the distance between the pigments is larger than 1 nm

so that these intermolecular interactions can be neglected. With this relation, a Hartree product ansatz can be used to construct a complete basis for the electronic wave function

$$\Phi_{\{a\}}(\mathbf{r}_{\{m\}}, \mathbf{R}) = \prod_m^M \phi_{ma}(\mathbf{r}_m, \mathbf{R}) \ . \tag{7.7}$$

The electronic Hamiltonian acting in the state space spanned by these states can now be written in terms of the electronic wave functions $\phi_{ma}$, which reads

$$H^{el} = \sum_m \sum_{ab} H_m^{ab} |\phi_{ma}\rangle \langle \phi_{mb}| + \sum_{mn} \sum_{abcd} V_{mn}^{abcd} |\phi_{ma}\phi_{nb}\rangle \langle \phi_{nc}\phi_{md}| \tag{7.8}$$

with the matrix elements

$$H_m^{ab} = \langle \phi_{ma}|H_m^{el}|\phi_{ma}\rangle \ . \tag{7.9}$$

The off diagonal elements correspond to nonadiabatic couplings which will be neglected. The matrix elements of the Coulomb interaction read

$$V_{nm}^{abcd} = \langle \phi_{ma}\phi_{nb}|V_{nm}|\phi_{nc}\phi_{md}\rangle \ . \tag{7.10}$$

In the following the description is restricted to incorporate only the ground and first excited state of the different molecules. This two-level approximation can be applied if initially only one molecule is excited and the transition energy in all molecules is similar. Therefore the index $a$ in the above equation takes only the values $g$ and $e$ for ground and excited state, respectively. In this approximation only coupling terms $V_{mn}^{egeg} \equiv V_{mn}$ have considerable contribution. This results in

$$H^{el} = \sum_m \sum_{a=g,e} \varepsilon_{ma} |\phi_{ma}\rangle \langle \phi_{ma}| + \sum_{mn} V_{nm} |\phi_{me}\phi_{mg}\rangle \langle \phi_{me}\phi_{mg}| \ . \tag{7.11}$$

The studies presented here investigate the case of a single excitation in the complex, i.e. only one molecule $m$ is in the excited state and all others are in the ground state

$$|m\rangle = |\phi_{me}\rangle \prod_{n\neq m} |\phi_{mg}\rangle \tag{7.12}$$

and the electronic single excitation Hamiltonian is given by

$$H_{el}^{(1)} = \sum_m (E_0 + \varepsilon_{me} - \varepsilon_{mg}) \, |m\rangle \, \langle m| + \sum_{nm} V_{nm} \, |n\rangle \, \langle m| \; . \tag{7.13}$$

This single excitation Hamiltonian will be used to describe the excitation transfer process in the complex and will be referred to as quantum system.

$$H_Q = H_{el}^{(1)} \; . \tag{7.14}$$

The ground state energy is not important and can be set to zero. Additionally we introduce the excitation energy $\varepsilon_m = \varepsilon_{me} - \varepsilon_{mg}$ of molecule $m$ which yields

$$H_Q = \sum_m \varepsilon_m \, |m\rangle \, \langle m| + \sum_{nm} V_{nm} \, |n\rangle \, \langle m| \; . \tag{7.15}$$

Further the eigenvalue equation for this Hamiltonian

$$H_Q \, |\alpha\rangle = \mathcal{E}_\alpha \, |\alpha\rangle \tag{7.16}$$

can be solved. Therefore the eigenstate $|\alpha\rangle$ is expanded in the basis of the singly excited states

$$|\alpha\rangle = \sum_m c_\alpha^m \, |m\rangle \; . \tag{7.17}$$

These states will be referred to as excitonic states of the pigment system. Using this expansion and the obtained excitonic energies the quantum Hamiltonian can be written as

$$H_Q = \mathcal{E}_\alpha \, |\alpha\rangle \, \langle \alpha| \; . \tag{7.18}$$

## 7.2.2. QM/MM modeling

As stated above the nuclear dynamics of the complex are treated classically using MD simulations with static forcefields. The result of these simulations are trajectories of the nuclear coordinates of the complex. With these coordinates the static electronic Schrödinger equation for the individual pigment molecules can be solved

to get the the excitation energies and Coulomb couplings. This can be accomplished with electronic structure methods, like CIS [153], TDDFT[154], or semi-empirical methods like ZINDO/S [155, 156]. The details of this methodology can be found in recent publications from our group [69, 70, 157]. This procedure results in a time-dependent Hamiltonian for the quantum system

$$H(t) = \sum_m \varepsilon_m(t) |m\rangle \langle m| + \sum_{nm} V_{nm}(t) |n\rangle \langle m| \tag{7.19}$$

were $\varepsilon_m(t)$ and $V_{nm}(t)$ are the time dependent excitation energies and Coulomb couplings calculated for every time step of the MD trajectory. To gain the Hamiltonian $H_Q$ (Eq 7.15) for the isolated quantum system we assume that the time average of the time-dependent Hamiltonian 7.19 corresponds to the electronic structure of the equilibrium configuration of the nuclear coordinates

$$\langle H(t, \mathbf{R(t)}) \rangle \equiv H_Q . \tag{7.20}$$

The effect of the classical part onto the quantum part can now be considered as fluctuations which are added to the excitation energies and couplings due to the displacement of the nuclei from the equilibrium configuration. These fluctuations define the the action of the classical system on the quantum system degrees of freedom.

$$H_{QC} = \langle \Psi_Q | H_{QC} | \Psi_Q \rangle = (H(t, \mathbf{R(t)}) - \langle H(t, \mathbf{R(t)}) \rangle) \tag{7.21}$$

Since we neglect any influence from the quantum system on the classical system $\langle \Psi_C | H_{QC} | \Psi_C \rangle = 0$ this is the total interaction Hamiltonian $H_{QC}$. It can be given in terms of the single excited pigment states

$$H_{QC}(t) = \sum_m \Delta\varepsilon_m(t) |m\rangle \langle m| + \sum_{m \neq n} \Delta V_{mn}(t) |m\rangle \langle n| . \tag{7.22}$$

Here the $\Delta\varepsilon_m(t)$ and $\Delta V_{mn}(t)$ are the fluctuations of the excitation energies and the couplings with respect to the average Hamiltonian. If we now combine Eqs. 7.1, 7.15 and 7.22 we can arrange the time dependent Schrödinger equation for

the quantum system

$$i\hbar\frac{\partial}{\partial t}|\Psi_Q(t)\rangle = (H_Q + \langle\Psi_Q|H_{QC}(t)|\Psi_Q\rangle)|\Psi_Q\rangle \ . \tag{7.23}$$

If the wave function of the quantum system is expanded in terms of the excitonic states $|\alpha\rangle$ (Eq. 7.17) of the pigment system

$$|\Psi_Q(t)\rangle = \sum_\alpha c_\alpha(t)|\alpha\rangle \tag{7.24}$$

coupled equations for the expansion coefficients can be obtained

$$i\hbar\frac{\partial}{\partial t}c_\alpha(t) = \mathcal{E}_\alpha + \sum_{\alpha\beta}J_{\alpha\beta}(t)c_\beta(t) \tag{7.25}$$

with the matrix elements of the coupling Hamiltonian

$$J_{\alpha\beta}(t) = \langle\alpha|H_{QC}(t)|\beta\rangle = \sum_{m,n}c_m^\alpha c_n^\beta \langle m|H_{QC}(t)|n\rangle \ . \tag{7.26}$$

The population of the excitonic states, i.e., the probability to find the pigment system in that state is given by $P_\alpha(t) = \left|c_\alpha(t)\right|^2$. Also the probability to find an individual pigment in the excited state can be obtained

$$P_m(t) = \left|\langle m|\Psi_Q\rangle\right|^2 = \sum_\alpha c_m^\alpha c_\alpha(t) \tag{7.27}$$

Using these equations the electronic time-dependent Schrödinger equation for the pigment system can be solved numerically. The wave function describes a pure state of the system. To reproduce the true physical ensemble the wave packet propagation has to be performed on sufficient number of trajectories and averaged.

### 7.2.3. Temperature correction

As discussed above the wave packet description of the pigment system has the disadvantage that it does not include temperature effects but implies a high temperature assumption. Therefore the populations will reach an equal distribution in the long time limit. However, the correct equilibrium distribution is given by the

Boltzmann distribution

$$|c_\alpha^{eq}|^2 = \frac{e^{-\mathscr{E}_\alpha/k_B T}}{\sum_\alpha e^{-\mathscr{E}_\alpha/k_B T}} \tag{7.28}$$

To correct the temperature behavior we follow a method proposed by Bastida and co-workers [66–68]. In this method the couplings between quantum system and classical system are modified by a temperature-dependent quantum correction factor

$$J_{\alpha\beta}^{tc} = \left( \frac{2}{1 + e^{-\hbar\omega_{\alpha\beta}/k_B T}} \right)^{1/2} J_{\alpha\beta} . \tag{7.29}$$

This factor ensures that the correct equilibrium distribution is reached. Since the use of this factor destroys the symmetry of the coupling matrix $J_{\alpha\beta}^{tc} \neq J_{\beta\alpha}^{tc}$. In order to keep it, symmetrical, quantum corrected couplings are introduced as follows

$$J_{\alpha\beta}^{stc} = J_{\beta\alpha}^{stc} = |c_\beta| J_{\alpha\beta}^{tc} - |c_\alpha| J_{\beta\alpha}^{tc} , \quad \alpha > \beta .$$
$$J_{\alpha\beta}^{stc} = J_{\alpha\beta} . \tag{7.30}$$

This corrected coupling matrix is real and symmetric and thus the norm and the total energy of the wave function will be conserved. The non diagonal matrix elements vanish when the populations reach equilibrium, this can be proven by Eqs. 7.28, 7.29 and 7.30.

## 7.3. Two-state model system

As a first test for the above described method a molecular heterodimer is used. This system consists of two monomers with different excitation energies $\varepsilon_1$ and $\varepsilon_2$ and the coupling $V_{12} = V$. According to Eq. 7.22 the coupling to the environment is introduced by adding fluctuations to the excitation energies the influence on the

coupling is neglected. Thus the Hamiltonians for this system are

$$H_Q = \sum_{m=1}^{2} \varepsilon_m \ket{m}\bra{m} + V(\ket{1}\bra{2} + \ket{2}\bra{1}),$$ (7.31)

$$H_{QC} = \sum_{m=1}^{2} \Delta\varepsilon_m(t)\ket{m}\bra{m}.$$ (7.32)

The system Hamiltonian can be diagonalized to get the excitonic states $\ket{\alpha}$, energies $\mathscr{E}_\alpha$ and expansion coefficients $c_m^\alpha$. For a two level system this can be done analytically. The solution can be found in textbooks [8, 48], here just the excitonic energies are given

$$\mathscr{E}_{\alpha=\pm} = \frac{\varepsilon_1 + \varepsilon_2}{2} \pm \frac{1}{2}\sqrt{(\varepsilon_1 + \varepsilon_2)^2 + 4|V|^2}.$$ (7.33)

With that the time-dependent Schrödinger equation for the system including the coupling to the classical system can be written as

$$i\frac{\partial}{\partial t}\ket{\Psi_Q(t)} = (H_Q + H_{QC}(t))\ket{\Psi_Q(t)}$$
$$= \left(\sum_{\alpha} \mathscr{E}_\alpha \ket{\alpha}\bra{\alpha} + \sum_{\alpha\beta} J_{\alpha\beta}\ket{\alpha}\bra{\beta}\right)\ket{\Psi_Q(t)}.$$ (7.34)

This can be solved numerically using the expansion given in Eq. 7.25. The quantum correction for the temperature can be introduced by replacing the coupling matrix elements $J_{\alpha\beta}$ with the temperature-dependent coupling factors $J_{\alpha\beta}^{stc}$ given in Eq. 7.30.

As reference for this calculation results obtained by the reduced density matrix approach will be used. In this approach the system is split in a relevant system (here the electronic excitations) and a bath containing all other degrees of freedom. The key quantity is the reduced density matrix (RDM) which is the partial average of the total density matrix over the baths degrees of freedom. This method reproduces the correct temperature behavior and is therefore suited to check the functionality of the quantum correction for the wave packet (WP) description. In this method the coupling to the bath is characterized by the spectral density. To compare both approaches we need to calculate time trajectories of excitation en-

ergy fluctuations which correspond to a specific spectral density. The spectral density can be calculated from the autocorrelation function of the excitation energies $E_m(t) = \varepsilon_m + \Delta\varepsilon_m(t)$

$$C_m(t) = \langle \Delta\epsilon_m(t)\Delta\epsilon_m(0)\rangle \, . \tag{7.35}$$

With that the spectral density can be introduced as [153]

$$J(\omega) = \frac{2}{\pi\hbar} \tanh\left(\frac{\hbar\omega\beta}{2}\right) \int_0^\infty dt \, \cos(\omega t)C(t) \, . \tag{7.36}$$

For the RDM calculations performed here as comparison a Drude spectral density was used

$$J(\omega) = \frac{2\lambda}{\pi} \frac{\gamma\omega}{\gamma^2 + \omega^2} \, . \tag{7.37}$$

Using the high temperature approximation $\beta = 1/k_B T \ll 1$ the autocorrelation function has to have the form

$$C(t) = \frac{2\lambda}{\beta} e^{-\gamma t} \tag{7.38}$$

With the dissipation energy $\lambda$ and the autocorrelation time $1/\gamma$. To gain a trajectory for the excitation energy fluctuations $\Delta\varepsilon_m(t)$ a random generator which produces random numbers with a given autocorrelation can be used.

### 7.3.1. Results and discussion

For the model system energy difference between the two excitation energies was set to $\varepsilon_2 - \varepsilon_2 = 100\text{cm}^{-1}$and the coupling to $V = 100\text{cm}^{-1}$. For generating the fluctuations a correlation time of $1/\gamma = 100\text{fs}$ was used. The calculations were performed for two different reorganization of $\lambda = 50\text{cm}^{-1}$ and $\lambda = 100\text{cm}^{-1}$. The wave function was calculated for $10^5$ realizations and averaged. To find the sufficient number of realization a check for convergence was performed. The excitonic wave function was calculated by solving the differential equations 7.25. From the wave function the populations of single excited states were calculated according to
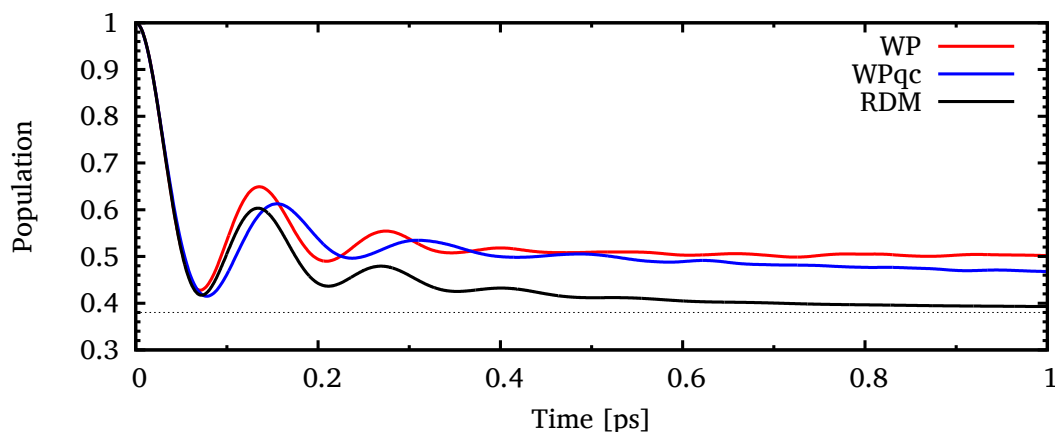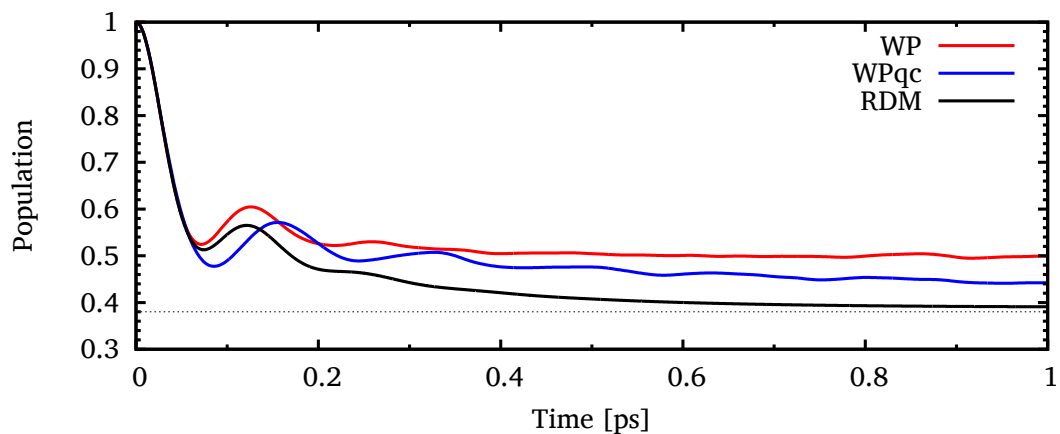
**Figure 7.2.:** Excitation dynamics calculated with wave packet approach (WP), WP with temperature correction (WPqc) and reduced density matrix (RDM) for reorganization energy of $\lambda = 50\text{cm}^{-1}$

Eq. 7.27. Figs. 7.2 and 7.4 show the time evolution of the population. Here, only the population of the monomer with the higher excitation energy is shown. The population of the other monomer is $P_2(t) = 1 - P_1(t)$ since the wave function is normalized. As can be seen from both plots, the populations obtained from the wave function and the RDM show the same oscillations also the dephasing time is equal. The only difference is that the populations obtained from the RDM converge to the thermal equilibrium, which is indicated by the dotted line in the figures. This is due to the reorganization energy which is removed from the system. The WP calculations do not include any energy dissipation and conserve the system energy over time. Therefore they imply a high temperature limit which leads to equal populated states in the long time limit, which is $P_m^{eq} = 0.5$ for the two-state system. The dephasing is determined by the correlation time $1/\gamma$ and equal in both methods. By increasing the reorganization energy, the system is expected to show a stronger damping, i.e., it reaches the equilibrium population faster, that can be seen in RDM calculations. The oscillations are due to the intermolecular coupling $V$ and therefore reproduced equal in both methods. If now the quantum correction is introduced to the WP calculations the populations are expected to also reach the equilibrium distribution. This is the case for the long time limit as can be seen in Figs. 7.3 and 7.5. Also the damping increases with higher reorganization energies. However, the time scale of the damping is different by a factor of approximately 10.
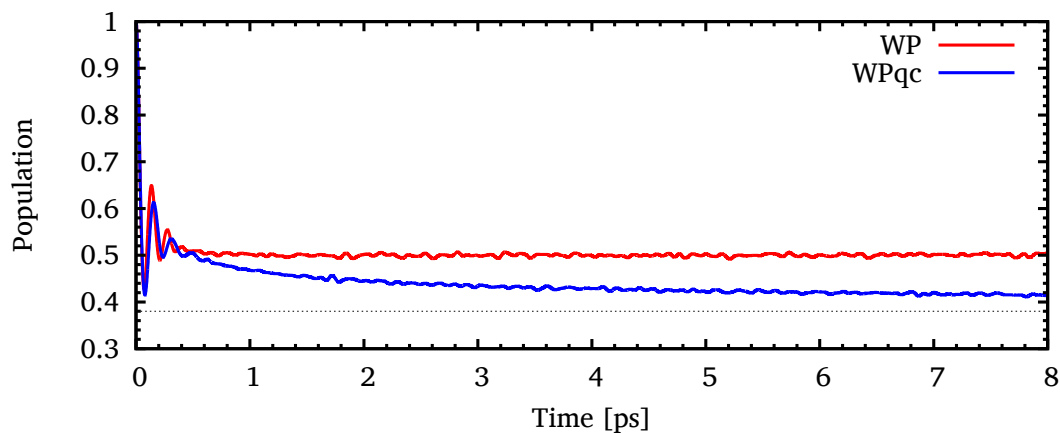
**Figure 7.3.:** Same as Fig. 7.2 but for a larger time scale. It can be seen, that using the temperature correction the correct thermal equilibrium population is reached in the long time limit.
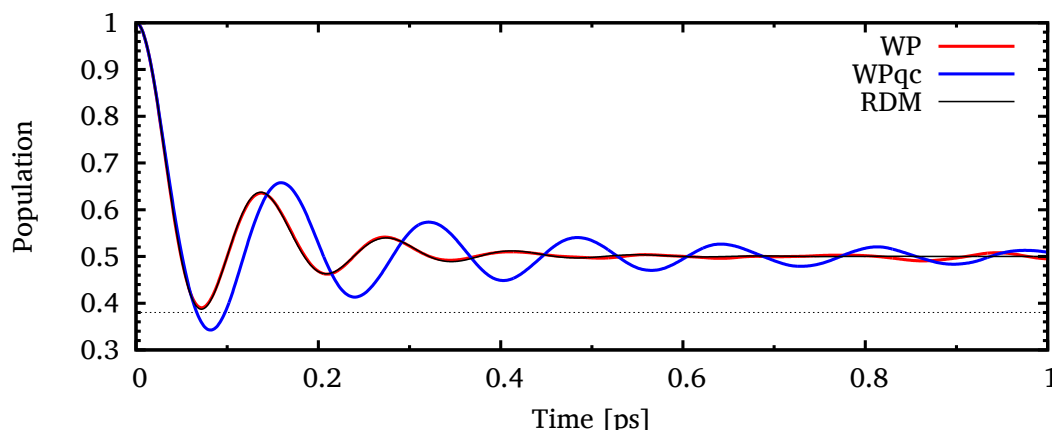


**Figure 7.4.:** Excitation dynamics calculated with wave packet approach (WP), WP with temperature correction (WPqc) and reduced density matrix (RDM) for reorganization energy of $\lambda = 100\text{cm}^{-1}$
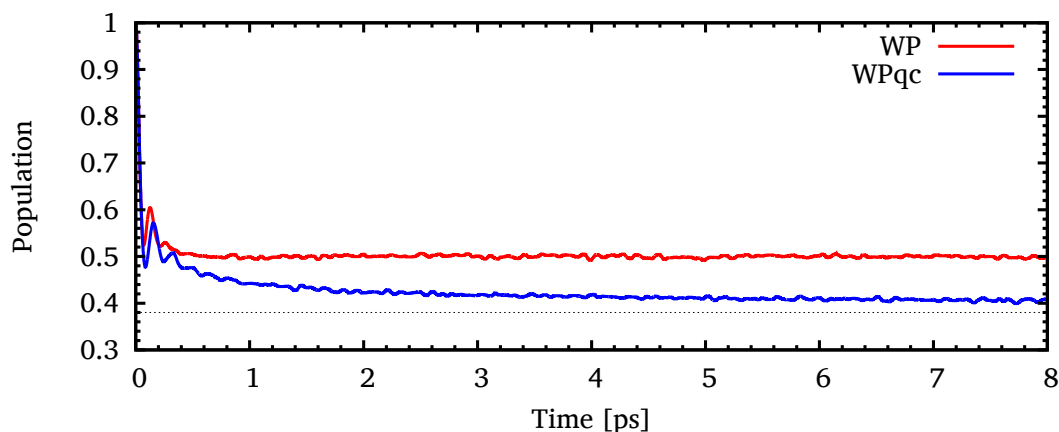
**Figure 7.5.:** Same as Fig. 7.2 but for a larger timescale. It can be seen, that using the temperature correction the correct thermal equilibrium populatian is reached in the long time limit.

The equilibrium is not reached exactly and after much longer time as in the RDM calculations. Another point is, that the peaks of the oscillations are shifted so that the oscillation frequency is lowered. Since the correction factor only changes the system-bath coupling and not the intermolecular coupling, this result is surprising. When the difference of the excitation energies is set to zero $\varepsilon_1 = \varepsilon_2$ the equilibrium distribution correspond to the high temperature limit and therefore WP and RDM calculations should give the same results. This is the case as can be seen in Fig. 7.6. The temperature-corrected WP calculations deviate also in this case from the other calculations. The quantum correction factor in Eq. 7.29 is equal to one when the excitation energies are equal ($\omega_{\alpha\beta} = 0$) an therefore the coupling factors are not changed. The only difference to the standard WP calculation is the symmetrization Eq. 7.30. This symmetrization changes the magnitude of the coupling factor and therefore the oscillation frequency.

Finally it can be concluded, that the ensemble averaged WP calculations and the RDM approach show excellent agreement in terms of the quantum coherent oscillations and their dephasing. The only disadvantage is that the correct thermal equilibrium is not achieved. In cases where the energy splitting in the system is low, e.g. $(\varepsilon_n - \varepsilon_m) \ll k_B T$ the results differ only marginal from the RDM results. The attempt to correct the WP calculations with a temperature dependent factor was not overall satisfying. On the one side the correct thermal equilibrium is reached

**Figure 7.6.:** Excitation dynamics calculated with wave packet approach (WP), WP with temperature correction (WPqc) and reduced density matrix (RDM) for reorganization energy of $\lambda = 50\text{cm}^{-1}$ and equal excitation energies.

but the time scale for this relaxation process is not reproduced correctly. Another disadvantage is the frequency of the coherent quantum oscillations is influenced by the symmetrization procedure. Therefore the application of this correction method to the here investigated system has to be put into question. It my be useful to check how temperature influences affect the system dynamics but it is not capable to describe them correctly. However the wave packet calculations are valuable tool for the hybrid quantum classical description of energy transfer processes in large molecular systems. The advantage over the other methods like RDM calculations is that the time-dependent Hamiltonian can be used directly. In the RDM approach all quantities of the classical system have to be included in the spectral density. This is in most cases related to averaging processes which may lead to the loss of information. For simple systems like the here investigated two-level system this is no drawback but for the combination with MD simulations of complex systems the wave packet method is easier to apply. Also the influence of the environment on the intermolecular coupling is straight forward to include by using time-dependet couplings gained from the MD simulations. Although the WP calculations have to be performed for a sufficient number of trajectories to achieve the correct ensemble average they are computationally cheap. This is because only a small system of coupled linear differential equations has to be solved.
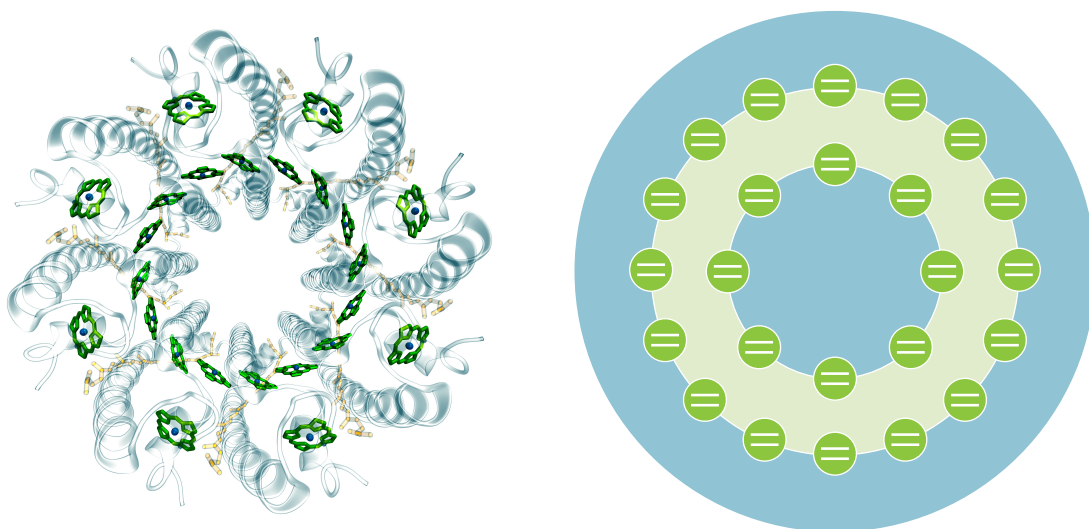
**Figure 7.7.: Left:** LH2 complex of *Rs. molischianum*, top view. The protein structure is blue colored and the BChls are shown in green. **Right:** Model system of the LH2 complex. The complex contains two rings of bacterio chlorophyl embedded in a protein matrix. The B850 ring contains 16 and the B800 ring 8 pigments. The model system consists of 24 two level systems (green) coupled by Coulomb interaction (light green). This system is coupled to a classical environment representing the protein matrix (blue).

## 7.4. Excitation energy transfer in LH2 of purple bacteria

In this part the hybrid quantum classical approach described above is applied to the light harvesting system II (LH2) of the purple bacterium *Rhodospirillum (Rs.) molischianum*. This LH complex, as depicted in Fig. 7.7, consists of two rings with 16 and 8 pigment molecules named bacteriochlorophyll a (BChl a). These two rings with eightfold symmetry are named B850 and B800 based on their respective absorption maxima at 850 nm and 800 nm. The model for this complex is depicted in the right hand side of Fig. 7.7. It consists of 24 coupled excitation states representing the BChls. The influence of the protein environment on the excitation energies and the couplings was included via a coupling operator containing the fluctuations of these values. The time-dependent Hamiltonian for this system was determined from MD simulations based on the crystal structure of *Rs. molishianum* (PDB:1LGH) [158]. From the MD trajectories the excitation energies and electronic couplings where

calculated with the ZINDO/S approach [155, 156, 159] and the method of transition charges from electrostatic potentials (TrEsp) [160, 161], respectively. Details on these calculations and the determined values of the time-dependent Hamiltonian can be found in our publication [59] which is attached in appendix B. Using this Hamiltonian the time-dependent Schrödinger equation for this system was solved numerically according to equation 7.25. From these results the time-dependent populations, i.e., the probability of excitation for the individual BChls were determined by Eq 7.27. The averaging over the fluctuations was achieved by propagating the wave function for multiple starting points along the MD trajectory and a subsequent averaging. The time-dependent Hamiltonian had a total length of 180 ps and the excitonic wave function was calculated for a time range of 250 fs. By shifting the starting time in steps of 100 fs 1800 realizations could be averaged to achieve a proper ensemble average. The shift of 100 fs was used because after a time of approximately 50 fs the temporal correlations of the excitation energies are negligible. Initially, one BChl was excited and the decay of its population was tracked. This calculation was repeated for every BChl in the complex. The results are shown in Fig. 7.8. The decay rates of the excitation differs strongly between the BChls belonging to the B850 and the B800 ring respectively. This is due to the weaker intermolecular coupling between the BChls in the B800 ring. In the B850 ring 50% of the excitation remains localized on BChl for about 20 fs while for the B800 ring this process takes between 50 fs and 200 fs. In both rings there are two BChls which exhibit a slower decay as the average. These BChls have an average excitation energy which is slightly higher than the average excitation energy of the BChls in the respective ring. In the longtime limit the population converges to an equal distribution over all BChls which is $P^{eq} = 1/24 = 0.042$. The excitation probability for the next neighboring BChls of the initial excited is shown in Fig. 7.9. Here also the difference between the both rings is obvious. In the B850 ring the excitation dynamics show a coherent wave-like behavior which is not destroyed by the ensemble averaging. The complete dephasing of these oscillations occurs at around 100 fs. In the B800 ring these oscillations are not present due to the weaker coupling between the BChls.
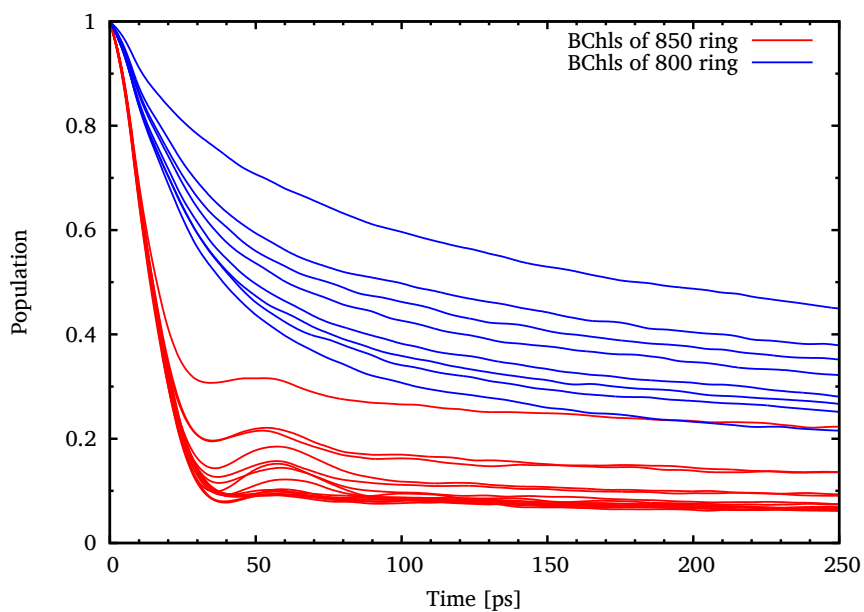
**Figure 7.8.:** Excitation dynamics of the BChls in LH2. Shown is the population decay from the respective initially excited BChl.
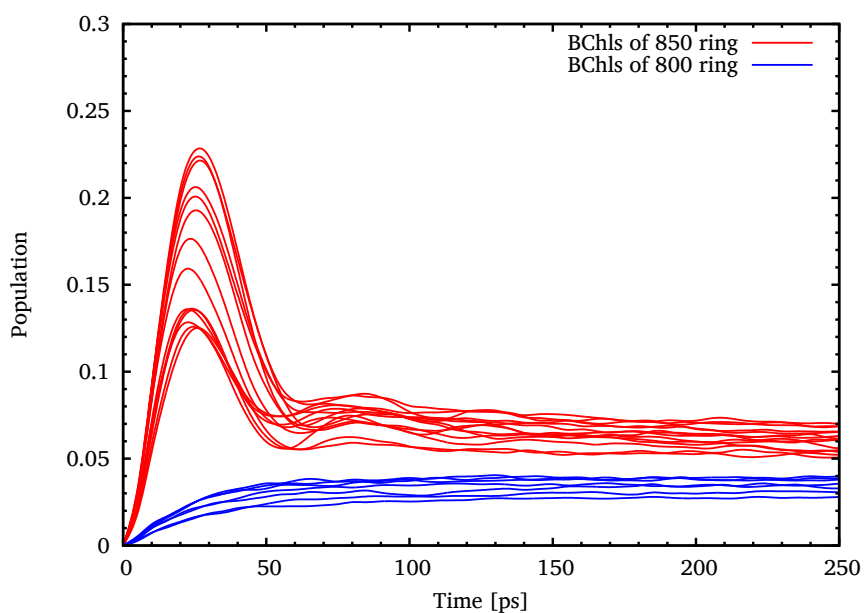


**Figure 7.9.:** Excitation dynamics of the BChls in LH2. Shown is the population of BChl next to the initially excited BChl.

119

# 8. Summary

In this thesis wave packet dynamics occurring in various molecular systems were investigated. This included the simulations of nuclear wave packet dynamics in different electronic states of diatomic molecules initiated by femtosecond laser pulses. A theoretical description of non-resonant multi-photon excitations has been given, which allows to study the wave packet dynamics initiated by such processes in the time domain. Furthermore the excitation energy transfer in pigment complexes was investigated by a hybrid quantum classical approach. Therefore the electronic excitations were described by a excitonic wave packet propagating in a quantum system coupled to an classical environment.

In the first part, simulations of fully time-resolved pump degenerate four-wave mixing (pump-DFWM) experiments, which enable the investigation of molecular dynamics in high-lying electronic states, were performed. These experiments were carried out on well investigated diatomic molecules. The potential energy surfaces for these molecules could be calculated from high resolution spectroscopic data using the Rydberg-Rees-Klein method. With these potential energy surfaces model systems containing the relevant electronic states were constructed. To simulate the excitation process which involved the non-linear interaction of three laser pulses the time-dependent Schrödinger equation for the nuclear motion was solved numerically. This was done using perturbation theory for full time-resolved pump-DFWM experiments on iodine and exactly for time coincident DFWM experiments on molecular Bromine. From the resulting wave function time and frequency-resolved spectra were calculated and compared to the experiments. This allowed for a detailed analysis of the experimental spectra.

For the iodine molecule a model system containing the ground, first excited state, and one ion-pair state was used. The experiments intended to investigate the molecular dynamics in ion-pair states belonging to two different tiers. To check

whether it is possible to monitor dynamics of a specific ion pair state by carefully selecting the right wavelength for the DFWM beams, simulations were performed which included only this specific ion pair state. Comparing the experimental and theoretical results, good agreement could be found. The contributions of the ion-pair state in the measured signals could be identified. Which confirmed that time-resolved pump-DFWM spectroscopy is suitable tool for the investigation of molecular dynamics in high-lying electronic states.

As a further system molecular bromine was investigated. For this molecule also high resolution spectroscopic data was available which allowed for the calculation of exact potential energy surfaces. The first experiment which was analyzed by performing a simulation was a pump-DFWM experiment with coincident laser pulses where the dynamics of the excited $B$ state were monitored. Different vibrational energy spacing were observed for different DFWM wavelengths of 310 nm and 300 nm with a fixed initial pump wavelength of 540 nm in both cases. For a DFWM wavelength of 310 nm, the observed spacings agreed well with the frequency domain data. However, for a DFWM wavelength of 300 nm, a smaller vibrational energy spacing was found. The theoretical analysis showed that the different spacings observed are attributed to the contribution of the first hot vibrational state in the electronic ground state. Here the DFWM signal was calculated from an exact propagation of the nuclear wave function. The experimental and theoretical signals were recorded time and frequency-resolved resulting in spectroscopic maps showing the dynamics for different detection wave lengths. The agreement between the experiment and the theoretical results showed good agreement.

The investigations on bromine were extended to a fully time-resolved pump-DFWM scheme similar to the iodine experiments. The spectroscopic signals were calculated using perturbation theory and compared to the experiments. Also here the signals were recorded time and frequency-resolved. It was possible to examine the ion-pair state dynamics in detail by considering only transients at particular detection wavelengths. By comparing experiment and simulation the features in the experimentally measured spectra could be assigned to excited state and ion-pair state contributions.

Femtosecond spectroscopy can also be performed using non-resonant transitions like non-resonant multi-photon (NMT) excitation. To gain information about dy-

namical processes occurring during such excitations a theoretical description in the time-domain is necessary. Therefore projection operator theories have been applied to study NMT processes in molecular systems. These allowed for the formulation of effective time-dependent Schrödinger equations. The effective Schrödinger equations were further simplified by invoking the slowly varying envelope approximations and rotating wave approximations. The validity of these approximations was numerically verified which was only possible due to the equations derived from a time local approach. The derived formalism was applied to a sequence of 2-photon and 3-photon transitions. It was shown that for such a sequence of events certain prerequisites of the pulse have to be fulfilled.

In the last part an ensemble averaged wave packet approach for the simulation of excitation energy transfer (EET) in complex biological systems was investigated. Therefore, a mixed quantum classical description was used. First a model system for the electronic excitation Hamiltonian for pigment systems coupled to a classical environment was deduced. The approach was tested on an artificial model system of a molecular heterodimer and compared to reduced density matrix (RDM) calculations. It could be shown that the wave packet dynamics (WP), which are the ensemble average of pure state dynamics, give the same results as the RDM calculations based on the statistical operator. Only the relaxation to the correct thermal equilibrium is not reproduced by the WP calculation. The application of a quantum correction for the proper temperature behaviour, proposed by Bastida and co-workers [67] was tested. With this correction the WP calculation equilibrate to the correct thermal distribution but the time scale of the relaxation process was not reproduced correctly. Also the intermolecular couplings were influenced by this correction which resulted in an deviation of the coherent quantum oscillations and their dephasing. This leads to the conclusion that the temperature correction in this form is improper for the description of EET processes and needs further modifications.

The ensemble averaged WP description of excitons was then used to model the EET in light harvesting system II (LH2) of purple bacteria. This complex contains two rings of pigments named B850 and B800 after their main absorption wave length. The B850 and B800 rings contain 16 and 8 pigments respectively. As model system a time-dependent Hamiltonian obtained by electronic structure calculations from classical molecular dynamics (MD) simulations was used. The temporal energy

fluctuations in this Hamiltonian were used to model the influence of the protein environment on the EET process in the pigment system of this complex. The energy transfer dynamics for individual pigments (bacteriochlorophyls) in this complex were calculated and analyzed. For the B850 ring where the pigments are stronger coupled coherent wave-like excitation dynamics could be observed. These oscillations dephased after 100 fs. In the B800 ring such beaviour could not be found due to the weaker electronic coupling of the pigments.

# A. Non-resonant multi photon transition

## A.1. Perturbational Description of Non–Resonant Transitions

To have a reference case at hand we shortly recall the perturbative description of a non–resonant two–photon transition. It should proceed from the electronic ground-state $\varphi_g$ to some electronic excited state $\varphi_e$ without intermediate states. In order to account for such transitions, we have to solve the respective time-dependent Schrödinger equation 6.6 with the initial condition $|\Psi_0\rangle = |\varphi_g\rangle |\chi_g^{(0)}\rangle$ (in most cases we have in mind $\chi_g^{(0)} = \chi_{gM=0}$). The expansion of the state vector in Eq. 6.6 with respect to the electron–vibrational basis introduced in Section 6.2 reads

$$|\Psi(t)\rangle = \sum_{a,M} C_{aM}(t) |\Psi_{aM}\rangle \; . \tag{A.1}$$

Those expansion coefficients which refer to the excited electron–vibrational states $\Psi_{eM}$, i.e. the quantities

$$C_{eM}(t) = e^{-i\omega_{eM}(t-t_0)} \langle \Psi_{eM} | S(t, t_0; \mathbf{E}) | \Psi_{g0} \rangle \; , \tag{A.2}$$

should display whether or not the non–resonant two–photon transition led to an excited state population. And, the time–dependence of the coefficients should display the vibrational wave packet dynamics induced by this transition.

As is well known the second-order contribution from the $S$-matrix expansion describes two-photon transitions. The respective matrix elements read (note the re-

placement of the initial vibrational state $\chi_{g0}$ by the more general one $\chi_{gN}$ leading to $\Psi_{gN}$, and the the use of the interaction representation for the dipole operators)

$$
\langle \Psi_{eM} | S^{(2)}(t, t_0; \mathbf{E}) | \Psi_{gN} \rangle = -\frac{1}{\hbar^2} \int_{t_0}^{t} d\tau_1 \int_{t_0}^{\tau_1} d\tau_2
$$
$$
\times \langle \Psi_{eM} | [\mathbf{E}(\tau_1)\hat{\mu}(\tau_1)][\mathbf{E}(\tau_2)\hat{\mu}(\tau_2)] | \Psi_{gN} \rangle . \quad \text{(A.3)}
$$

Let us calculate this expression for the case of a cw-excitation, i.e. in the frequency domain. Of course, the field-strength has to be weak enough to guarantee the validity of the used approximation, i.e. $|C_{eM}(t)|^2 \ll 1$ should be fulfilled for all considered times. In the limit $t_0 \to -\infty$ one obtains for the expansion coefficients of the excited electronic state (note the replacement of $\mathbf{E}(t)$ by the resonant contribution $\sim \exp(-i\omega t)$)

$$
C_{eM}(t) = -e^{-i\omega_{eM}(t-t_0)-i2\omega t_0} \frac{E^2}{\hbar^2} \sum_{xK} \frac{d(eM, xK)d(xK, gN)}{\omega_{xK} - \omega_{gN} - \omega}
$$
$$
\times \left( \frac{1}{\omega_{eM} - \omega_{gN} - 2\omega + i\epsilon} - \frac{1}{\omega_{eM} - \omega_{xK} - \omega + i\epsilon} \right) .
$$
$$
\text{(A.4)}
$$

$E$ denotes the constant field envelope. The unity vector $\mathbf{n}$ of field polarization has been multiplied with the dipole operator to give scalar dipole transition matrix elements $d(aM, bN) = \langle \Psi_{aM} | \mathbf{n}\hat{\mu} | \Psi_{bN} \rangle$. The states $\varphi_x$ used for the expansion are understood to be positioned energetically far away from the excited state $\varphi_e$.

In order to achieve a proper understanding of both terms in Eq. A.4 let us assume for a moment that all levels $\varphi_x$ are condensed into a single one denoted by $\varphi_i$ (with energy $\hbar\omega_i$) and positioned in between the ground and the excited state. Then, the second term in Eq. A.4 is easily identified as describing the stepwise transition from $\varphi_g$ to $\varphi_i$, and afterwards from $\varphi_i$ to $\varphi_e$, both steps in a single photon absorption process. In contrast, the first term in Eq. A.4 is responsible for a direct transition from $\varphi_g$ to $\varphi_e$ without intermediate states, and gives a resonant contribution independent on the position of $\varphi_i$ in relation to $\varphi_g$ and $\varphi_e$.

Let us move $\varphi_i$ energetically far above $\varphi_e$. Then the first term of Eq. A.4 decreases in $1/\omega_i$ and the second in $1/\omega_i^2$. Hence, the first term strongly dominates over the second one, which will be neglected in the following.

If the single state $\varphi_i$ is replaced by the manifold of electron-vibrational states belonging to the off-resonant electronic states $\varphi_x$, then there is a chance that the smallness of the expansion coefficients, Eq. A.4 can be compensated for by a summation with respect to the off-resonant state-manifold. In order to see this we assume that the non-resonant states form a dense continuum characterized by the density of states

$$\varrho(\Omega) = \sum_{x,K} \delta(\Omega - \omega_{xK}) . \tag{A.5}$$

With it, the expansion coefficients (note the neglect of the second term of Eq. A.4) yields

$$C_{eM}(t) = -\frac{e^{-i\omega_{eM}(t-t_0)-i2\omega t_0}}{\omega_{eM} - \omega_{gN} - 2\omega + i\epsilon} \frac{E^2}{\hbar^2} \int d\Omega \, \varrho(\Omega) \frac{d(eM,\Omega)d(\Omega,gN)}{\Omega - \omega_{gN} - \omega} , \tag{A.6}$$

where $d(eM,\Omega)$ and $d(\Omega,gN)$ denote frequency dependent (transition) dipole operator matrix elements. The expression indicates that the efficiency of the non-resonant two-photon transition (that is, the population $\mid C_{eM}(t) \mid^2$ of the excited electron-vibrational state) is essentially determined by the $\Omega$-integral. It represents a summation with respect to all off–resonant single photon transitions from the initial state with energy $\hbar\omega_{gN}$ into the non–resonant states with energy $\hbar\Omega$. Only the complete summation of all these non–resonant contributions may lead to a sufficiently large two–photon transition amplitude. As is obvious from Eq. A.6 the $\Omega$–integral can be seen as an effective two–photon transition matrix element coupling to the *square* of the field strength.

## A.2. Time Non–Local Terms and the RWA

Based on the expansion, Eq. 6.49 of the vibrational wave functions and the total time–dependent Schrödinger equation we present in the following a possible sim-

plification of the two–photon and three–photon term in Eq. 6.33 what will be done separately for both contributions. Afterwards the RWA is introduced

## A.2.1. The Two–Photon Term

We consider the time non–local term of Eq. 6.33 being proportional to $\mathbf{D}_{ab}^{(2)}$. Noting Eq. 6.5 for the field–strength and the expansion Eq. 6.49, as well as $D_{ab}^{(2)} = \mathbf{D}_{ab}^{(2)}\mathbf{nn}$ we introduce

$$-\sum_b \int_{t_0}^{t} d\bar{t} \, \mathbf{D}_{ab}^{(2)}(t - \bar{t})\mathbf{E}(t)\mathbf{E}(\bar{t})\chi_b(\bar{t}) = -\sum_n e^{-in\omega t}\tilde{\Gamma}_a^{(2)}(n; t), \qquad (A.7)$$

with

$$\tilde{\Gamma}_a^{(2)}(n; t) = -\sum_b \int_{t_0}^{t} d\bar{t} \, D_{ab}^{(2)}(t - \bar{t})e^{in\omega t}$$

$$\times [E(t)e^{-i\omega t} + E^*(t)e^{i\omega t}][E(\bar{t})e^{-i\omega\bar{t}} + E^*(\bar{t})e^{i\omega\bar{t}}]e^{-in\omega\bar{t}}\chi_b(n; \bar{t}) \qquad (A.8)$$

Note also the introduction of factors oscillating with $\exp(\pm in\omega t)$. Then, all terms are arranged in such a way that they have the common prefactor $\exp(-in\omega t)$. This requires to move in part from $\chi_b(n; \bar{t})$ to $\chi_b(n \pm 2; \bar{t})$. The newly arranged terms are collected now by $\Gamma_a^{(2)}$ instead of $\tilde{\Gamma}_a^{(2)}$. The introduction of the difference time $\tau = t - \bar{t}$ finally yields

$$\Gamma_a^{(2)}(n; t) = -\sum_b \int_{0}^{t-t_0} d\tau \, D_{ab}^{(2)}(\tau)\Big(E(t)E(t - \tau)e^{i(n-1)\omega\tau}\chi_b(n - 2; t - \tau)$$

$$+ E(t)E^*(t - \tau)e^{i(n-1)\omega\tau}\chi_b(n; t - \tau) + E^*(t)E(t - \tau)e^{i(n+1)\omega\tau}\chi_b(n; t - \tau)$$

$$+ E^*(t)E^*(t - \tau)e^{i(n+1)\omega\tau}\chi_b(n + 2; t - \tau)\Big). \qquad (A.9)$$

### A.2.2. The Three–Photon Term

The three–photon term of Eq. 6.33 is reformulated in the same way as the two–photon one in the foregoing section We introduce $D_{ab}^{(3)} = \mathbf{D}_{ab}^{(3)}\mathbf{nnn}$ and may write in a first step

$$
-\sum_b \int_{t_0}^t d\bar{t} \int_{\bar{t}}^t dt_1\, \mathbf{D}_{ab}^{(3)}(t, t_1, \bar{t})\mathbf{E}(t)\mathbf{E}(t_1)\mathbf{E}(\bar{t})\chi_b(\bar{t}) = -\sum_n e^{-in\omega t}\tilde{\Gamma}_a^{(3)}(n; t)\,,
$$

(A.10)

with

$$
\tilde{\Gamma}_a^{(3)}(n; t) = -\sum_b \int_{t_0}^t d\bar{t} \int_{\bar{t}}^t dt_1\, D_{ab}^{(3)}(t, t_1, \bar{t})e^{in\omega t}[E(t)e^{-i\omega t} + E^*(t)e^{i\omega t}]
$$

$$
\times [E(t_1)e^{-i\omega t_1} + E^*(t_1)e^{i\omega t_1}][E(\bar{t})e^{-i\omega \bar{t}} + E^*(\bar{t})e^{i\omega \bar{t}}]e^{-in\omega \bar{t}}\chi_b(n; \bar{t})\,. \text{ (A.11)}
$$

We change to new time–arguments $t - \bar{t} = \tau$ and $t_1 - \bar{t} = \bar{\tau}$ and also change the index $n$ to have for all terms a common prefactor $\exp(-in\omega t)$ (note the replacement of $\tilde{\Gamma}_a^{(3)}$ by $\Gamma_a^{(3)}$). It results in

$$
\Gamma_a^{(3)}(n; t) = -\sum_b \int_0^{t-t_0} d\tau \int_0^{\tau} d\bar{\tau}\, D_{ab}^{(3)}(\tau - \bar{\tau}, \bar{\tau})
$$

$$
\times [E(t)E(t - (\tau - \bar{\tau}))E(t - \tau)e^{-i\omega\bar{\tau}+i(n-1)\omega\tau}\chi_b(n - 3; t - \tau)
$$

$$
+E(t)E^*(t - (\tau - \bar{\tau}))E(t - \tau)e^{i\omega\bar{\tau}+i(n-1)\omega\tau}\chi_b(n - 1; t - \tau)
$$

$$
+E^*(t)E(t - (\tau - \bar{\tau}))E(t - \tau)e^{-i\omega\bar{\tau}+i(n+1)\omega\tau}\chi_b(n - 1; t - \tau)
$$

$$
+E^*(t)E^*(t - (\tau - \bar{\tau}))E(t - \tau)e^{i\omega\bar{\tau}+i(n+1)\omega\tau}\chi_b(n + 1; t - \tau)
$$

$$
+E(t)E(t - (\tau - \bar{\tau}))E^*(t - \tau)e^{-i\omega\bar{\tau}+i(n-1)\omega\tau}\chi_b(n - 1; t - \tau)
$$

$$
+E(t)E^*(t - (\tau - \bar{\tau}))E^*(t - \tau)e^{i\omega\bar{\tau}+i(n-1)\omega\tau}\chi_b(n + 1; t - \tau)
$$

$$
+E^*(t)E(t - (\tau - \bar{\tau}))E^*(t - \tau)e^{-i\omega\bar{\tau}+i(n+1)\omega\tau}\chi_b(n + 1; t - \tau)
$$

$$
+E^*(t)E^*(t - (\tau - \bar{\tau}))E^*(t - \tau)e^{i\omega\bar{\tau}+i(n+1)\omega\tau}\chi_b(n + 3; t - \tau)]\,. \quad \text{(A.12)}
$$

## A.3. Sequence of Three–Photon and Two–Photon Transitions

Next the reverse sequence of processes compared with that of the preceding section are considered, i.e. a three–photon transition into the first excited state followed by a two–photon transition into the higher excited state. Therefore, beside $\chi_g(t)$ we have to consider $\chi_e(t)$, and $\chi_f(t)$. The coupled Schrödinger equations read:

$$i\hbar\frac{\partial}{\partial t}\chi_g(t) = H_g\chi_g(t) - d^{(3)}E^{*3}(t)\chi_e(t)\,, \tag{A.13}$$

$$
\begin{aligned}
i\hbar\frac{\partial}{\partial t}\chi_e(t) = {} & \left(H_e - 3\hbar\omega - 2d^{(2)}|E(t)|^2\right)\chi_e(t) \\
& - d^{(3)}E^3(t)\chi_g(t) - d^{(2)}E^{*2}(t)\chi_f(t)\,,
\end{aligned}
\tag{A.14}
$$

and

$$
\begin{aligned}
i\hbar\frac{\partial}{\partial t}\chi_f(t) = {} & \left(H_f - 5\hbar\omega - 2d^{(2)}|E(t)|^2\right)\chi_f(t) \\
& - d^{(2)}E^2(t)\chi_e(t)\,.
\end{aligned}
\tag{A.15}
$$

# B. Modeling of light-harvesting in purple bacteria using a time-dependent Hamiltonian approach

**B.1.** Phys. Status Solidi B **248** 393 (2011)

# Modeling of light-harvesting in purple bacteria using a time-dependent Hamiltonian approach

**Carsten Olbrich, Jörg Liebers, and Ulrich Kleinekathöfer***

School of Engineering and Science, Jacobs University Bremen, Campus Ring 1, 28759 Bremen, Germany

* Corresponding author: e-mail u.kleinekathoefer@jacobs-university.de, Phone: +49-421-200-3523, Fax: +49-421-200-493523

The photosynthetic light-harvesting system II (LH2) of *Rhodospirillum molischianum* is investigated using a time-dependent combination of molecular dynamics simulations and semiempirical ZINDO/S electronic structure calculations. The classical simulations are performed on the available crystal structure of the LH2 complex. Snapshots of the atomic fluctuations along this 12 ps long trajectory serve as input for the calculation of the excitation energies of the individual

bacteriochlorophylls embedded in the LH2 complex. Furthermore, the couplings between the bacteriochlorophylls are computed using the method of transition charges from electrostatic potentials and for comparison also using the point-dipole approximation. With these quantities the excitonic energies of the complete system as well as the linear absorption spectra are calculated and compared to experimental findings.

**1 Introduction** Since photosynthesis is one of the most important biological processes on earth, it has been at the focus of many investigations. Many details of the molecular properties have been unraveled by a combination of experimental and theoretical studies [1–5]. Optical spectra have been investigated in experiment and theory especially also for the light-harvesting (LH) systems of purple bacteria [2, 6, 7]. In the last decades several high resolution crystal structures became available and opened the opportunity to study the structure–function relationship in atomic detail [6, 8–15]. Here, the light-harvesting system II (LH2) system of *Rhodospirillum (Rs.) molischianum* is in the focus of interest. This LH complex, as depicted in Fig. 1, consists of two rings with 16 and 8 bacteriochlorophyll a (BChl a) molecules, respectively. These two rings with eightfold symmetry are named B850 and B800 based on their respective absorption maxima at 850 and 800 nm. The difference in the absorption profile of the two rings is on the one hand caused by the strong coupling of the BChls in the B850 ring [35] and on the other hand by unlike environments around the chromophores. For the B800 ring its surrounding is hydrophilic while for the B850 ring it is rather hydrophobic [17]. In addition to the 24 BChls eight light-absorbing carotenoids are embedded into the protein matrix of the LH complex.

Classical molecular dynamics (MD) simulations provide an insight into the ground state properties of molecular complexes especially into their conformational changes. In order to describe optical properties one needs to apply quantum calculations providing the site energies of the system. Because of the size of the BChls these are often treated on a semiempirical level using, e.g., the ZINDO/S approach [18–20]. Over the last years this technique became rather popular and was applied to LH complexes [10–12, 15, 21–26] and other systems as well, e.g., Refs. [27–29]. Due to its low computational costs compared to *ab initio* methods, the semiempirical ZINDO/S method is quite suitable for performing excited state calculations along MD trajectories [24, 28, 29]. This in turn allows to determine the so-called spectral density. This spectral density can be used to calculate optical spectra, excitation energy transfer (EET) dynamics, and similar properties [9, 15, 24].

Another quantity which is necessary to describe electronic properties of the LH system are the electronic couplings between the individual sites (see, e.g., the review in Ref. [30]). Often it is assumed that for EET the coupling is dominated by the Coulomb interaction. A quite commonly used approach to that is the point-dipole approximation (PDA) which is known to be problematic at short distances

133
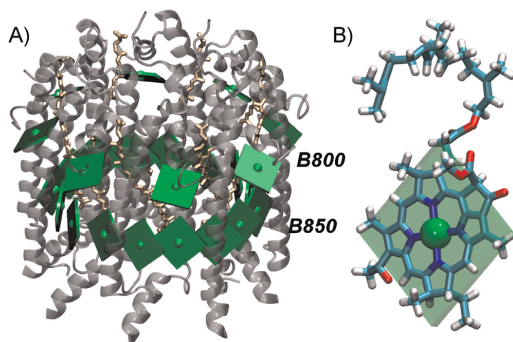
**Figure 1** (online color at: www.pss-b.com) Panel A: LH2 complex of *Rs. molishianum*. In gray, the protein structure is shown while the carotenoids are depicted in light yellow. Furthermore, the BChl molecules are represented as green squares with the central Mg atom as a sphere. Panel B: A green square as used in panel A overlaying a single BChl a molecule. (Figure rendered using VMD [16].)

[27, 31–33]. Alternatively, one can calculate the interaction energy by a supermolecule approach of two chromophores [10, 25]. Another accurate but numerically expensive techniques which calculates the Coulomb interaction in an *ab initio* manner is the transition density cube method [34]. Renger and co-workers developed the method of transition charges from electrostatic potentials (TrEsp) [32, 35]. In this approach, atomic centered partial transition charges are fitted to the electrostatic potential of the transition density belonging to the corresponding molecule. A simplification of that method is the so-called extended dipole method [27, 32]. In this case two charges, representing the dipole, are fitted to reproduce the transition charge density distribution. To account for a solvent screening effect on the couplings one can either use a constant factor [35] or, in an alternative approach, a distance-dependent correction developed by Scholes and co-workers [33, 36]. In a subsequent step, one can combine the obtained energies and couplings to construct a time-dependent Hamiltonian. This Hamiltonian can be used to evaluate optical properties and transfer rates from wave packet calculation directly [37–40] or using alternative approaches [15].

The present contribution starts with a description of the MD simulations before a semiempirical electronic structure methods for the ground and excited state energy calculations is detailed. A comparison is furthermore performed for the electronic couplings between the individual pigments. Preceding the conclusions, a time-dependent Hamiltonian is constructed to determine the time evolution of the electronic states and dipole strengths as well as the average linear absorption spectrum of the LH2 system under investigation.
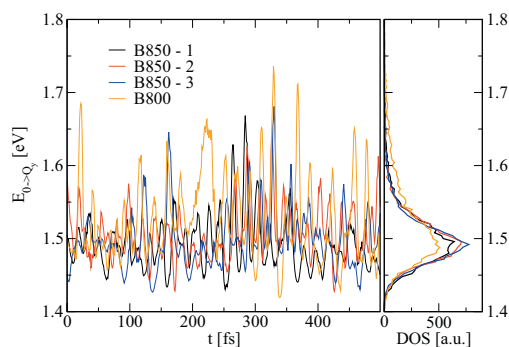
**2 Molecular dynamics simulations** The MD simulations are based on the crystal structure of *Rs. molishianum*

(PDB:1LGH) [17]. After adding the missing hydrogen atoms, the pigment–protein complex was embedded into a POPC lipid bilayer with about 30 Å of water on both sides. To neutralize the system, 16 Cl$^-$ ions were added to the bulk water. In total the system contained about 114,000 atoms with a dimension of $115 \times 115 \times 96$ Å$^3$. The simulations were carried out using the NAMD program package [41] with the CHARMM27 force field parameter for lipids, protein and the TIP3P water model. The same parameters as reported in [9] were employed for BChls and lycopenes.

Subsequent to an energy minimization the system was equilibrated in several steps at room temperature (300 K) and normal pressure (1 atm) in a NpT ensemble using periodic boundary conditions, the particle mesh Ewald method and a 2 fs time step using the SHAKE algorithm. In a first step, only the lipid tails were equilibrated for 2 ns while everything else was kept fixed. In the next step the constraints were limited to the LH2 complex for another 4 ns followed by a 2 ns equilibration without constrains. Finally a 12 ps production run with a time step of 1 fs was carried out. The atomic coordinates were recorded at every time step, resulting in 12,000 snapshots which were subsequently used in the QM calculations.

**3 Quantum chemistry calculations** Based on the MD simulations, we used the ORCA code (University Bonn, Germany) [42] in order to calculate the site energies for all 24 BChls in the complex at each of the 12,000 snapshots. So in total 288,000 single-point calculations were performed. Due to the large number of calculations to be performed and because the optical properties of BChls are determined by the cyclic conjugated $\pi$-electron system, we restricted the quantum system to a truncated structure of the BChl molecule. Each terminal CH$_3$ and CH$_2$CH$_3$ group as well as the pythyl tail were replaced by H atoms. Such truncation schemes have been employed previously [21, 24, 43]. Because of its accuracy [44] and the low computational cost we used the semiempirical ZINDO/S-CIS(10,10) method using the 10 highest occupied and the 10 lowest unoccupied states. This technique was also used in Refs. [24, 28, 29] for similar systems. To account for the effect of the surrounding environment, point charges from the MD simulations, from within a cutoff radius of 20 Å around the truncated BChl molecule, were included in the ZINDO/S-CIS calculations. The energy gap between the ground and the first excited, i.e., the $Q_y$, state and the corresponding density of state (DOS) is shown in Fig. 2 for several individual BChls. In this figure, the coupling between the BChls is neglected. Clearly a fluctuation of the energy gap around an average value is visible.

**4 Electronic coupling** In order to be able to construct the time-dependent Hamiltonian, one needs the coupling between the individual BChls in addition to the site energies. As already mentioned in Section 1, there exists several approaches to calculate the EET coupling. For purple bacteria a wide range of values were reported and a recent overview is, for example, given in Ref. [2].

B.1. Phys. Status Solidi B 248 393 (2011)

Original

Paper

Phys. Status Solidi B **248**, No. 2 (2011)
395

**Figure 2** (online color at: www.pss-b.com) Site energy fluctuations and corresponding DOS exemplified using three individual BChls from the B850 ring and of one BChl from the B800 ring. The coupling between the BChls is not taken into account in this figure.

In the Förster approach to exciton dynamics the coupling is assumed to be dominated by the Coulomb interaction and calculated using the PDA. Including a screening factor $f$ which will be detailed below, the PDA is given by

$$V_{nm} = \frac{f}{4\pi\varepsilon_0}\left(\frac{\mathbf{d}_m\mathbf{d}_n}{R_{mn}^3} - 3\frac{(\mathbf{d}_m\mathbf{R}_{mn})(\mathbf{d}_n\mathbf{R}_{mn})}{R_{mn}^5}\right), \qquad (1)$$

where the vector $\mathbf{d}_m$ denotes the optical transition dipole moments, which were rescaled by 0.558 to match the experimental measured value of 6.3 $D$ [45] on average. $\mathbf{R}_{mn}$ connects the center of the BChls $m$ and $n$ and $R_{mn}$ denotes the corresponding distance. The PDA has been applied in many studies, e.g., Refs. [27, 31–33], for reasons of simplicity although its problematic behavior for short distances is well known.

To get an improved description of the spatial arrangement of the charges, Renger and co-workers developed the TrEsp method [32, 35]. In this approach, the transition density of pigment $m$ is described using atomic transition charges $q_I^T$ that are localized at the respective pigment, i.e., $\rho(\mathbf{r}) = \sum_I q_I^T \delta(\mathbf{r} - \mathbf{R}_m^I)$ where $\mathbf{R}_m^I$ denotes the coordinates of the $I$th atom of BChl $m$. The coupling between two pigment molecules is then given by

$$V_{nm} = \frac{f}{4\pi\varepsilon_0}\sum_{I,J}\frac{q_I^T \cdot q_J^T}{|\mathbf{R}_m^I - \mathbf{R}_n^J|}. \qquad (2)$$

In Ref. [32] these charges were calculated on the level of HF-CIS and TDDFT/B3LYP. In the following, the corresponding couplings will be denoted as TrEsp(HF) and TrEsp(DFT), respectively.

In addition, to include solvent effects to the couplings, the results for the PDA and TrEsp need to be scaled. To this end, two approaches are commonly used: while in the Förster theory the screening factor is given by $f_F = 1/n^2$, in the Onsager theory cavities around the dipole are assumed and

the factors is determined to be $f_O = 3/(2n^2 + 1)$. In these expressions $n$ denotes the refractive index. After a detailed analysis on protein environments, Scholes et al. [36] fitted a distance-dependent screening factor to their results

$$f(R_{mn}) = A\exp(-BR_{mn}) + f_O, \qquad (3)$$

with $A = 2.68$, $B = 0.27$ 1/Å, and $f_O = 0.54$. At large distances ($R_{mn} > 20$ Å) this function reaches the value $f = 0.54$ which lies in between the values used in Förster theory $f_F$ and the Onsager value $f_O$ for $n^2 = 2$, i.e., a protein environment. In the following calculations, this distance-dependent solvent-screening factor $f$ is applied to all results, i.e., to the PDA, TrEsp(HF), as well as TrEsp(DFT) approaches.

The probability densities to find certain coupling values in the B850 ring along the MD trajectory are shown Fig. 3 for the three different methods detailed above. In comparison, the PDA method yields larger average coupling values of 0.035 cm⁻¹ (282 cm⁻¹) and the broadest distribution. Also the distribution does not show any splitting into intra- and inter-dimer couplings.

When using the TrEsp methods a splitting into couplings between the BChls within the heterodimer and couplings between the heterodimers can be observed. The charges used in the TrEsp method resulting from the TDDFT and the HF/CIS calculations are rather similar after rescaling them in order to obtain realistic transition dipole moments. The observed variations result from different treatments of electron interaction in the two electronic structure theories. The couplings within and between the dimers calculated using TrEsp(HF) are on average 0.024 eV (195 cm⁻¹) and 0.021 eV (166 cm⁻¹), respectively. The average values for TrEsp(DFT) are 0.021 eV (172 cm⁻¹) and for the intra-dimer couplings 0.017 eV (138 cm⁻¹). Furthermore, the couplings between the individual BChls within the B800 ring are much lower than those in the B850 ring due to their average
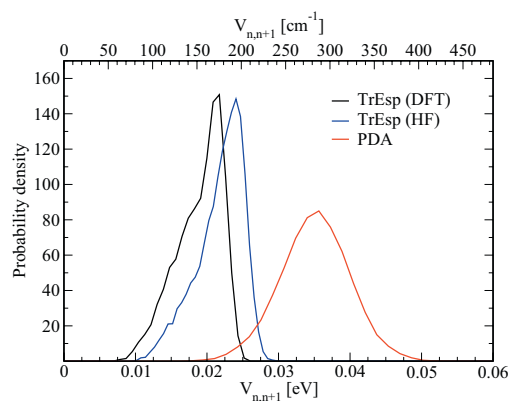


**Figure 3** (online color at: www.pss-b.com) Probability density of the electronic couplings in the B850 ring using three different approaches.

distance of about 22.25 Å. For the PDA, we get an average value of $-1.00 \times 10^{-3}$ eV ($-8.06$ cm$^{-1}$). The average coupling strength for TrEsp(HF) and TrEsp(DFT) are $-1.07 \times 10^{-3}$ eV ($-8.63$ cm$^{-1}$) and $-1.17 \times 10^{-3}$ eV ($-9.43$ cm$^{-1}$), respectively.

**5 Excitonic states and linear absorption** The excitonic states of the complete system can be determined from the site energies and the electronic couplings gained from the quantum chemical calculations. To achieve this, a Hamiltonian for the LH2 composed of the two BChl rings is constructed. This Hamiltonian includes the excitation energies of the sites and the couplings $V_{nm}(t)$ between them

$$H(t) = \sum_n |n\rangle \varepsilon_n(t) \langle n| + \sum_{n,m} |n\rangle V_{nm}(t) \langle m|. \quad (4)$$

Here the states $|n\rangle$ represent the singly excited BChl states and the energies $\varepsilon_n(t)$ correspond to the energy difference between the ground and excited state of BChl $n$. The indices $n$ and $m$ run over all 24 sites. In addition, the site energies of the eight BChls belonging to the B800 ring where shifted by an energy of 44 meV. This was necessary since the absolute value of the individual site energies is not reproduced exactly by the ZINDO approach. In order to calculate the energies of the excitonic states the system Hamiltonian needs to be diagonalized. Since the values of the site energies and the couplings vary along the MD trajectory this diagonalization has to be carried out at every time step resulting in time-dependent exciton energies. The upper panel of Fig. 4 shows the time evolution of these excitonic state energies. The energies lie within a range of 1.4–2 eV. It is evident that the energies of the higher exciton states oscillate notably stronger then those belonging to the low energy states. This becomes more obvious in the DOS of the individual states which is shown in the middle panel of Fig. 4. As can be seen there, the width of the distribution increases for increasing energies. The lower panel of Fig. 4 depicts the average excitonic energies over the 12 ps long MD trajectory with error bars corresponding to the variance of the DOS of the individual states.

The spectrum of linear absorbance is calculated to be able to compare the simulated results with experiments. To compute this experimentally accessible observable the excitonic transition dipole moments are needed in addition to the excitonic energies. They can be calculated from the expansion coefficients $C_\nu^n$ of the excitonic states in the site representation and the transition dipole moments $\mathbf{d}_n$ from the ZINDO/S calculations

$$\mathbf{d}_\nu = \sum_n C_\nu^n \mathbf{d}_n. \quad (5)$$

The dipole strength for an excitonic state $\nu$ can then be given as

$$D_\nu = |\mathbf{d}_\nu|^2 = \sum_n \sum_m C_\nu^n C_\nu^{*m} \times (\mathbf{d}_n \mathbf{d}_m). \quad (6)$$
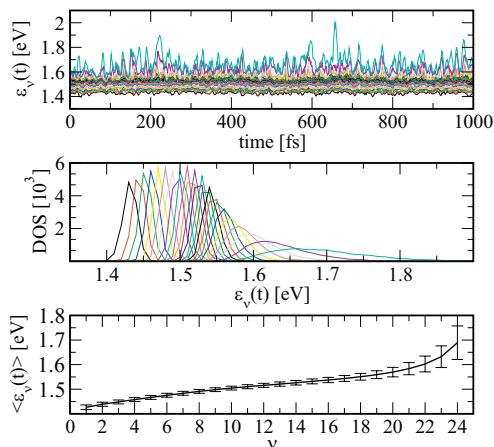


**Figure 4** (online color at: www.pss-b.com) Excitonic energies of the complete LH2 system as calculated using the TrEsp(DFT) couplings. The individual excitonic states are distinguished by different colors. Upper panel: Time evolution of the exciton energies, every line belongs to one excitonic state. Middle panel: Distribution of the exciton energies along the MD trajectory. Lower panel: Average exciton energies with error bars corresponding to the variance of the distribution.
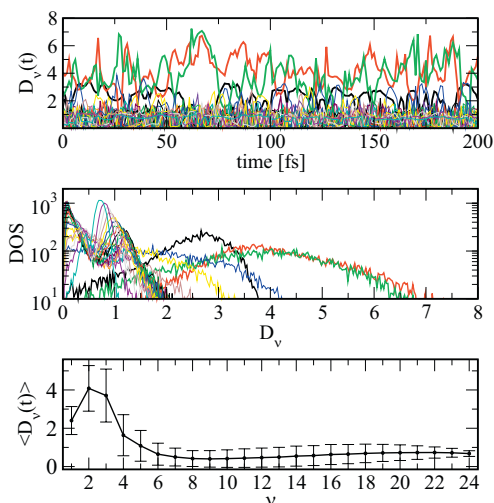


**Figure 5** (online color at: www.pss-b.com) Excitonic dipole strengths in units of the average monomeric dipole strength of 6.3 $D$ as calculated using TrEsp(DFT) couplings. The various states are distinguished by different colors. Upper panel: Time evolution of the dipole strengths, every line belongs to one excitonic state. Middle panel: Distribution of the dipole strengths along the MD trajectory. Lower panel: Average dipole strength with error bars corresponding to the variance of the distribution.

**Original**

**Paper**
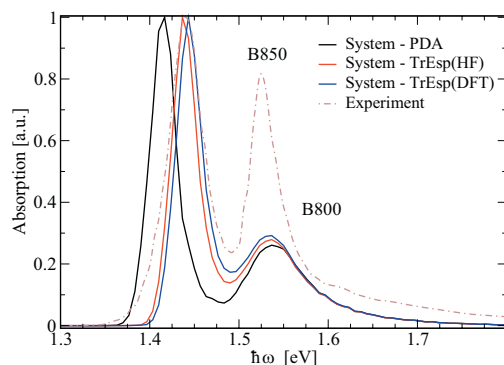


**Figure 6** (online color at: www.pss-b.com) Absorption spectrum evaluated from the DOS weighted with the dipole strengths for TrEsp and PDA calculations compared to the experimentally obtained spectrum [47].

Shown in Fig. 5 are the obtained values. The upper panel displays the time evolution of the dipole strength for each excitonic state. The distribution of the individual dipole strengths within the MD trajectory is shown in the middle panel and the average dipole strength with corresponding variance of the distribution in the lower one.

If a δ-like absorption line shape is assumed, the linear absorption spectrum is comparable to the sum over all DOSs of the individual excitonic levels weighted by their dipole strengths. To estimate the spectrum the frequency axis is divided into an equidistant grid with spacing $\Delta\omega$ (binning). The value of the spectrum at grid point $\omega_j$ is then evaluated by adding up all dipole strengths of those excitonic levels which lie in the energy range of $\omega_j \pm \frac{1}{2}\Delta\omega$ [24, 39, 46]. The absorption spectrum for the three different calculated couplings is shown in Fig. 6 together with an experimentally obtained spectrum [47]. All three employed methods produce spectra which show the same basic features as the experimental one. Using the PDA the absorption peak of the B850 ring lies at a notably lower frequency than the peaks in the spectra obtained from TrEsp couplings. Both TrEsp couplings produce spectra with a good agreement to the experiment.

**6 Conclusions** Based on the trajectory of the MD simulation the energy gap fluctuations between ground and excited state were calculated on the semiempirical ZINDO/S level. From the absorption spectrum it can be deferred that a good agreement of the site energies and the experimental data were obtained. Only the energies for the B800 ring had to be slightly shifted (44 meV) due to an insufficient red shift in the ZINDO calculations. An important quantity beside the site energies is the coupling. To this end the commonly used PDA was compared to the TrEsp method using two different sets of transition charges from either HF-CIS or TDDFT/ B3LYP calculations. In addition a distance-dependent

solvent screening factor was used. We were able to show that the TrEsp methods show an obvious splitting of couplings due to the eightfold symmetry of the system. The TrEsp approach yields rather accurate coupling values due to the more realistic representation of the transition densities of the whole molecules. Especially for short distances this is certainly superior to the PDA. The site energies together with the couplings were used in a time-depend Hamiltonian approach for the complete system of the B850 and B800 rings. Especially the obtained excitonic energies of the higher levels show strong fluctuations. Opposite to this, the dipole strengths of the lower excitonic levels have a broad distribution. The first four levels on average carry the largest dipole strengths leading to a peak of the B850 ring in the absorption spectra. The dipole strength for the excitonic level with energy around the B800 peak (1.55 eV) is rather low. This might be the reason for the smaller absorption strength of the B800 ring in the simulations compared to experiment. This discrepancy might also be caused by an insufficient sampling of the relevant energies and dipole strengths. The three different kinds of couplings, PDA and TrEsp(HF) and TrEsp(DFT), do not have a large influence on the peak position of the B800 ring due to the low coupling between the BChls in all three cases. The larger couplings of the PDA compared to TrEsp approaches for the BChls in the B850 ring lead to a red shift of the calculated B850 peak and a larger splitting between the two peaks of the complex. Due to the quite similar average coupling values of TrEsp(DFT) and TrEsp(HF) methods for the BChls within the B850 ring the spectra does but differ remarkable. The spectra are in good agreement with the experimental one.

In the present contribution the time-dependent Hamiltonian was analyzed in terms of the time dependence of the excitonic states and the resulting absorption. In Ref. [15] it is shown how the data can be used to obtain the so-called spectral density. This function is a key ingredient in the theory of open quantum systems and can also be used to determine exciton dynamics and optical properties [48–51].

### References

[1] X. Hu, T. Ritz, A. Damjanović, F. Autenrieth, and K. Schulten, Q. Rev. Biophys. **35**, 1–62 (2002).
[2] R. J. Cogdell, A. Gall, and J. Köhler, Q. Rev. Biophys. **39**, 227–324 (2006).
[3] V. Sundström, Annu. Rev. Phys. Chem. **59**, 53–77 (2008).
[4] Y. C. Cheng and G. R. Fleming, Annu. Rev. Phys. Chem. **60**, 241–242 (2009).
[5] V. I. Novoderezhkin and R. van Grondelle, Phys. Chem. Chem. Phys. **12**, 7352–7365 (2010).
[6] H. van Amerongen, L. Valkunas, and R. van Grondelle, Photosynthetic Excitons (World Scientific, Singapore, 2000).

137

[7] S. Georgakopoulou, R. N. Frese, E. Jonson, C. Koolhaas, R. J. Cogdell, R. van Grondelle, and G. van der Zwan, Biophys. J. **82**, 2184–2197 (2002).

[8] X. Hu, A. Damjanović, T. Ritz, and K. Schulten, Proc. Natl. Acad. Sci. USA **95**, 5935–5941 (1998).

[9] A. Damjanović, I. Kosztin, U. Kleinekathöfer, and K. Schulten, Phys. Rev. E **65**, 031919 (2002).

[10] S. Tretiak, C. Middleton, V. Chernyak, and S. Mukamel, J. Phys. Chem. B **104**, 4519–4528 (2000).

[11] S. Tretiak, C. Middleton, V. Chernyak, and S. Mukamel, J. Phys. Chem. B **104**, 9540–9553 (2000).

[12] A. Damjanović, H. M. Vaswani, P. Fromme, and G. R. Fleming, J. Phys. Chem. B **106**, 10251–10262 (2002).

[13] M. Yang, A. Damjanović, H. M. Vaswani, and G. R. Fleming, Biophys. J. **85**, 140–148 (2003).

[14] M. E. Madjet, F. Müh, and T. Renger, J. Phys. Chem. B **113**, 12603–12614 (2009).

[15] C. Olbrich and U. Kleinekathöfer, J. Phys. Chem. B **114**, 12427–12437 (2010).

[16] W. F. Humphrey, A. Dalke, and K. Schulten, J. Mol. Graph. **14**, 33–38 (1996).

[17] J. Koepke, X. Hu, C. Muenke, K. Schulten, and H. Michel, Structure **4**, 581–597 (1996).

[18] J. Ridley and M. C. Zerner, Theor. Chim. Acta **32**, 111–134 (1973).

[19] M. C. Zerner, G. H. Loew, R. F. Kirchner, and U. T. Mueller-Westerhoff, J. Am. Chem. Soc. **102**, 589–599 (1980).

[20] J. Li, B. Williams, C. J. Cramer, and D. G. Truhlar, J. Chem. Phys. **110**, 724–733 (1999).

[21] M. G. Cory, M. C. Zerner, X. Hu, and K. Schulten, J. Phys. Chem. B **102**, 7640–7650 (1998).

[22] J. Linnanto and J. Korppi-Tommola, Phys. Chem. Chem. Phys. **2**, 4962–4970 (2000).

[23] J. Linnanto and J. Korppi-Tommola, Phys. Chem. Chem. Phys. **2**, 3453–3460 (2002).

[24] L. Janosi, I. Kosztin, and A. Damjanović, J. Chem. Phys. **125**, 014903 (2006).

[25] J. Linnanto and J. Korppi-Tommola, Phys. Chem. Chem. Phys. **8**, 663–667 (2006).

[26] J. Linnanto and J. Korppi-Tommola, Chem. Phys. **357**, 171–180 (2009).

[27] I. A. Howard, F. Zutterman, G. Deroover, D. Lamoen, and C. V. Alsenoy, J. Phys. Chem. B **108**, 19155–19162 (2004).

[28] M. C. Zwier, J. M. Shorb, and B. P. Krueger, J. Comput. Chem. **28**, 1572–1581 (2007).

[29] J. S. Kwon, C. M. Choi, H. J. Kim, N. J. Kim, J. Jang, and M. Yang, J. Phys. Chem. A **113**, 2715–2723 (2009).

[30] J. Neugebauer, Chemphyschem **10**, 3148–3153 (2009).

[31] J. Linnanto, J. E. I. Korppi-Tommola, and V. Helenius, J. Phys. Chem. B **103**, 8739–8750 (1999).

[32] M. E. Madjet, A. Abdurahman, and T. Renger, J. Phys. Chem. B **110**, 17268–17281 (2006).

[33] D. Beljonne, C. Curutchet, G. D. Scholes, and R. J. Silbey, J. Phys. Chem. B **113**, 6583–6599 (2009).

[34] B. Krueger, G. Scholes, and G. Fleming, J. Phys. Chem. B **102**, 5378–5386 (1998).

[35] T. Renger, Photosynth. Res. **102**, 471–485 (2009).

[36] G. D. Scholes, C. Curutchet, B. Mennucci, R. Cammi, and J. Tomasi, J. Phys. Chem. B **111**, 6978–6982 (2007).

[37] T. L. C. Jansen and J. Knoester, J. Phys. Chem. B **110**, 22910–22916 (2006).

[38] T. L. C. Jansen and J. Knoester, Acc. Chem. Res. **42**, 1405–1411 (2009).

[39] H. Zhu, V. May, B. Röder, and T. Renger, J. Chem. Phys. **128**, 154905 (2008).

[40] H. Zhu, B. Röder, and V. May, Chem. Phys. **362**, 19–26 (2009).

[41] J. C. Phillips, R. Braun, W. Wang, J. Gumbart, E. Tajkhorshid, E. Villa, C. Chipot, R. D. Skeel, L. Kale, and K. Schulten, J. Comput. Chem. **26**, 1781–1802 (2005).

[42] T. Petrenko and F. Neese, J. Chem. Phys. **127**, 164319 (2007).

[43] I. P. Mercer, I. R. Gould, and D. R. Klug, J. Phys. Chem. B **103**, 7720–7727 (1999).

[44] M. R. Silva-Junior and W. Thiel, J. Chem. Theor. Comput. **6**, 1546–1564 (2010).

[45] R. G. Alden, E. Johnson, V. Nagarajan, W. W. P. J. Law, and R. G. Cogdell, J. Phys. Chem. B **101**, 4667–4680 (1997).

[46] H. Zhu, V. May, B. Röder, M. E. Madjet, and T. Renger, Chem. Phys. Lett. **444**, 118–124 (2007).

[47] J. P. Zhang, R. Fujii, P. Qian, T. Inaba, T. Mizoguchi, and Y. Koyama, J. Phys. Chem. B **104**, 3683–3691 (2000).

[48] P. Heřman, U. Kleinekathöfer, I. Barvík, and M. Schreiber, J. Lumin. **94/95**, 447–450 (2001).

[49] P. Heřman, U. Kleinekathöfer, I. Barvík, and M. Schreiber, Chem. Phys. **275**, 1–13 (2002).

[50] U. Kleinekathöfer, I. Barvík, P. Heřman, I. Kondov, and M. Schreiber, J. Phys. Chem. B **107**, 14094–14102 (2003).

[51] J. Strümpfer and K. Schulten, J. Chem. Phys. **131**, 225101 (2009).

# List of Figures

# Bibliography

[1] E. L. Wolf: *Nanophysics and Nanotechnology* (Wiley–VCH, Berlin, 2006)

[2] A. H. Zewail: *Femtochemistry: Ultrafast dynamics of the chemical bond, vol. I + II* (World Scientific, 1994)

[3] P. Ball: Nature **474** (2011) 272

[4] G. D. Scholes: Nat Phys **7** (2011) 448

[5] Science **332** (2011) 1488

[6] X.-J. Yang, X.-K. Liao, K. Lu, Q.-F. Hu, J.-Q. Song and J.-S. Su: J. Comput. Sci. & Technol. **26** (2011) 344

[7] D. Marx and J. Hutter: *Ab Initio Molecular Dynamics: Basic Theory and Advanced Methods* (Cambridge University Press, Cambridge, 2010)

[8] D. J. Tannor: *Introduction to Quantum Mechanics: A Time-Dependent Perspective* (University Science Books, Sausalito, 2007)

[9] A. H. Zewail: J. Phys. Chem. A **104** (2000) 5660

[10] J. Manz and L. Wöste: *Femtosecond chemistry* (VCH, Weinheim, 1995)

[11] V. Sundström, T. Pullertis and R. van Grondelle: J. Phys. Chem. B **103** (1999) 2327

[12] T. Brixner, J. Stenger, H. M. Vaswani, M. Cho, R. E. Blankenship and G. R. Fleming: Nature **434** (2005) 625

[13] A. H. Zewail: Science **242** (1988) 1645

[14] J. S. Briggs and J. M. Rost: Eur. Phys. J. D **10** (2000) 311

[15] J. S. Briggs and J. M. Rost: Found. Phys. **31** (2001) 693

[16] S. Mukamel: *Principles of Nonlinear Optical Spectroscopy* (Oxford University Press, 1995)

[17] Y. R. Shen: *The Principle of Nonlinear Optics* (Wiley, New York, 1984)

[18] R. W. Boyd: *Nonlinear Optics* (Academic Press, San Diego, 2003)

[19] M. Motzkus, S. Pedersen and A. Zewail: J. Phys. Chem. **100** (1996) 5620

[20] J. Faeder, I. Pinkas, G. Knopp, Y. Prior and D. Tannor: J. Chem. Phys. **115** (2001) 8440

[21] B. Zhang, N. Gador and T. Hansson: Phys. Rev. Lett. **91** (2003) 173006

[22] S. Meyer and V. Engel: Appl. Phys. B **71** (2000) 293

[23] A. Scaria, V. Namboodiri, J. Konradi and A. Materny: J. Chem. Phys. **127** (2007)

[24] A. Scaria, V. Namboodiri, J. Konradi and A. Materny: Phys. Chem. Chem. Phys. **10** (2008) 983

[25] A. Scaria: *Investigation of complex molecular dynamics in the gas phase using femtosecond four-wave mixing spectoscopy*. Ph.D. thesis, Jacob University Bremen (2008)

[26] M. Schmitt, G. Knopp, A. Materny and W. Kiefer: Chem. Phys. Lett. **270** (1997) 9

[27] M. Schmitt, G. Knopp, A. Materny and W. Kiefer: Chem. Phys. Lett. **280** (1997) 339

[28] M. Schmitt, G. Knopp, A. Materny and W. Kiefer: J. Phys. Chem. A **102** (1998) 4059

[29] M. Vrakking, D. Villeneuve and A. Stolow: Phys. Rev. A **54** (1996) R37

[30] I. Averbukh, M. Vrakking, D. Villeneuve and A. Stolow: Phys. Rev. Lett. **77** (1996) 3518

[31] S. Meyer, M. Schmitt, A. Materny, W. Kiefer and V. Engel: Chem. Phys. Lett. **287** (1997) 753

[32] S. Meyer, M. Schmitt, A. Materny, W. Kiefer and V.Engel: Chem. Phys. Lett. **301** (1999) 248

[33] S. Meyer and V. Engel: Appl. Phys. B **71** (2000) 293

[34] J. A. Coxon: J. Mol. Spectrosc. **37** (1971) 39

[35] R. F. Barrow, T. C. Clark, J. A. Coxon and K. K. Yee: J. Mol. Spectrosc. **51** (1974) 428

[36] R. Mulliken: J. Chem. Phys. **55** (1971) 288

[37] J. C. D. Brand, A. R. Hoy, A. Kalkar and A. Yamashita: J. Mol. Spectrosc. **95** (1982) 350

[38] K. S. Viswanathan and J. Tellinghuisen: J. Mol. Spectrosc. **101** (1983) 285

[39] J. P. Perrot, M. Broyer, J. Chevaleyre and B. Femelat: J. Mol. Spectrosc. **98** (1983) 161

[40] T. Ishiwata, H. Takekawa and K. Obi: J. Mol. Spectrosc. **159** (1993) 443

[41] Y. Nakano, H. Ukeguchi and T. Ishiwata: J. Chem. Phys. **121** (2004) 1397

[42] D. R. Glenn, D. A. Lidar and V. A. Apkarian: Mol. Phys. **104** (2006) 1249

[43] M. Shapiro and P. Brumer: Phys. Rep. **425** (2006) 195

[44] D. Ambrosek, M. Oppel, L. González and V. May: Chem. Phys. Lett. **380** (2003) 536

[45] F. H. M. Faisal: *Theory of Multiphoton Processes* (Plenum Press, New York, 1987)

[46] D. Meshulach and Y. Silberberg: Nature **396** (1998) 239

[47] D. Meshulach and Y. Silberberg: Phys. Rev. A **60** (1999) 1287

[48] V. May and O. Kühn: *Charge and Energy Transfer in Molecular Systems* (Wiley–VCH, Berlin, 2004), 2 edition

[49] U. Kleinekathöfer: J. Chem. Phys. **121** (2004) 2505

[50] T. L. C. Jansen and J. Knoester: J. Phys. Chem. B **110** (2006) 22910

[51] T. L. C. Jansen and J. Knoester: Acc. Chem. Res. **42** (2009) 1405

[52] H. Zhu, V. May, B. Röder and T. Renger: J. Chem. Phys. **128** (2008) 154905

[53] H. Zhu, B. Röder and V. May: Chem. Phys. **362** (2009) 19

[54] H. Michel: J. Mol. Biol. **158** (1982) 567

[55] A. R. Leach: *Molecular modelling, principles and applications* (Pearson, Harlow, 2001), 2nd edition

[56] F. Jensen: *Introduction to computational chemistry* (Wiley, Chichester, 2007), 2nd edition

[57] H. Grubmüller and K. Schulten: J. Struct. Biol. **157** (2007) 443

[58] A. Koyré and I. B. Cohen (eds.): *Isaac Newton's Philosophiae Naturalis Principia Mathematica: the Third edition (1726) with variant readings* (Harvard UP, Cambridge, 1972)

[59] C. Olbrich, J. Liebers and U. Kleinekathoefer: Phys. Status Solidi B **248** (2011) 393

[60] C. Olbrich, J. Struempfer, K. Schulten and U. Kleinekathoefer: J. Phys. Chem. Lett. **2** (2011) 1771

[61] H. P. Breuer and F. Petruccione: *The Theory of Open Quantum Systems* (Oxford University Press, Oxford, 2002)

[62] J. Liebers, A. Scaria, A. Materny and U. Kleinekathöfer: J. Raman Spectros. **40** (2009) 822

[63] A. Scaria, J. Liebers, U. Kleinekathoefer and A. Materny: Chem Phys Lett **470** (2009) 39

[64] J. Liebers, A. Scaria, A. Materny and U. Kleinekathofer: Phys. Chem. Chem. Phys. **12** (2010) 1351

[65] J. Lieber, U. Kleinekathöfer and V. May: Chem. Phys. **347** (2008) 229

[66] A. Bastida, C. Cruz, J. Zuniga, A. Requena and B. Miguel: Chem. Phys. Lett. **417** (2006) 53

[67] A. Bastida, C. Cruz, J. Zuniga, A. Requena and B. Miguel: J. Chem. Phys. **126** (2007) 014503

[68] A. Bastida, J. Zuniga, A. Requena and B. Miguel: J. Chem. Phys. **129** (2008) 154501

[69] C. Olbrich and U. Kleinekathoefer: J. Phys. Chem. B **114** (2010) 12427

[70] C. Olbrich, T. L. C. Jansen, J. Liebers, M. Aghtar, J. Struempfer, K. Schulten, J. Knoester and U. Kleinekathoefer: J. Phys. Chem. B **115** (2011) 8609

[71] W. Kaiser: *Ultrashort laserpulses and applications* (Springer-Verlag, Berlin Heidelberg New York, 1988)

[72] V. V. Lozovoy, I. Pastirk, E. J. Brown, B. I. Grimberg and M. Dantus: Int. Rev. Phys. Chem. **19** (2000) 531

[73] T. H. Joo and A. C. Albrecht: Chemical Physics **173** (1993) 17

[74] T. Joo and A. C. Albrecht: Chemical Physics **176** (1993) 233

[75] A. C. Eckbreth: Appl. Phys. Lett. **32** (1978) 421

[76] P. P. Ho and R. R. Alfano: Phys. Rev. A **20** (1979) 2170

[77] R. Rydberg: Z. Physik **73** (1931)

[78] R. Rydberg: Z. Physik **80** (1933)

[79] O. Klein: Z. Physik **76** (1932)

[80] A. L. G. Rees: Proc. Phys. Soc. (London) **59** (1947) 998

[81] R. J. Le Roy: *RKR1 2.0: A Computer Program Implementing the First-Order RKR Method for Determining Diatomic Molecule Potential Energy Curves*. Research Report CP-657R, University of Waterloo (2004)

[82] R. J. Le Roy: *LEVEL 8.0 A Computer Program for Solving the Radial Schrödinger Equation for Bound and Quasibound Levels*. Research Report CP-663, University of Waterloo (2007)

[83] R. Kosloff: In R. E. Wyatt and J. Z. H. Zhang (eds.), *Dynamics of Molecules and Chemical Reactions* (Marcel Dekker, New York, 1996)

[84] J. C. Tremblay and T. Carrington: J. Chem. Phys. **121** (2004) 11535

[85] C. Leforestier, R. H. Bisseling, C. Cerjan, M. D. Feit, R. Friesner, A. Guldberg, A. Hammerich, G. Jolicard, W. Karrlein, H.-D. Meyer, N. Lipkin, O. Roncero and R. Kosloff: J. Comp. Phys. **94** (1991) 59

[86] R. de Vivie-Riedle and A. Hofmann: In W. Domcke, D. R. Yarkony and H. Köppel (eds.), *Conical intersections: Electronic Structure, Dynamics and spectroscopy* (World Scientific, Singapore, 2004)

[87] L. X. Wang, H. D. Meyer and V. May: J. Chem. Phys. **125** (2006)

[88] H. D. Meyer, U. Manthe and L. S. Cederbaum: Chem. Phys. Lett. **165** (1990) 73

[89] U. Manthe, H. D. Meyer and L. S. Cederbaum: J. Chem. Phys. **97** (1992) 3199

[90] L. Seidner, G. Stock and W. Domcke: J. Chem. Phys. **103** (1995) 3998

[91] H. Wang and M. Thoss: Chem. Phys. Lett. **389** (2004) 43

[92] M. F. Gelin, D. Egorova and W. Domcke: Chem. Phys. **312** (2005) 135

[93] M. Gelin, D. Egorova and W. Domcke: J. Chem. Phys. **123** (2005)

[94] M. F. Gelin, A. V. Pisliakov, D. Egorova and W. Domcke: J. Chem. Phys. **118** (2003) 5287

[95] M. Motzkus, S. Pedersen and A. H. Zewail: J. Phys. Chem. **100** (1996) 5620

[96] J. Hauer, T. Buckup and M. Motzkus: J Phys Chem A **111** (2007) 10517

[97] R. Maksimenka, B. Dietzek, A. Szeghalmi, T. Siebert, W. Kiefer and M. Schmitt: Chemical Physics Letters **408** (2005) 37

[98] R. Zadoyan, D. Kohen, D. Lidar and V. Apkarian: Chem. Phys. **266** (2001) 323

[99] S. Pezeshki, M. Schreiber and U. Kleinekathöfer: Phys. Chem. Chem. Phys. **10** (2008) 2058

[100] K. P. Lawley and R. J. Donovan: J. Chem. Soc. Faraday Trans. **89** (1993) 1885

[101] R. M. Bowman, M. Dantus and A. H. Zewail: Chem. Phys. Lett. **174** (1990) 546

[102] P. Farmanara, H.-H. Ritze, V. Stert and W. Radloff: Chem. Phys. Lett. **307** (1999) 1

[103] H. Knockel, B. Bodermann and E. Tiemann: Eur. Phys. J. D **28** (2004) 199

[104] V. Engel: Comp. Phys. Commun. **63** (1991) 228

[105] G. W. King, I. M. Littlewood and J. R. Robbins: Chem. Phys. **56** (1981) 145

[106] J. P. Perrot, B. Femelat, M. Broyer and J. Chevaleyre: Mol. Phys. **61** (1987) 97

[107] J. P. Perrot, B. Femelat, J. L. Subtil, M. Broyer and J. Chevaleyre: mp **61** (1987) 85

[108] J. Konradi, A. K. Singh and A. Materny: Phys. Chem. Chem. Phys. **7** (2005) 3574

[109] J. Konradi, A. K. Singh and A. Materny: J. Photochem. Photobiol. A **180** (2006) 289

[110] R. M. Bowman, M. Dantus and A. H. Zewail: Chem. Phys. Lett. **161** (1989) 297

[111] G. Kerenskaya, I. U. Goldschleger, V. A. Apkarian and K. C. Janda: J. Phys. Chem. A **110** (2006) 13792

[112] M. Gühr, M. Bargheer, M. Fushitani, T. Kiljunen and N. Schwentner: Phys. Chem. Chem. Phys. **9** (2007) 779

[113] V. A. Ermoshin, A. K. Kazansky and V. Engel: J. Chem. Phys. **111** (1999) 7807

[114] S. Gerstenkorn, P. Luc, A. Raynal and J. Sinzelle: J. Phys. (France) **48** (1987) 1685

[115] J. C. D. Brand, U. D. Deshpande, A. R. Hoy and S. M. Jaywant: J. Mol. Spectrosc. **100** (1983) 143

[116] T. Ishiwata, A. Tokunaga, T. Shinzawa and I. Tanaka: Bull. Chem. Soc. Jpn. **57** (1984) 1317

[117] E. Hwang, P. J. Dagdigian and J. Tellinghuisen: J. Mol. Spectrosc. **181** (1997) 297

[118] J. Konradi, A. Gaal, A. Scaria, V. Namboodiri and A. Materny: J. Phys. Chem. **112** (2008) 1380

[119] C. Focsa, H. Li and P. Bernath: J. Mol. Spectrosc. **200** (2000) 104

[120] S. Gerstenkorn and P. Luc: J. Phys. France **50** (1989) 1417

[121] L. Frediani, Z. Rinkevicius and H. Ågren: J. Chem. Phys. **122** (2005) 244104

[122] S.-I. Chu: J. Chem. Phys. **123** (2005) 062207

[123] M. J. Paterson, O. Christiansen, F. Pawlowski, P. Jorgensen, C. Hütting, T. Helgaker and P. Salek: J. Chem. Phys. **124** (2006) 054322

[124] P. N. Day, K. A. Nguyen and R. Pachter: J. Chem. Phys. **125** (2006) 094103

[125] K. A. Walowicz, I. Pastirk, V. V. Lozovoz and M. Dantus: J. Phys. Chem. A **106** (2002) 9369

[126] V. V. Lozovoy, I. Pastirk, K. A. Walowicz and M. Dantus: J. Chem. Phys. **118** (2003) 3187

[127] D. Ambrosek, M. Oppel, L. González and V. May: Opt. Comm. **264** (2006) 502

[128] V. May, D. Ambrosek, M. Oppel and L. González: J. Chem. Phys. **127** (2007) 144102

[129] T. Kreibich, M. Lein, V. Engel and E. K. U. Gross: Phys. Rev. Lett. **87** (2001) 103901

[130] M. Lein, N. Hay, R. Velotta, J. P. Marangos and P. L. Knight: Phys. Rev. Lett. **88** (2002) 183903

[131] M. Erdmann, P. Marquetand and V. Engel: J. Chem. Phys. **119** (2003) 672

[132] M. Erdmann and V. Engel: J. Chem. Phys. **120** (2004) 158

[133] R. Xu, J. Cheng and Y. J. Yan: J. Chem. Phys. **103** (1999) 10611

[134] S. A. Hosseini and D. Goswami: Phys. Rev. A **64** (2001) 033410

[135] S. Nakajima: Prog. Theor. Phys. **20** (1958) 948

[136] R. Zwanzig: In W. E. Brittin, B. W. Downs and J. Downs (eds.), *Lectures in Theoretical Physics*, volume 3 (Interscience, New York, 1961), 106

[137] S. Mukamel, I. Oppenheim and J. Ross: Phys. Rev. A **17** (1978) 1988

[138] H. P. Breuer, B. Kappler and F. Petruccione: Phys. Rev. A **59** (1999) 1633

[139] V. Čápek: Physica A **203** (1994) 495

[140] A. Fuliński: Phys. Lett. A **25** (1967) 13

[141] A. Fuliński and W. J. Kramarczyk: Physica **39** (1968) 575

[142] N. Hashitsume, F. Shibata and M. Shingu: J. Stat. Phys. **17** (1977) 155

[143] F. Shibata, Y. Takahashi and N. Hashitsume: J. Stat. Phys. **17** (1977) 171

[144] V. Čápek: Physica A **203** (1994) 520

[145] S. Chaturvedi and F. Shibata: Z. Phys. B **35** (1979) 297

[146] A. Kaiser and V. May: Chem. Phys. **320** (2006) 95

[147] N. Nelson and A. Ben-Shem: Nat. Rev. Mol. Cell Biol. **5** (2004) 971

[148] R. Car and M. Parrinello: Phys. Rev. Lett. **55** (1985) 2471

[149] X. S. Li, J. C. Tully, H. B. Schlegel and M. J. Frisch: Journal of Chemical Physics **123** (2005) 084106

[150] B. Space and D. F. Coker: J. Chem. Phys. **94** (1991) 1976

[151] P. V. Parandekar and J. C. Tully: J. Chem. Phys. **122** (2005) 094102

[152] K. Drukker: J. Comp. Phys. **153** (1999) 225

[153] A. Damjanović, I. Kosztin, U. Kleinekathöfer and K. Schulten: Phys. Rev. E **65** (2002) 031919

[154] S. Shim, P. Rebentrost, S. Valleau and A. Aspuru-Guzik: *Microscopic Origin of the Long-Lived Quantum Coherences in the Fenna-Matthew-Olson Complex* (2011). ArXiv:1104.2943v1

[155] J. Ridley and M. C. Zerner: Theor. Chim. Acta **32** (1973) 111

[156] M. C. Zerner, G. H. Loew, R. F. Kirchner and U. T. Mueller-Westerhoff: J. Am. Chem. Soc. **102** (1980) 589

[157] C. Olbrich, J. Struempfer, K. Schulten and U. Kleinekathoefer: J. Phys. Chem. B **115** (2011) 758

[158] J. Koepke, X. Hu, C. Muenke, K. Schulten and H. Michel: Structure **4** (1996) 581

[159] J. Li, B. Williams, C. J. Cramer and D. G. Truhlar: J. Chem. Phys. **110** (1999) 724

[160] M. E. Madjet, A. Abdurahman and T. Renger: J. Phys. Chem. B **110** (2006) 17268

[161] T. Renger: Photosynth. Res. **102** (2009) 471

# Copyright Statement

- **Chapter 3**
  Reprinted from Publication: J. Liebers, A. Scaria, A. Materny and U. Kleinekathöfer: J. Raman Spectros. **40** (2009) 822, with permission from John Wiley and Sons.

- **Chapter 4**
  Reprinted from Publication: A. Scaria, J. Liebers, U. Kleinekathöfer and A. Materny: Chem. Phys. Lett. **470** (2009) 39, with permission from Elsevier.

- **Chapter 5**
  Reproduced by permission of the PCCP Owner Societies: J. Liebers, A. Scaria, A. Materny and U. Kleinekathöfer: Phys. Chem. Chem. Phys. **12** (2010) 1351

- **Chapter 6**
  Reprinted from Publication: J. Liebers, U. Kleinekathöfer and V. May: J. Chem. Phys. **347** (2008) 229, with permission from Elsevier.

- **Appendix B**
  Reprinted from Publication: C. Olbrich, J. Liebers and U. Kleinekathöfer: Phys. Status Solidi B **248** (2011) 393, with permission from John Wiley and Sons.

# List of publications

- J. Liebers, U. Kleinekathöfer and V. May: *Sequences of Ultrafast Non-Resonant Multiphoton Transitions in a Three-Electronic Level Molecule.*
  J. Chem. Phys. **347** (2008) 229

- A. Materny, U. Kleinekathöfer, A. Scaria, V. Namboodiri and J. Liebers: *Femtosecond four-wave mixing for investigation and control of molecular gas phase dynamics in different electronic states.* in Proc. 21st Int. Conf. on Raman Spectr., edited by R. Withnall and B. Z. Chowdhry (IM Publications LLP, Chichester, 2008).

- A. Scaria, J. Liebers, U. Kleinekathöfer and A. Materny: *Probing the contributions of hot vibrational states using pump-degenerate four-wave mixing.*
  Chem. Phys. Lett. **470** (2009) 39

- J. Liebers, A. Scaria, A. Materny and U. Kleinekathöfer: *Ultrafast vibrational dynamics in higher electronic excited states of iodine.*
  J. Raman Spectros. **40** (2009) 822

- J. Liebers, A. Scaria, A. Materny and U. Kleinekathöfer: *Probing the vibrational dynamics of high-lying electronic states using pump-degenerate four-wave mixing*
  Phys. Chem. Chem. Phys. **12** (2010) 1351

- C. Olbrich, J. Liebers and U. Kleinekathöfer: *Modeling of light-harvesting in purple bacteria using a time-dependent Hamiltonian approach*
  Phys. Status Solidi B **248** (2011) 393

- C. Olbrich, T.L.C. Jansen, J. Liebers, M. Aghtar, J. Strümpfer, K. Schulten, J. Knoester and U. Kleinekathöfer: *From Atomistic Modeling to Excitation Transfer and Two-Dimensional Spectra of the FMO Light-Harvesting Complex*
  J. Phys. Chem. B **115** (2011) 8609

# Acknowledgment

# Independence Statement

I hereby declare that I have written the thesis at hand on my own without submitting it for any other degree. It is the result of my own work except where stated differently. All quotes, references, and other sources have been acknowledged as such. The published manuscripts in this thesis are reproduced with permission of the corresponding publishers and described as such.

Jörg Liebers, Bremen, September 16, 2012